

POLITECNICO DI TORINO

Collegio di Ingegneria Meccanica e Aerospaziale

**Corso di Laurea Magistrale
In Ingegneria Aerospaziale**

Tesi di Laurea Magistrale

**CFD Simulation of Propellers:
Best Practices Analysis**



Relatore:

prof. Domenic D'Ambrosio

Candidato:

Manuel Carreño Ruiz

Marzo 2019

Abstract

This work presents the different methods available in the commercial CFD software STAR CCM+ for the simulation of small-scale propellers typically used in UAV's with special emphasis on the validity of a steady state approach based on the use of multiple frames of reference which is computationally cheap. The objective of this work is to assess the validity of the different approaches to capture low Reynolds number effects which most analytical approaches fail to represent appropriately.

Chapter 1 presents the motivation for the development of this thesis and a literature review on propeller performance. Chapter 2 provides the most important results from the main traditional theories; Momentum theories, Vortex theories and Blade Element Method. Chapter 3 compares the documented performance experimentally and theoretically, showing increasing discrepancies for lower Reynolds numbers. A part from the Reynolds number effects, other parameters that affect the performance are considered such as the pitch influence or stall characteristics of aerofoils. Chapter 4 gives a general view of the different methods embedded in the commercial software STAR CCM+ to solve rotating flows. Chapter 5 provides the description of the procedure followed to develop the CAD model and presents the experimental results for the propeller DA4022. Chapter 6 describes the CFD model setup and performs different analysis with the objective of validating and comparing the different approaches, concluding with the selection of the most adequate one. Chapter 7 shows the performance studies carried out for the propeller DA4022. Simulations were carried out for a variety of rotation and advance rates which allows a correct comparison between experimental and CFD calculated performance. Chapter 8 presents the development of a new more complex propeller, the commercially available APC 10x7 Inches Slow Flyer. Performance studies are also carried out on this propeller and the results are compared with available experimental data.

To family and friends

Acknowledgments

I would like to thank all professors which influenced positively my aeronautical education at Seville's University, Technical School of Madrid (UPM) and Politecnico di Torino. Especially I would like to thank Professor Domenic D'Ambrosio for giving me the opportunity of doing this CFD based thesis and the inestimable guidance during these months and also Professor Miguel Perez-Saborid for triggering my passion for Fluid Dynamics with his practical lessons and during the elaboration of my undergraduate thesis.

I would also like to thank family and friends which gave me the extra thrust that I needed to cruise through a 7-years Aeronautical education successfully. Especially I would like to thank my mother who has been always there for me even though I was in different cities or different countries, she always made me feel at home. And finally I would like to thank my colleague Carmen Velarde, for the unconditional support, friendship and for making these years incredibly happy for me.

Table of Contents

LIST OF FIGURES	VI
LIST OF TABLES	IX
1 INTRODUCTION	1
1.1 Motivation.....	1
1.2 Literature review	2
2 PROPELLERS	4
2.1 Momentum theories.....	4
2.1.1 Actuator Disc Theory.....	4
2.1.2 Extended Momentum Theory.....	7
2.2 Blade Element Theory	9
2.3 Vortex Theory.....	11
2.3.1 Constant circulation distribution, $\Gamma(r) = constant$	12
2.3.2 Radial circulation distribution, $\Gamma(r)$	15
3 PROPELLER PERFORMANCE	17
3.1 Expected theoretical performance.....	19
3.1.1 Momentum Theory Performance.....	19
3.1.1.1 Actuator disc theory.....	19
3.1.1.2 General momentum theory.....	20
3.1.2 Blade Element Momentum Theory(BEMT).....	21
3.2 Reynolds Number effects.....	23
3.3 Pitch angle variation	27
3.4 Stall aerofoil characteristics	28
4 CFD SIMULATION OF ROTATING FLOWS	30
4.1 Solvers selection.....	30
4.1.1 Steady state approaches	30
4.1.2 Unsteady approaches	32
4.2 Mesh selection.....	33
4.2.1 Structured and unstructured meshing.....	33
4.2.2 Prism layer mesher	33
4.3 Turbulence modelling.....	37
4.3.1 Reynolds Averaged Navier-Stokes Equations(RANS)	37
4.3.2 Unsteady Reynolds Averaged Navier-Stokes Equations(URANS)	38
4.3.3 Large Eddy Simulation(LES) and Detached Eddy Simulations(DES).....	38

5	BENCHMARK TEST: DA-4022 5X3.75 INCHES.....	40
5.1	CAD Modelling.....	40
5.2	Experimental performance.....	43
6	CFD SIMULATIONS: VALIDATION STUDIES.....	46
6.1	Problem definition.....	46
6.1.1	Fluid domain.....	46
6.1.2	Mesh generation.....	47
6.1.2.1	Surface meshing.....	47
6.1.2.2	Volume mesh.....	48
6.1.2.3	Prism layer mesher.....	48
6.1.3	Interfaces and Boundary conditions.....	49
6.1.4	Physics models.....	50
6.2	Mesh refinement study.....	52
6.3	Rotating region sensitivity analysis.....	58
6.4	Turbulence models.....	64
6.5	Interface and boundary conditions effects.....	66
6.6	Unsteady Simulation: Rigid Body Motion.....	67
7	PERFORMANCE RESULTS: DA4022.....	73
8	APC SLOW FLYER:10X7.....	79
9	CONCLUSIONS AND FUTURE WORK.....	86
10	BIBLIOGRAPHY.....	88
	APPENDIX A: SDA 1075 AEROFOIL COORDINATES.....	90
	APPENDIX B: GEOMETRY DATA DA4022.....	91
	APPENDIX C: MATLAB ROUTINES FOR CAD GENERATION.....	92
	APPENDIX D: PROPELLERSCANNER RAW DATA: APC SLOW FLYER 10X7 INCHES.....	93
	APPENDIX E: GEOMETRY MATRIX APC SLOW FLYER 10X7 INCHES.....	94
	APPENDIX F: MATLAB ROUTINES FOR APC CAD GENERATION.....	95
	APPENDIX G: APC 10X7 SLOW FLYER AEROFOIL COORDINATES.....	96

List of Figures

Figure 1.1: Jet Propulsion Laboratory Helicopter.	2
Figure 2.1: Actuator disc model and variation of relevant magnitudes.	5
Figure 2.2: Extended momentum theory.	7
Figure 2.3: Annular differential control volume for the Extended Momentum Theory.	8
Figure 2.4: Element dr at radial position r	10
Figure 2.5: N.E Joukowski original diagram of constant circulation vortex system.	12
Figure 2.6: Vortex system of the actuator disc ($N \rightarrow \infty$) with constant circulation.	13
Figure 3.1: Element dr at position r	21
Figure 3.2: Blade element momentum method iteration loop.	23
Figure 3.3: Laminar recirculation bubble region from McGranaham[14].	23
Figure 3.4: Reynolds Number variation for DA4002 9x6.75 propeller at 5000RPM from[5].	24
Figure 3.5: Power coefficient DA4002 9-inches.	24
Figure 3.6: Thrust coefficient DA4002 9-inches.	25
Figure 3.7: Efficiency DA4002 9-inches.	25
Figure 3.8: Drag Coefficient distribution along the span for DA4002 9x6.75. Deters[5].	26
Figure 3.9: Lift Coefficient distribution along the span for DA4002 9x6.75. Deters[5].	27
Figure 3.10: Pitch influence on efficiency for DA4002 5xp.	28
Figure 4.1: Turbomachinery simulation using mixing plane approach[15].	31
Figure 4.2: Coordinate system in static and rotating frames of reference[7].	31
Figure 4.3: Boundary layer thickness estimation for a full scale propeller with a turbulent boundary layer.	35
Figure 4.4: Boundary layer thickness estimation for a small scale propeller with a turbulent boundary layer.	36
Figure 5.1: SDA1075 aerofoil.	40
Figure 5.2: Chord distribution of the manufactured and designed models.	41
Figure 5.3: Pitch angle distribution of the manufactured and designed models.	42
Figure 5.4: Top, front and side views of the CAD modelled geometry.	42
Figure 5.5: Rendered Image of CAD modelled Geometry.	42
Figure 5.6: Thrust coefficient for rotation rate 4546 RPM.	43
Figure 5.7: Power coefficient for rotation rate 4546 RPM.	44
Figure 5.8: Efficiency for rotation rate 4546 RPM.	44
Figure 6.1: Fluid domain geometry.	46
Figure 6.2: Rotating domain detailed geometry.	46

Figure 6.3: Prism layer mesh at the plane $z=-0.02$	49
Figure 6.4: Periodic interfaces sketch.....	50
Figure 6.5: Induced velocity on the disc calculated from momentum theory.	52
Figure 6.6: Fine mesh. Blade surface mesh (Top). Volume mesh at the plane $z=-0.02$ (Bottom).	53
Figure 6.7: Standard mesh. Blade surface mesh (Top). Volume mesh at the plane $z=-0.02$ (Bottom).	53
Figure 6.8: Course mesh. Blade surface mesh (Top). Volume mesh at the plane $z=-0.02$ (Bottom).	54
Figure 6.9: Thrust coefficient convergence on fine mesh $J=0.375$	55
Figure 6.10: Power coefficient convergence on fine mesh for $J=0.375$	56
Figure 6.11: Thrust coefficient against advance ratio.	57
Figure 6.12: Power coefficient against advance ratio.....	57
Figure 6.13: Efficiency for increasing advance ratio.	58
Figure 6.14: Axial velocity distribution along the axial coordinate measured by a probe set at $z=0.75R$ and $y=0$	59
Figure 6.15: Radial velocity distribution along the axial coordinate measured by a probe set at $z=0.75R$ and $y=0$	60
Figure 6.16: Tangential velocity distribution along the axial coordinate measured by a probe set at $z=0.75R$ and $y=0$	60
Figure 6.17: Tangential velocity along the radial coordinate for a rotating volume diameter of $1.05D$	62
Figure 6.18: Tangential velocity along the radial coordinate for a rotating volume diameter of $1.1D$	62
Figure 6.19: Tangential velocity along the radial coordinate for a rotating volume diameter of $1.15D$	63
Figure 6.20: Tangential velocity along the radial coordinate for a rotating volume diameter of $1.25D$	63
Figure 6.21: Turbulent Viscosity ratio for model: $k-\omega$ SST. $z=-0.03$	64
Figure 6.22: Turbulent Viscosity ratio for model: $k-\epsilon$ Realizable . $z=-0.03$	65
Figure 6.23: Turbulent Viscosity ratio for model: Spalart-Almaras. $z=-0.03$	65
Figure 6.24: Turbulent Viscosity ratio for model: $k-\omega$ standard. $z=-0.03$	65
Figure 6.25: Back view of the propeller with pressure contours.	69
Figure 6.26: Front view of the propeller with pressure contours.	69
Figure 6.27: Thrust coefficient evolution in time for unsteady simulation.	70
Figure 6.28: Power coefficient evolution in time for unsteady simulation.	70
Figure 6.29: Back view of the propeller with pressure contours. Multiple frame of reference(Top). Unsteady(Bottom).	71

Figure 6.30: Front view of the propeller with pressure contours. Multiple frame of reference(Top). Unsteady(Bottom)	71
Figure 6.31: Axial velocity contours at $z=0$. Multiple frame of reference(Top). Unsteady(Bottom)	72
Figure 6.32: Detail of wake behind cylindrical hub in unsteady simulation.	72
Figure 7.1: Thrust coefficient for $\Omega = 4546 \text{ RPM}$	74
Figure 7.2: Power coefficient for $\Omega=4546 \text{ RPM}$	74
Figure 7.3: Efficiency for $\Omega=4546 \text{ RPM}$	75
Figure 7.4: Thrust coefficient for $\Omega=7559 \text{ RPM}$	75
Figure 7.5: Power coefficient for $\Omega=7559 \text{ RPM}$	76
Figure 7.6: Efficiency for $\Omega=7559 \text{ RPM}$	76
Figure 7.7: Thrust coefficient for different rotation rates.....	77
Figure 7.8: Power coefficient for different rotation rates.....	78
Figure 7.9: Efficiency for different rotation rates.....	78
Figure 8.1: Front view of APC 10x7 slow flyer.[1]	79
Figure 8.2: Top view of APC 10x7 slow flyer.[1]	79
Figure 8.3: Rendered Image of the CAD model of the propeller APC 10x7 Slow flyer.	80
Figure 8.4: Bottom and front views of the CAD model of the propeller APC 10x7 Slow flyer.	80
Figure 8.5: Thrust coefficient for rotation rate 3008 RPM.....	82
Figure 8.6: Power coefficient for rotation rate 3008 RPM.....	83
Figure 8.7: Efficiency for rotation rate 3008 RPM.....	83
Figure 8.8: Thrust coefficient CFD results (3008RPM) and manufacturers data(3000RPM)..	84
Figure 8.9: Power coefficient CFD results (3008RPM) and manufacturers data(3000RPM)..	85
Figure 8.10: Efficiency CFD results (3008RPM) and manufacturers data(3000RPM).	85

List of Tables

Table 5.1: Experimental Results for rotation rate 4546RPM from[1].....	45
Table 6.1: Surface mesher controls.	47
Table 6.2: Propeller surface custom controls.....	47
Table 6.3: Rotating region surface custom controls.....	47
Table 6.4: Outer region surface custom controls.	48
Table 6.5: Polyhedral mesher settings.....	48
Table 6.6: Prism Layer Settings.	49
Table 6.7: Prism Layer Controls Propeller surface.	49
Table 6.8: Example of freestream velocities for rotation rate 4546 RPM.....	50
Table 6.9: Trial Grids Characteristics.....	52
Table 6.10: Mesh refinement results.	55
Table 6.11: Relative Errors compared with experimental results.	56
Table 6.12: Region’s length sensitivity analysis.....	59
Table 6.13: Region’s Diameter sensitivity analysis.	61
Table 6.14: Results for advance ratio $J=0.375$ and different turbulence models.	64
Table 6.15: Lateral boundary condition effect on performance for $J=0.375$	66
Table 6.16: Lateral boundary condition effect on performance for $J=0.375$. Rotating domain 1.25D.	66
Table 6.17: Interface effect on performance for $J=0.375$. Rotating domain diameter=1.05D.	66
Table 6.18: Interface effect on performance for $J=0.375$. Rotating domain length=0.2D.	67
Table 6.19: Performance coefficients results of the unsteady simulation for $J=0.375$ and $\Omega = 4546 \text{ RPM}$	68
Table 7.1: Comparison between CFD and experimental results.....	73
Table 8.1: Modified propeller’s surface custom controls.....	81
Table 8.2: : Modified Prism Layer Controls for Propeller’s surface.....	81
Table 8.3: Comparison between CFD and experimental results.....	82

1 Introduction

1.1 Motivation

For many years small-scale propellers were simply used in aircraft modelling and their performance did not require a great accuracy as the models are generally light and the safety issues are not as important. Today, UAV's are state of the art technology, used in a great variety of applications including security, health, agriculture and military. This means that now that accuracy is required, it is vital to know the propeller's performance curves for the different Reynolds numbers associated to flow conditions in the flight envelope of the UAV. Reynolds number based on the chord for small scale propellers at normal rotation rates are under 100000, thus below the turbulent transition Reynolds numbers for a flat plate. Possibly the most reliable way to evaluate small scale propeller performance is through experimental testing. Comparisons between experimental and theoretical calculations show degradation in performance for low Reynolds numbers, therefore it becomes a problem to estimate performance by numerical approaches such as Blade Element Momentum Theory(BEMT). Static performance tests do not require a wind tunnel and are relatively more affordable, but advancing flow performance tests do require wind tunnel access and are therefore more limited and expensive. Another issue of experimental tests is the fact that an actual physical geometry is needed; this is a complication if the objective is propeller design and optimisation as every variation in geometry will require the manufacturing of a new propeller with the increase in cost and time this generates. Many analytical and semi-analytical model have been developed to try and simulate low Reynolds number effects. However it is still a challenge for designers to find an accurate predictive propulsive model for small scale UAV's. CFD simulations are potentially able to represent adequately the flow field around a rotating propeller and could therefore become an alternative way of assessing propeller performance. If sufficiently robust, accurate and computationally cheap CFD models were developed, they could be used for performance optimisation directly or more likely to correct semi-analytical models which could then be used for optimisation and design purposes.

A particularly interesting application could also be the characterization of the aerodynamic performance of propellers with leading edge protrusions. These protrusions are commonly found on whale's fins and generate counter-rotating chordwise vortices. Under certain flow conditions these vortices tend to delay stall with minimal effect on drag.

Another potential application of CFD simulations would be to simulate full-scale or intermediate scale propellers operating in low Reynolds numbers conditions for example the Martian atmosphere. For instance, JPL (Jet Propulsion Laboratory) is investigating the use of UAV's as Mars Rover's. They have developed a preliminary prototype shown in Figure 1.1, which has a diameter of 1.1 m. This propeller operating at 2500 RPM on The Earth will definitely generate high Reynolds numbers, around 1 million. However a representative value of kinematic viscosity in Martian atmosphere is $8.7 \cdot 10^{-4}$ around 60 times higher than the earth. This would make the Reynolds number of the flow around the blades fall into the low Reynolds numbers flow, complicating the traditional analytical codes to provide reliably results. Experimental testing in these cases is very complex and expensive, as a wind tunnel facility in which atmospheric properties (pressure, temperature, gas composition, wind flow etc.) can be reproduced is required. Therefore it would be very interesting the use of CFD

simulations to reproduce the performance of these new generation Mars rovers, saving time and money in the development of propellers.



Figure 1.1: Jet Propulsion Laboratory Helicopter.

1.2 Literature review

Full scale propeller performance has been well documented as its design has been studied for many years, this can be seen for example in reference [21], a paper on propeller performance co-written by Theodorsen in 1937. As previously mentioned, the small-scale propellers have recently gained importance since UAV's started to gain weight for aerospace applications and therefore, they are not as well documented. In the last few years the Aerospace department at the University of Illinois at Urbana-Champaign (UIUC) have performed many experimental performance tests on small scale propellers, both off the shelf propellers and 3D printed propellers and the results are available in reference [1]. Some CFD simulations are documented, but they are mainly done for marine propellers, for example Wang et al [23] report good matching between experimental and CFD results using a moving reference frame and a $k - \epsilon$ turbulence model. Morgut et al [24] included a transition sensitive turbulence model which resulted in better prediction of experimental results respect to the SST $k - \omega$ turbulence model. Morgado et al. [25] documented improvement in the accuracy of results using Reynolds Stress Modelling(RSM) compared to the SST $k - \omega$ model, incurring in higher computational costs.

Airship propellers CFD simulations are not as common, the design tools are normally semi-analytical tools incorporating stall modelling to a Blade Element Momentum Method, for example as done by Morgado et al. [26]-[28]. There are some reported CFD simulations, but they are normally limited to hovering situations. Kutty et al [17] performs an advancing flow analysis using unstructured meshing and *standard* $k - \omega$ turbulence modelling with a moving reference frame to simulate the rotation of the commercial propeller, APC 10x7 slow

flyer model. They reported reliable capability to predict performance of a low speed, low Reynolds number small-scale propeller.

2 Propellers

Propeller propulsion is, in the appropriate operating range of operation, one of the most efficient ways of providing thrust to an aircraft as it consists in giving a reduced velocity raise to a considerably big flow rate. The main problem is that with increased forward speed the efficiency drops dramatically due to velocity at the tip approaching the speed of sound. This is why for medium subsonic Mach Numbers Turboprops are selected over Turbofans but above $M=0.5-0.6$, Turbofans become more efficient and are therefore preferred. The fuel consumption of a Turbofan is however higher than a Turboprop, this is one of the reasons why there is still an active research to obtain improvement in propeller performance. Propeller propulsion has been popular since the first aircraft appeared and nowadays the increasing usage of UAV's for multiple applications is making this kind of propulsion object of development and investigation especially the smaller scale which are not as well documented as the larger scales. The next sections show an overview of the different theoretical approaches that traditionally had been used to estimate the slipstream characteristics of the flow across a propeller.

2.1 Momentum theories

Several authors contributed to these theories, starting at the British School with Rankine and Froude, then followed by the German and Russian Schools with Prandtl, Betz and Joukowski as most laureate researchers. The starting point was the development Actuator Disc theory, and then more generalisations were progressively added to finally arrive to the general momentum theory.

2.1.1 Actuator Disc Theory

This theory was originally developed for marine propellers and only considers axial momentum across the disc. In figure 2.1 a graphic description of this model is shown. This model bases on the following assumptions:

- Pressure and velocity are uniform across any plane perpendicular to the rotating axis.
- The fluid is inviscid and incompressible
- The fluid flow is stationary and irrotational
- The streamlines at the tip of the blades define the contracting stream-tube.

This theory substitutes the rotor by an infinitely thin disc, with the same diameter as the blades, which is impermeable, in other words, velocity is continuous but it can withstand a pressure difference that occurs in an abrupt manner as the fluid flow crosses the disc. Basically an axial momentum balance is done with the streamtube as the volume of control obtaining:

$$T = \dot{m}((V_{\infty} + w_j) - V_{\infty}) = \dot{m}w_j \quad (2.1)$$

Considering continuity equation along the streamtube:

$$\dot{m} = \rho A_1 V_{\infty} = \rho A_{disc} (V_{\infty} + w) = \rho A_3 (V_{\infty} + w_j) \quad (2.2)$$

An inflow parameter **a** and a slipstream parameter **b**, are usually defined as:

$$a = \frac{w}{V_\infty} \quad (2.3)$$

$$b = \frac{w_j}{V_\infty} \quad (2.4)$$

The inflow factor is sometimes called axial induction factor.

Equation 2.1 can be rewritten as:

$$T = \dot{m}(V_\infty(1 + b) - V_\infty) = \dot{m}V_\infty b \quad (2.5)$$

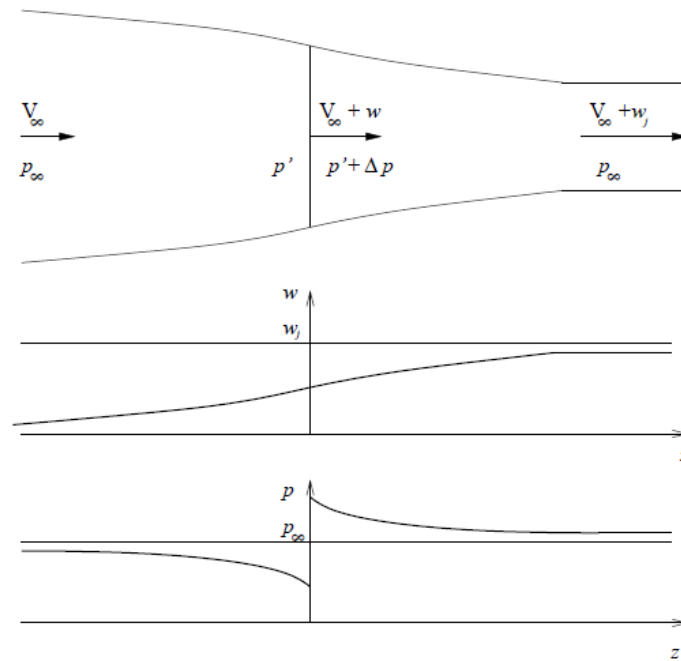


Figure 2.1: Actuator disc model and variation of relevant magnitudes.

And equation 2.2 can be rewritten as:

$$\dot{m} = \rho V_\infty (1 + a) A_{disc} \quad (2.6)$$

Substituting in equation 2.5 the thrust can be specified as:

$$T = A_{disc} \rho V_\infty^2 (1 + a) b \quad (2.7)$$

As pressure is uniform the surface integral of pressure distribution over the actuator disc could be simplified to:

$$T = \iint_{Disc} p \, dS = \Delta p A_{disc} \quad (2.8)$$

Equating equations 2.7 and 2.8 an expression for the pressure jump can be obtained:

$$\Delta p = \rho V_{\infty}^2 (1 + a) b \quad (2.9)$$

One of the assumptions of this theory is incompressibility of the flow, this allows the application of Bernouilli's Equation along any streamline in our streamtube but it cannot be applied across the actuator disc. If Bernouilli's Equation is applied twice, once between the intake section of the streamtube(Point 1) and a point just before the disc(Point f) and again between a point just after the disc(Point r) and the outlet section(Point 2) of the streamtube the following expressions are obtained.

$$p_1 + \frac{1}{2} \rho V_{\infty}^2 = p_f + \frac{1}{2} \rho V_{\infty}^2 (1 + a)^2 \quad (2.10)$$

$$p_r + \frac{1}{2} \rho V_{\infty}^2 (1 + a)^2 = p_2 + \frac{1}{2} \rho V_{\infty}^2 (1 + b)^2 \quad (2.11)$$

Taking into account that the inlet and outlet of the streamtube are far enough from the disc in order for the streamlines to be parallel to the rotation axis, which is equivalent to say that pressure is the atmospheric pressure. Adding equation 2.10 and 2.11:

$$\Delta p = p_r - p_f = \rho V_{\infty}^2 b \left(1 + \frac{b}{2} \right) \quad (2.12)$$

Now, equating 2.9 and 2.12:

$$(1 + a) b = b \left(1 + \frac{b}{2} \right) \rightarrow b = 0 \text{ and } b = 2a \quad (2.13)$$

The resultant equation provides two answers, $b=0$ which is non-physical, and $b = 2a$ which constitutes Froude's Theorem which states that for any flight speed, the induced velocity at the outlet of the streamtube by the propeller is twice the velocity induced at the disc.

$$w_j = 2w \quad (2.14)$$

The slipstream and inflow parameters can be calculated for a known thrust:

$$b = 2a = -1 \pm \sqrt{1 + 2 \frac{T}{\rho V_{\infty} A_{disc}}} \quad (2.15)$$

Considering for example a Helicopter, where $T = W$ to maintain vertical equilibrium, inflow and slipstream parameters can be calculated. Then induced velocity at the disc can be calculated and so the induced power:

$$w = aV_{\infty}, \quad P_i = Tw \quad (2.16)$$

This theory does not describe precisely the flow field near the disc as the assumptions of a discrete pressure jump and unidirectional flow do not seem fully realistic. However far away from the disc the assumptions seem reasonable and so for a known thrust and propeller diameter the induced fluid field would become more and more realistic.

2.1.2 Extended Momentum Theory

The theory discussed in the previous section was simplified and the possibility of having radial variations of axial, radial or tangential velocity was not considered. This Extended Momentum Theory still does not allow an induced radial velocity, which is equivalent to state that wake will not contract. However it does allow tangential induced velocity and also radial variations of axial and tangential velocities which allows the theory to represent considerably better the fluid flow in the vicinity of the propeller. Figure 2.2 shows a sketch of the configuration of the Extended Momentum Theory.

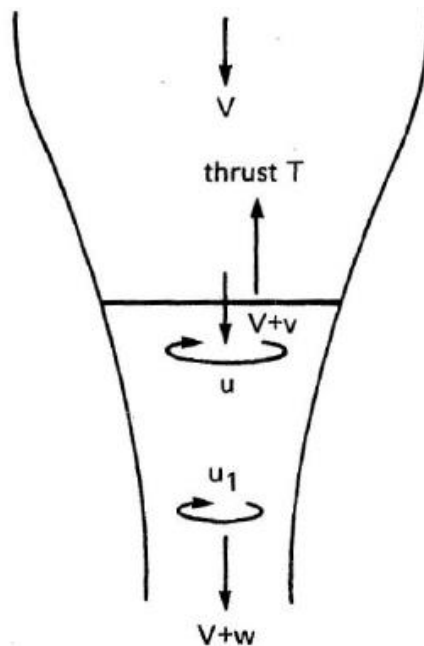


Figure 2.2: Extended momentum theory.

As radial variations in velocity are present now the adequate volume of control to apply conservation laws would be an annular differential control volume enclosed by two streamtubes placed at r and $r+dr$ and two normal planes to the rotation axis placed at z and $z+dz$. Figure 2.3 shows a sketch of this control volume.

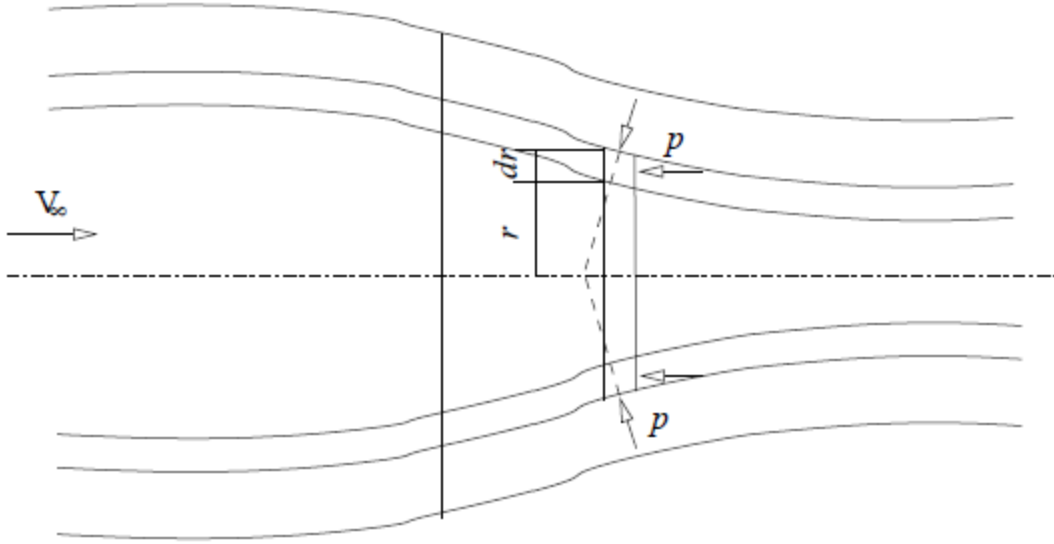


Figure 2.3: Annular differential control volume for the Extended Momentum Theory.

The steady state angular momentum conservation equation can be written, neglecting body forces and shear stresses as:

$$\int_S \rho(\vec{r} \times \vec{V}) \vec{V} \cdot \vec{n} dS + \int_S \vec{r} \times p \vec{n} dS = 0 \quad (2.17)$$

Axial symmetry in the control volume and pressure field will make the second integral in equation 2.17 to be 0. Also considering that the streamtube surfaces verify impenetrability condition:

$$\vec{V} \cdot \vec{n} = 0 \quad (2.18)$$

The only fluxes which have a non zero resultant would be those associated to the faces normal to the rotation axis. Naming the velocity vector $\vec{V} = (0, v(r), V)$ the first integral evaluated in those two faces results in:

$$-vr\rho V dA + \left[vr + \frac{\partial}{\partial z}(vr) dz \right] \left(\rho V dA + \frac{\partial}{\partial z}(\rho V dA) dz \right) = 0 \quad (2.19)$$

Equation 2.18 also implies that the mass flow is constant and so:

$$\rho V dA = constant \rightarrow \frac{\partial}{\partial z}(\rho V dA) = 0 \quad (2.20)$$

Equation 2.19 can be now simplified to:

$$\frac{\partial}{\partial z}(vr) = 0 \rightarrow vr = \omega r^2 = constant \quad (2.21)$$

Equation 2.21 represents the conservation of the magnitude vr along the z-direction. ω represents the angular velocity of the fluid volume. This value of angular velocity is definitely discontinuous across the disc being 0 upstream of the disc and $\omega = \frac{v}{r}$ downstream. This discontinuity at the disc represents the torque needed to accomplish the corresponding azimuthal induced velocity.

$$dQ = \omega r^2 \rho V dA \quad (2.22)$$

Taking into account that:

$$dA = 2\pi r dr \quad (2.23)$$

And introducing a rotational influence factor:

$$a' = \frac{\omega}{2\Omega} \quad (2.24)$$

The torque can be now expressed as:

$$dQ = 4\pi r^3 \rho V \Omega a' dr \quad (2.25)$$

Noticing that the Power can be expressed as:

$$P = \int_0^R \Omega dQ = \int_0^R 4\pi r^3 \rho V \Omega^2 a' dr = a' \Omega^2 \rho V \pi R^4 = \dot{m} a' \Omega^2 R^2 \quad (2.26)$$

2.2 Blade Element Theory

Section 2.1 shows the development of a theory based on momentum conservation equations, through which it was possible to obtain information about the fluid field using no information about the blade geometry but its radius. Even though the extended version of the momentum theory is able to provide reliable preliminary data, it seems evident that in order to design accurately propeller blades its geometry has to be included at some point. Blade Element Theory basically divides each blade in elements perpendicularly to the radial axis and assumes that the flow can be considered 2D in any element associated to a radial position. This assumption is accurate enough for preliminary design in 2 and 3 blade propellers. For more blades a cascade treatment would be required.

Usually propellers operate at very high rotation rates, this means that the aerofoil sees a very high speed in the rotation plane near the tip but this component reduces linearly to zero at the root. When the inflow speed and rotational speed are combined the relative velocity of the aerofoils is obtained, this velocity will change from almost parallel to the rotation plane at the tip to parallel to the flow direction near the root. Aerofoils have an optimum operating angle of attack, it is therefore mandatory to include in the propellers geometry a pitch angle, β . Figure 2.4 shows the geometric parameters involved in this theory.

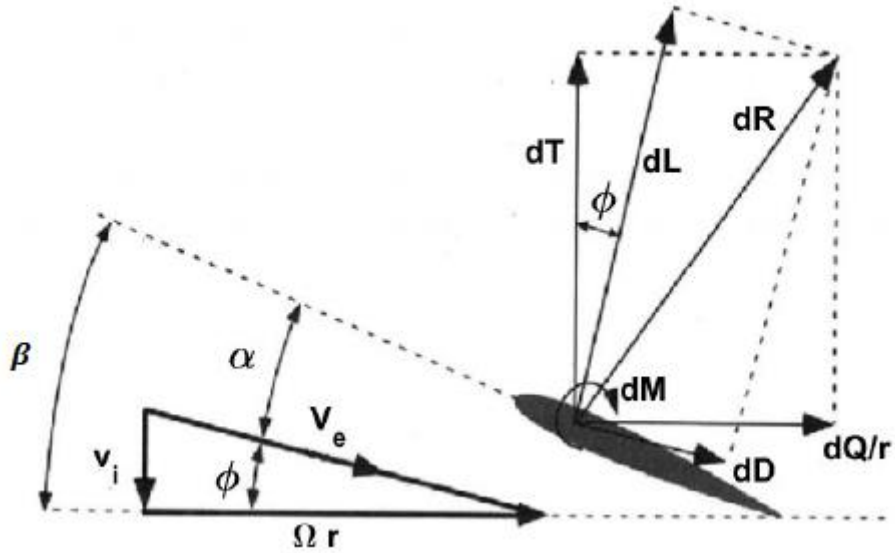


Figure 2.4: Element dr at radial position r .

From figure 2.4 some geometrical relationships can be pointed.

$$\beta = \alpha + \phi \quad (2.27)$$

$$\phi = \arctan\left(\frac{v_i}{\Omega r}\right) \quad (2.28)$$

$$\vec{V}_e = v_i \vec{e}_z + \Omega r \vec{e}_\theta \quad (2.29)$$

$$|\vec{V}_e| = \sqrt{v_i^2 + (\Omega r)^2} \quad (2.30)$$

As its appreciable in equation 2.29 there is no radial component of velocity therefore every infinitesimal element can be solved considering bidimensional flow. This results in the following aerodynamic forces:

$$\delta L(r) = \frac{1}{2} \rho V_e(r)^2 c(r) \delta r C_L(r) \quad (2.31)$$

$$\delta D(r) = \frac{1}{2} \rho V_e(r)^2 c(r) \delta r C_D(r) \quad (2.32)$$

The aerodynamic coefficients should be calculated locally at each radial coordinate r , as in general these coefficients are a function of the Reynolds and Mach numbers which vary with the radial coordinate. Looking at figure 2.4 it is clear that lift and drag are rotated an angle ϕ compared to thrust and tangential force, therefore these can be expressed as:

$$\delta T(r) = \delta L \cos(\phi(r)) - \delta D \sin(\phi(r)) \quad (2.33)$$

$$\frac{\delta Q(r)}{r} = \delta D \cos(\phi(r)) + \delta L \sin(\phi(r)) \quad (2.34)$$

If the geometry and induced velocity are known, for fixed rotation and advance speed, equations 2.33 and 2.34 can be integrated radially and multiplied by the number of blades to obtain the resultant thrust and power.

$$T = N \int_0^R \delta T(r) dr \quad (2.35)$$

$$P = N \omega \int_0^R \delta Q(r) dr \quad (2.36)$$

Equations 2.34 and 2.35 show how global magnitudes obtained by this method are directly related to the blade geometry whereas the momentum approaches where only related to the flow conditions and radius of the blades.

2.3 Vortex Theory

Vortex theory is an analysis of the rotor, considering inviscid and incompressible flow, which allows the calculation of the velocity field near the disc and in the wake. There are many approaches that make use of vortex theory, the simplest one uses the actuator disc model. The first researcher to theorise this idea was N.E. Joukowski and then was extended by A. Betz. Equation 2.28 shows that for the standard rotational speeds the inflow angle ϕ is relatively small and so the following approximations remain valid:

- $\cos(\phi) \approx 1$
- $\sin(\phi) \approx \phi$
- $\phi \approx \frac{v_i}{\Omega r}$
- $V_e \approx \Omega r$
- $dT \approx dL$

Using the Kutta-Joukowski Theorem we can calculate lift as:

$$L = \rho V_e \int_0^R \Gamma(r) dr \quad (2.37)$$

Now if the previous approximations are introduced and differentiating by the radial coordinate the equation 2.37:

$$dT \approx dL = \rho \Omega r \Gamma(r) dr \quad (2.38)$$

Equation 2.38 imply that known the radial distribution of circulation, thrust can be easily obtained by integration.

2.3.1 Constant circulation distribution, $\Gamma(r) = \text{constant}$

A constant circulation distribution is the simplest case and can be represented for a two blade rotor by a rotating horseshoe vortex with a longitudinal vortex root, this can be seen in figure 2.5.

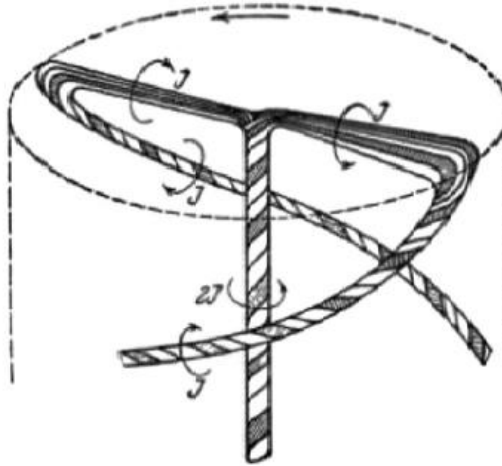


Figure 2.5: N.E Joukowski original diagram of constant circulation vortex system.

The Russian school with Joukowski as it maximum referent considered that the optimum rotor was the one with a constant circulation distribution, in fact they named this type of rotor after Joukowski and some texts still call a N.E.J Rotor to a constant circulation distribution rotor. The tip vortex filament has a helical structure due to the composition rotating motion of the blades and the axial velocity of the flow. Due to the fact that the fluid is irrotational upstream of the rotor and considering the vorticity equation for ideal flow (Equation 2.39) this flow must remain irrotational while it does not cross the rotor.

$$\frac{D\vec{\omega}}{Dt} = \vec{\omega} \cdot \nabla \vec{V} \quad (2.39)$$

This jump in vorticity when crossing the actuator disc induces a tangential velocity as shown in the general momentum theory. This velocity can be actually calculated for the case of infinite blade rotor by decomposing the vortex system into 4 elemental vorticity distributions:

- A vortex filament of intensity Γ aligned with the rotation axis(root vortex)
- A radial distribution of vortex filaments over the actuator disc(Infinite blades) with an intensity density of $\gamma = \frac{\Gamma}{2\pi r}$
- A tube formed by vortex rings Γ parallel to the plane of the rotor.(Figure 2.6)
- A tube formed by longitudinal vortices, perpendicular to vortex rings and with a total intensity equal to the root vortex, therefore the intensity density of the filaments would be, $\gamma = \frac{\Gamma}{2\pi R}$.(Figure 2.6)

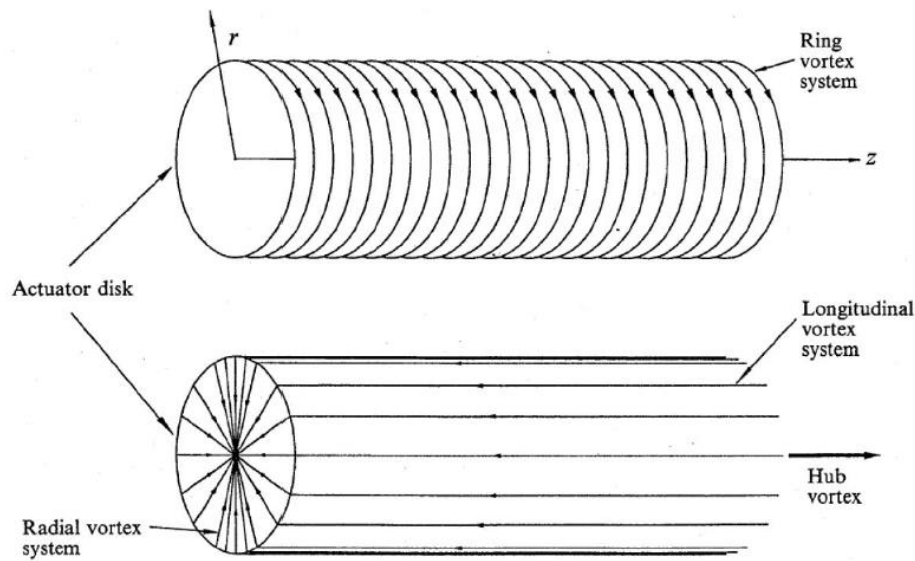


Figure 2.6: Vortex system of the actuator disc ($N \rightarrow \infty$) with constant circulation.

Adding up all this contributions the final induced tangential velocity is obtained. The root vortex induces the following tangential velocity:

$$u_{root}(r) = \frac{\Gamma}{4\pi r} \quad (2.40)$$

The velocity induced by the radial filament distribution forming the blades upstream of the rotor is equal to:

$$u_{upstream_b} = -u_b \quad (2.41)$$

However as the flow is rotational upstream of the disc so the tangential velocity must be cancelled with the tangential velocity induced by the root vortex:

$$u_{upstream} = u_{upstream_b} + u_{root} = 0 \quad (2.42)$$

Therefore:

$$u_b = u_{root} \quad (2.43)$$

And the velocity expressed on equation 2.43 is the velocity induced by the radial filaments distribution downstream of the disc, and so the total tangential velocity induced by the disc can be written as:

$$u(r) = u_b + u_{root} = 2u_{root} = \frac{\Gamma}{2\pi r} \quad (2.44)$$

And finally considering that the radial distribution has no effect infinitely downstream, the induced velocity here would be:

$$u_{\infty}(r) = u_{root} = \frac{\Gamma}{4\pi r} = \frac{u(r)}{2} \quad (2.45)$$

It can be shown that the longitudinal distribution has no effect on the inside of the wake [13]. In the limit of infinite blades it can also be shown that axial velocity is not affected by the radial distribution of vortices, as two opposing radial filaments will induce opposite axial velocities and so they will cancel, extending this idea to the whole disc, the result is immediate. Therefore the only vortices that contribute to axial velocity are those in de vortex rings, these have intensity per unit length of:

$$\gamma_{rings} = \frac{\Gamma}{h} \quad (2.46)$$

Where h is the distance the wake covers in one revolution:

$$h = \frac{2\pi}{\Omega} w_i \quad (2.47)$$

Where v_i is the axial velocity induced by the disc. Combining equations 2.46 and 2.47:

$$\gamma_{rings} = \frac{\Gamma\Omega}{2\pi w_i} \quad (2.48)$$

Going back to equation 2.38, as the circulation is constant, this can be integrated to obtain:

$$T = \frac{\rho\Omega r^2\Gamma}{2} = \frac{\rho\Omega A\Gamma}{2\pi} \quad (2.49)$$

So equation 2.48 can be now rewritten as:

$$\gamma_{rings} = \frac{T}{A\rho w_i} \quad (2.50)$$

It can be shown[12], that a distribution of vortex rings starting at z_1 and ending at z_2 , produces a velocity potential at a point X on the surface of the disc of:

$$\phi_X = \frac{\gamma_{rings}}{4\pi} \int_{z_1}^{z_2} \omega dz \quad (2.51)$$

Where ω is the solid angle at point X respect to the vortex ring in position z. Applying the velocity potential definition, equation 2.51 can be transformed to:

$$v_i(X) = \frac{d\phi_X}{dz} = \frac{\gamma_{rings}}{4\pi} \int_{\omega_1}^{\omega_2} d\omega \quad (2.52)$$

Integrating equation 2.52 from the disc to infinitely downstream and inserting the result in equation 2.50:

$$v_i(X) = \frac{T}{2A\rho v_i(X)} \quad (2.53)$$

Where the induced axial velocity can be written as:

$$v_i(X) = \sqrt{\frac{T}{2A\rho}} \quad (2.54)$$

Which is the same result described by the actuator disc momentum theory seen in the previous section.

Section 2.3.1 describe the velocity induce for a constant vortex intensity, however this is a particular case, there is a more general procedure where vortex intensity is considered a radial function that will be outlined in the following section.

2.3.2 Radial circulation distribution, $\Gamma(r)$

In order to verify Bjerkness-Kelvin Theorem(2.56), when there is a radial variation of circulation a vortex filament is emitted. The ensemble of all these vortices generates a helical surface that is convected downstream. These surface forms an angles ϕ with the plane of the disc that can be expressed as:

$$\phi = \arctan\left(\frac{w_i}{\Omega r - \frac{u}{2}}\right) \quad (2.55)$$

This surface will be a continuous surface in the case of infinite number of blades. Bjerkness-Kelvin Theorem states that in absence of viscous forces circulation will remain constant:

$$\frac{D\Gamma}{Dt} = 0 \quad (2.56)$$

In order to accomplish this theorem the intensity of the vortex filaments leaving the blade should be equal to the variation of the circulation for that r coordinate, with opposite sign. For one revolution of the rotor, the vortex intensity of these cylindrical surfaces generated at each r coordinate can be expressed as:

$$\gamma(r) = -\frac{d\Gamma}{dr} \frac{1}{h} = -\frac{d\Gamma}{dr} \frac{\Omega}{2\pi w_i} \quad (2.57)$$

Equation 2.44 is still valid so the tangential velocity downstream of the rotor can be expressed as:

$$u(r) = \frac{\Gamma(r)}{2\pi r} \quad (2.58)$$

Applying Bernouilli's equation in a similar way as done for equation 2.12, but taking into account the induced axial velocity the pressure jump across the disc can be calculated as:

$$\Delta p = \rho \left(2w_i - \frac{u^2}{2} \right) \quad (2.59)$$

Thrust can be obtained by:

$$dT = 2\pi\rho \left(2w_i - \frac{u^2}{2} \right) r dr \quad (2.60)$$

Also it can be obtained by the Kutta-Joukowski Theorem as:

$$dT = \rho V_e \Gamma dr \quad (2.61)$$

Equating 2.60 and 2.61, introducing as well 2.58 circulation can be obtained:

$$\Gamma(r) = \frac{4\pi w_i^2}{\Omega} \quad (2.60)$$

This in general would be dependent on the radial coordinate as the induced axial velocity will.

3 Propeller performance

Fixed pitch propeller performance is dependent, apart from the specific geometry of the propeller, on the following parameters:

- Propeller diameter(D)
- Inflow velocity(V)
- Fluid density(ρ)
- Fluid dynamic viscosity(μ)
- Rotation rate(n)
- Speed of sound(a)

Carrying out a dimensional analysis the performance results to be dependent only by three non-dimensional parameters:

- Advance ratio:

$$J = \frac{V}{nD} \quad (3.1)$$

- Reynolds number:

$$Re = \frac{\rho n D^2}{\mu} \quad (3.2)$$

- Mach Number:

$$M = \frac{nD}{a} \quad (3.3)$$

The two independent magnitudes that measure propeller performance are:

- Thrust(T)
- Torque(Q)

Thrust and Torque can be expressed as the following non-dimensional coefficients as:

- Thrust coefficient(C_T):

$$C_T = \frac{T}{\rho(nD)^2 D^2} = \frac{T}{\rho n^2 D^4} \quad (3.4)$$

- Torque coefficient(C_Q):

$$C_T = \frac{Q}{\rho(nD)^2 D^3} = \frac{Q}{\rho n^2 D^5} \quad (3.5)$$

Two other interesting variables, derived from Thrust and Torque, to assess propeller performance are Power and Efficiency.

$$P = \Omega Q = 2\pi nQ \quad (3.6)$$

$$\eta = \frac{TV}{P} \quad (3.7)$$

The Power coefficient can be defined as:

$$C_P = \frac{P}{\rho n^3 D^5} = \frac{2\pi nQ}{\rho(nD)^2 nD^3} = 2\pi \frac{Q}{\rho n^2 D^5} = 2\pi C_Q \quad (3.8)$$

Efficiency is already non-dimensional and can be written as:

$$\eta = \frac{TV}{P} = J \frac{C_T}{C_P} \quad (3.9)$$

The general performance of a propeller is defined by the functional curves $C_T = C_T(J, Re, M)$ and $C_Q = C_Q(J, Re, M)$. However normally there is just one or two of the parameters. Three different scenarios can arise which simplify considerable the study of the propeller performance:

- **Low speed and/or very small scale propellers.** This would imply low Reynolds numbers and normally low Mach numbers too. Therefore the performance would be dependent only on the Reynolds Number and Advance ratio as the compressibility effects would be negligible. $C_T = C_T(J, Re)$ and $C_Q = C_Q(J, Re)$.
- **Full scale propellers in incompressible flow conditions(M<0.3).**In this case compressibility effects are negligible as well as viscous effects due to the rise of the Reynolds number. $C_T = C_T(J)$ and $C_Q = C_Q(J)$.
- **Full scale propellers in compressible flow conditions(M>0.3).** As the velocity increases compressibility effects become important and so the Mach number influence needs to be considered. $C_T = C_T(J, M)$ and $C_Q = C_Q(J, M)$.

In this text the first scenario is appropriate as the propellers in consideration are for small UAV's applications and their diameter are only a few inches. If martian atmosphere applications are considered, the dependence of the performance coefficients with all three parameters have to be taken into account as the density is so low that very large rotational rates are required to generate thrust, this combined with the fact that the speed of sound on Mars is lower than on Earth generates high Mach numbers and therefore appreciable compressibility effects. This is also true for very high altitudes.

3.1 Expected theoretical performance

This section presents the application of some of the different theories discussed in the previous chapter to propeller performance. Specifically momentum theories and BEM method are going to be assessed.

3.1.1 Momentum Theory Performance

Results from both, the general momentum Theory and the actuator disc theory will be analysed in this section.

3.1.1.1 Actuator disc theory

Going back to the main results of this theory seen in section 2.1.1, it is possible to express the ratio of the induced velocity to the freestream velocity by combining equations 2.15 and 2.16

$$\frac{w_i}{V_\infty} = a = -\frac{1}{2} \pm \sqrt{\frac{1}{4} + \frac{T}{2\rho V_\infty A_{disc}}} \quad (3.10)$$

Doing an energy balance it is clear that the total power induced by the propeller to the system can be expressed as:

$$P = T(V_\infty + w_i) = TV_\infty(1 + a) \quad (3.11)$$

And from this power, the only useful power for propulsion would be.

$$P_{useful} = TV_\infty \quad (3.12)$$

Therefore efficiency can be defined as:

$$\eta = \frac{P_{useful}}{P} = \frac{1}{1 + a} \quad (3.13)$$

The inflow factor a can be written in terms of the advance ratio and thrust coefficient as:

$$a = -\frac{1}{2} \pm \sqrt{\frac{1}{4} + \frac{2C_T}{\pi J^2}} = a(C_T, J) \quad (3.14)$$

Equations 3.13 and 3.14 show how the efficiency depends only on the thrust coefficient and advance ratio.

$$\eta = \frac{1}{1 + a} = \eta(C_T, J) \quad (3.15)$$

However there would be an implicit dependence on the Reynolds number behind the thrust coefficient, recovering the results in the previous section.

$$C_T = C_T(Re, J) \rightarrow \eta = \eta(Re, J) \quad (3.16)$$

3.1.1.2 General momentum theory

Similarly as done in section 3.1.1.1 an energy balance can be done:

$$P = T(V_\infty + w_i) + P_{rot} \quad (3.17)$$

Where an extra term is included which represents the rotational kinetic energy associated to the tangential induced velocity present in this extended theory. This extra power can be expressed as:

$$P_{rot} = \int_0^R \frac{1}{2} (\omega r)^2 d\dot{m} \quad (3.18)$$

As in section 2.1.2 an annular differential control volume is being used, therefore the mass flow can be expressed as:

$$d\dot{m} = \rho w_i 2\pi r dr \quad (3.19)$$

And so the integral results in:

$$P_{rot} = \int_0^R \rho w_i \pi \omega^2 r^3 dr = \rho w_i \frac{\pi \omega^2 R^4}{4} = \dot{m} \frac{D^2}{16} \omega^2 \quad (3.20)$$

Introducing the rotational interference factor as in section 2.1.2 this power results in:

$$P_{rot} = \dot{m} \frac{D^2}{4} \Omega^2 a'^2 \quad (3.21)$$

Apart from equation 3.17 the total power can also be obtained through integration of the torque force as done in equation 2.26. Equating these two:

$$P = T(V_\infty + w_i) + \dot{m} \frac{D^2}{4} \Omega^2 a'^2 = \dot{m} \frac{D^2}{4} \Omega^2 a' \quad (3.22)$$

From which the following relationship can be obtained:

$$P = T(V_\infty + w_i) + Pa' \quad (3.23)$$

And therefore the total power can be expressed as:

$$P = \frac{T(V_\infty + w_i)}{1 - a'} \quad (3.24)$$

Now, it is possible to define the efficiency as:

Combining equations 2.33-2.36 and adapting them to the new notation:

$$T = N \int_0^R [dL \cos(\phi + \alpha_i) - dD \sin(\phi + \alpha_i)] dr \quad (3.27)$$

$$P = N \omega \int_0^R [dD \cos(\phi + \alpha_i) + dL \sin(\phi + \alpha_i)] r dr \quad (3.28)$$

And introducing equations 2.31 and 2.32:

$$T = N \int_0^R \left[\frac{1}{2} \rho V_e^2 c C_L \cos(\phi + \alpha_i) - \frac{1}{2} \rho V_e^2 c C_D \sin(\phi + \alpha_i) \right] dr \quad (3.29)$$

$$P = N \omega \int_0^R \left[\frac{1}{2} \rho V_e^2 c C_L \sin(\phi + \alpha_i) + \frac{1}{2} \rho V_e^2 c C_D \cos(\phi + \alpha_i) \right] r dr \quad (3.30)$$

Taking into account the following geometrical relationships:

$$V_R^2 = V_\infty^2 + (\omega r)^2 \quad (3.31)$$

$$V_e^2 = V_R^2 \cos(\alpha_i)^2 = (V_\infty^2 + (\omega r)^2) \cos(\alpha_i)^2 \quad (3.32)$$

Equations 3.29 and 3.30 can be written in its non-dimensional form:

$$C_T = \frac{\pi}{8} \int_{r_0}^R \left(J^2 + \pi^2 \left(\frac{r}{R} \right)^2 \right) \left(\frac{Nc}{\pi R} \right) \cos(\alpha_i)^2 [C_L \cos(\phi + \alpha_i) - C_D \sin(\phi + \alpha_i)] dr \quad (3.33)$$

$$C_P = \frac{\pi}{8} \int_{r_0}^R \left(J^2 + \pi^2 \left(\frac{r}{R} \right)^2 \right) \left(\frac{Nc}{\pi R} \right) \cos(\alpha_i)^2 [C_L \sin(\phi + \alpha_i) + C_D \cos(\phi + \alpha_i)] \frac{r}{R} dr \quad (3.34)$$

This α_i angle represents, in this formulation of the Blade Element Momentum Method, the first link between the two theories. The second link would be to equate thrust and power for each dr element from both theories. The iterative process is clarified in Figure 3.2. This algorithm has to converge to a constant α_i at each radial station, obtaining $\alpha_i(r)$. Then the integral to calculate the performance coefficients can be computed.

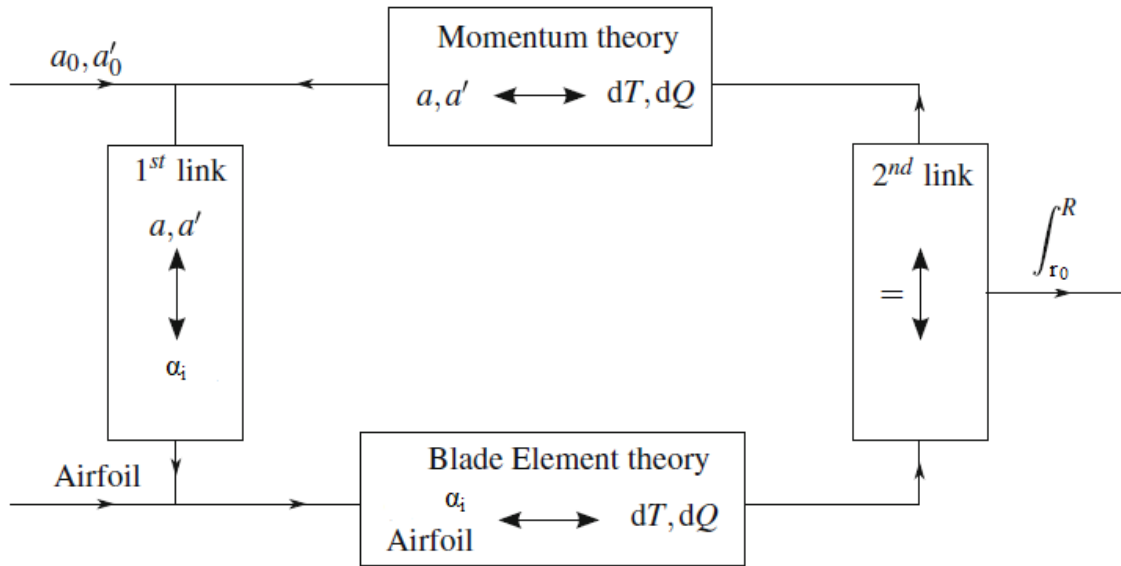


Figure 3.2: Blade element momentum method iteration loop.

3.2 Reynolds Number effects

The Reynolds number has a considerable influence in propeller performance, mainly due to the behaviour of the boundary layer. Propellers do not operate always in design conditions, this mean that sometimes the angles of attack that some sections of the blade see are high and flow separation can occur. When the boundary layer is laminar, separation is easier to achieve and a laminar recirculation bubble forms which influences the performance coefficients. In this text the Reynolds number is defined considering as the reference velocity, the rotational speed and as reference length as the chord at 75% of the half span.

$$Re = \frac{\rho V c_{0.75}}{\mu} \quad (3.35)$$

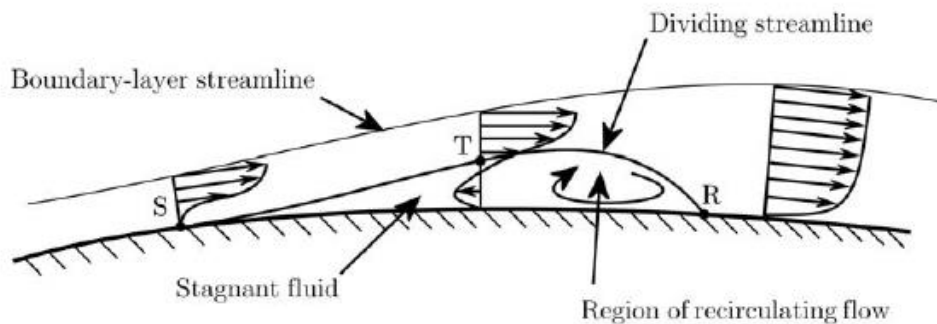


Figure 3.3: Laminar recirculation bubble region from McGranaham[14].

The use of rotational speed to compute Reynolds Number is not exact, however the induced velocity is not known but it is relatively small compared with the rotational speed. Figure 3.4 shows that how the advance ratio barely affects the Reynolds number distribution.

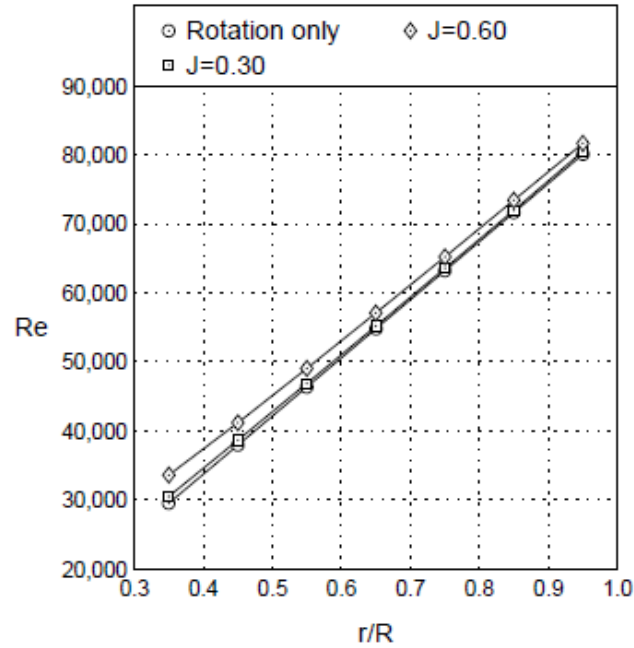


Figure 3.4: Reynolds Number variation for DA4002 9x6.75 propeller at 5000RPM from[5].

Experimental tests carried out by [5] show how efficiency of small propellers have maximum efficiencies of around 70% however literature agrees that a well-designed full-scale propeller should have a propulsive efficiency around 85%. This difference reinforces the need to find an accurate way to evaluate the real performance of small-scale propellers for which standard numerical methods such as BEM are not able to predict. Figures 3.5-3.7 show the performance of a simple rectangular propeller with a constant pitch of 6.75 inches, designed by [5], prototype DA4002, which was designed for a diameter of 9 inches. Data was obtained from UIUC Propeller database[1].

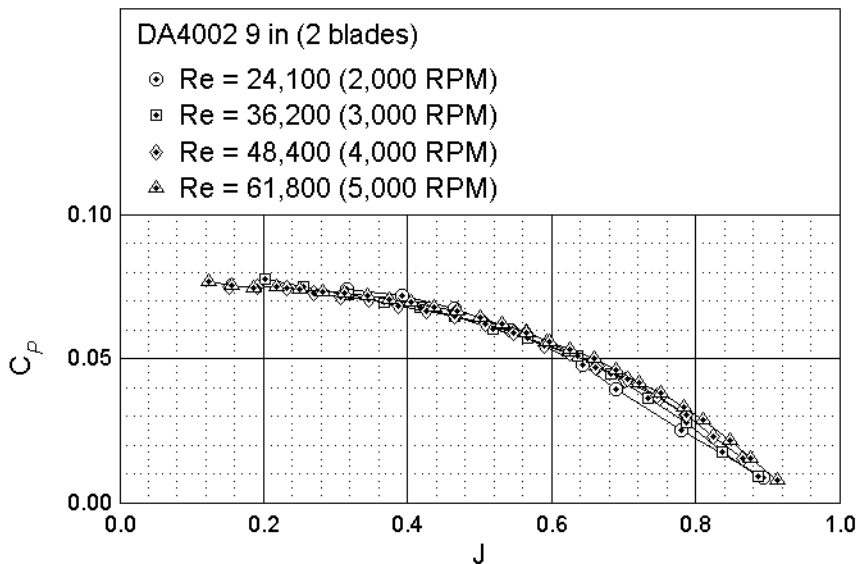


Figure 3.5: Power coefficient DA4002 9-inches.

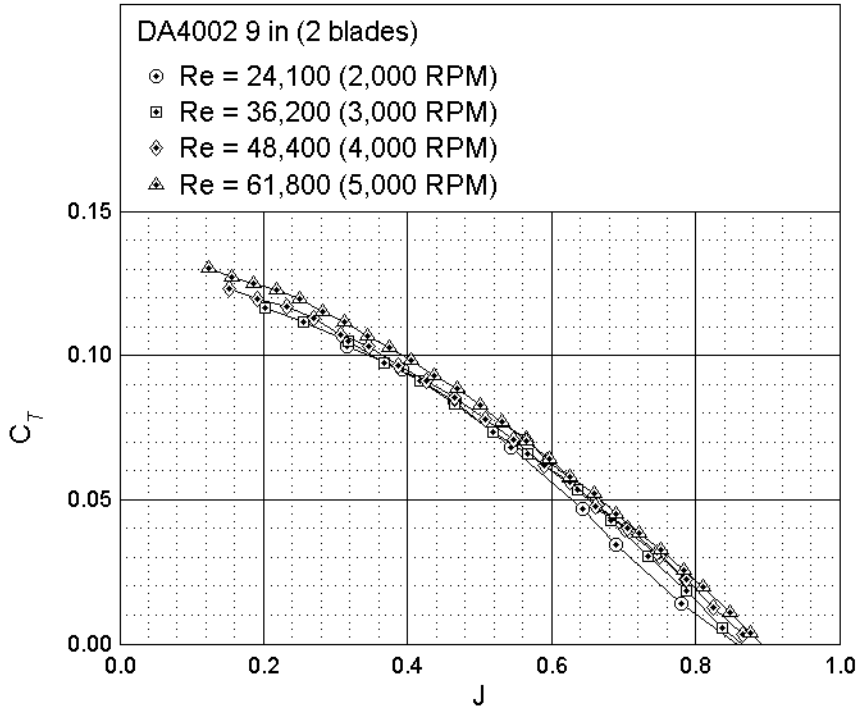


Figure 3.6: Thrust coefficient DA4002 9-inches.

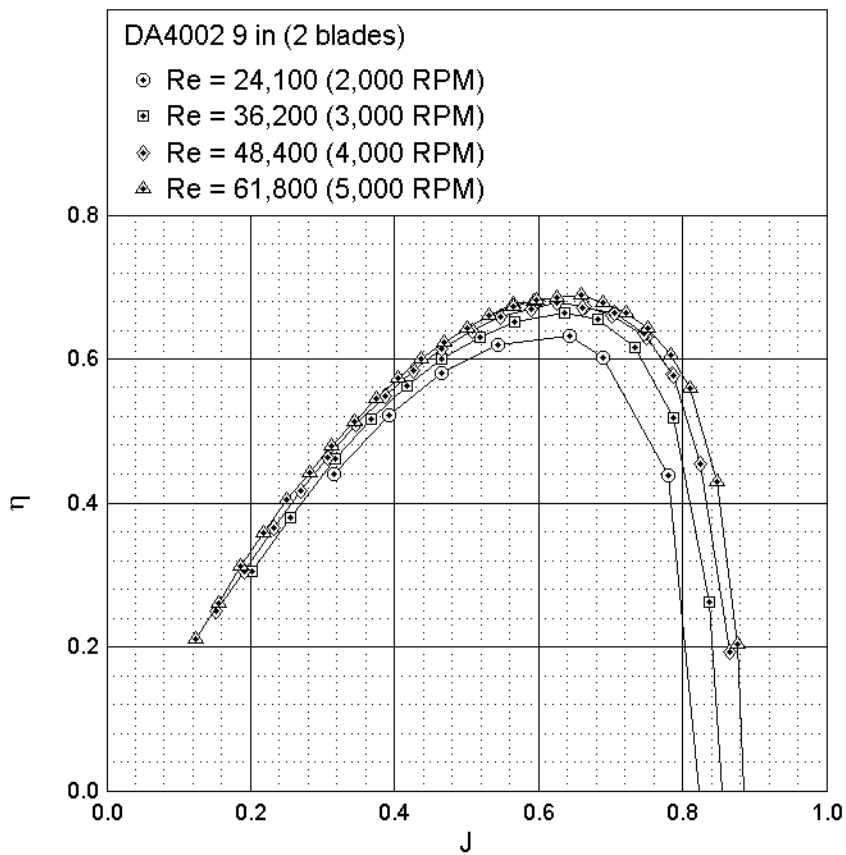


Figure 3.7: Efficiency DA4002 9-inches.

For this propeller, the effect of the Reynolds number on the power coefficient for low advance ratios is to decrease for increasing Reynolds Numbers and for high advance ratios to increase for increasing Reynolds Number. To explain this lets first note that going back to equation 3.30, it is possible to say that when drag coefficient decreases power coefficient decreases and when lift coefficient increases power coefficient increases. With increasing Reynolds number the drag coefficient tends to drop and the lift coefficients tend to raise, the decrease in drag coefficient is higher than the increase in lift for small advance ratio this is why for low advance ratios the power coefficient decreases with Reynolds Number, the opposite occurs for high advance ratios. This can be seen in figures 3.8-3.9 which show the variation of drag and lift coefficient distributions for two different rotation rates and therefore to different Reynolds Number. Nevertheless the overall effect is not as important as for the thrust coefficient where for all advance ratios increasing the Reynolds number produces an increase in the thrust coefficient. This is the reason why increasing the Reynolds Number always produces an increase in efficiency. This is the case for this propeller in particular, these trends may change for different propellers due to the strong coupling between lift and drag and the sensitivity of the coefficients to different pitch distributions. Nevertheless the efficiency is always increased for increasing Reynolds numbers, either by an increase on the power coefficient or by a decrease in the drag coefficient as checked for the propeller tested by [5].

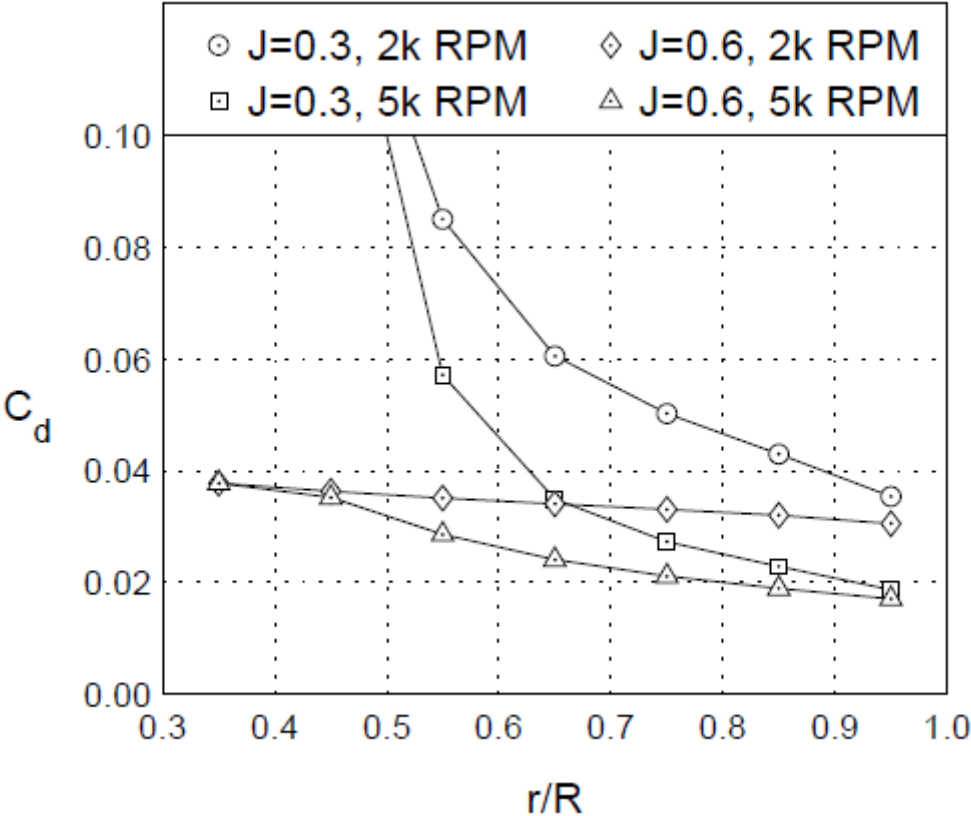


Figure 3.8: Drag Coefficient distribution along the span for DA4002 9x6.75. Deters[5].

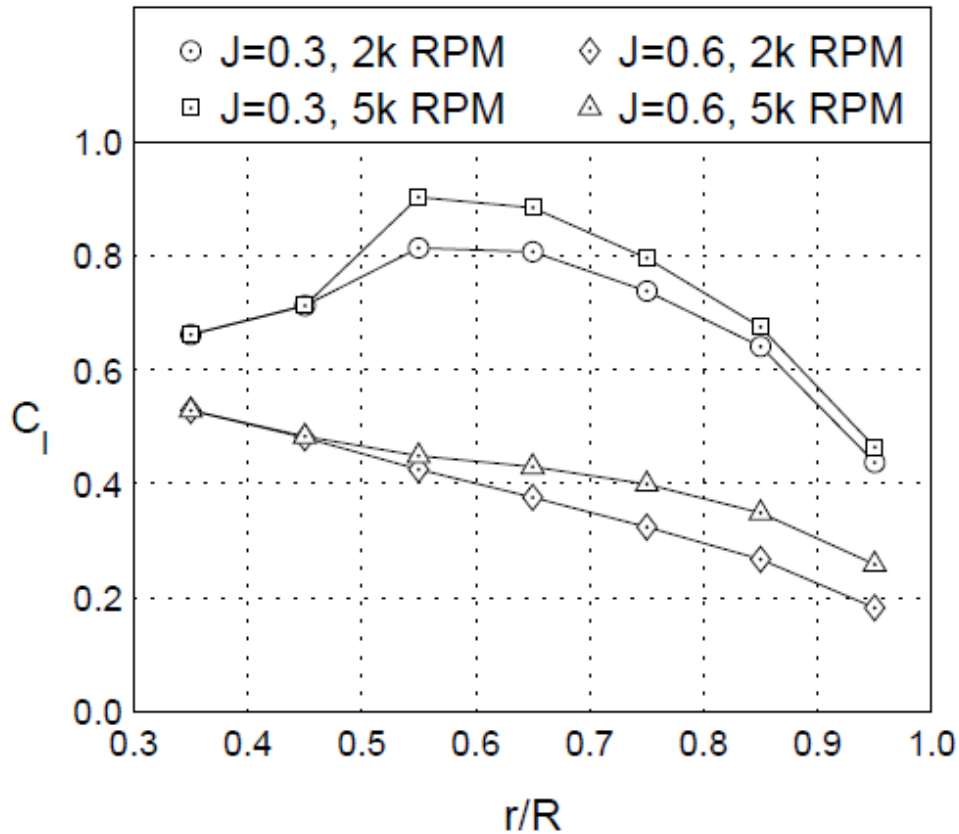


Figure 3.9: Lift Coefficient distribution along the span for DA4002 9x6.75. Deters[5].

3.3 Pitch angle variation

Although only fixed pitch propellers are considered in the following chapters, it is interesting to point out that these coefficients are extremely sensitive to pitch variation, and sometimes a small error fixing the blades to the hub, manufacturing not being precise and/or aeroelastic effects for high rotation rates can generate significant discrepancies in the performance curves. Figure 3.10 shows how increasing the pitch produces a lower efficiency for low advance ratios but as the advance ratio grows, the efficiency becomes bigger (for this propeller, with this pitch values) and more importantly the maximum is reached for a higher advance ratio. This is an expected result as increasing pitch requires a higher advance ratio in order to achieve an optimum angle of attack of the profile. For very thin blades, aeroelastic effects become more important and pitch tends to increase as the rotational speed increases, this increase in pitch as shown in figure 3.10 decreases the efficiency of the propeller for low advance ratios and may mask the increase in efficiency due to the Reynolds Number effects commented on the previous section. In order to individuate the appearance of aeroelastic phenomena efficiency curves should be checked to see if the advance ratio for which the maximum efficiency is obtained varies considerably or not when the rotation rate, and therefore the Reynolds Number, is increased.

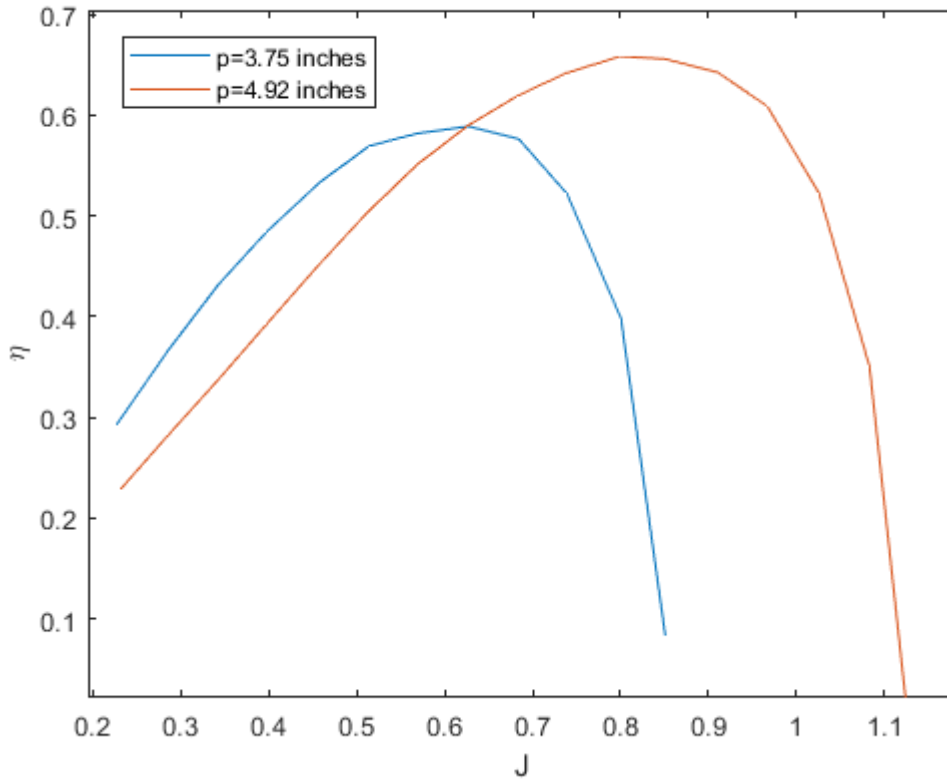


Figure 3.10: Pitch influence on efficiency for DA4002 5xp.

3.4 Stall aerofoil characteristics

In order to explain the behaviour of the performance coefficients it is mandatory to understand what happens to an aerofoil when the maximum lift angle of attack is exceeded. Recalling equations 2.27-2.28 it is clear that increasing the rotational speed tends to increase the angle of attack of the blade sections and increasing the advance ratio to decrease it. There are some off-design operating conditions that imply some sections of the blades being stalled. For a constant angular velocity and low advance ratios the flow is arriving almost in the tangential direction being the angles of attack along the blade large, therefore there is a risk of stalling. As the advance ratio increases these angles of attack are reduced, this increases efficiency up to a certain point then the angles of attack are too low and almost no thrust is being generated creating a drop in efficiency and eventually thrust reversal. Introducing 3.33 and 3.34 into 3.9 and differentiating the efficiency of a blade element can be expressed as:

$$\eta = \frac{J [C_L \cos(\phi + \alpha_i) - C_D \sin(\phi + \alpha_i)]}{[C_L \sin(\phi + \alpha_i) + C_D \cos(\phi + \alpha_i)] \frac{r}{R}} \quad (3.36)$$

Most operating conditions verify $V_e \ll \Omega R$ so in first approximation the expression for the efficiency can be simplified as:

$$\eta = \frac{J [C_L - C_D(\phi + \alpha_i)]}{[C_L(\phi + \alpha_i) + C_D] \frac{r}{R}} = \frac{JR}{r} \frac{E - \frac{V_\infty(1+a)}{\Omega r}}{E \frac{V_\infty(1+a)}{\Omega r} + 1} = \frac{JR}{r} \frac{E - \frac{JD(1+a)}{2\pi r}}{E \frac{JD(1+a)}{2\pi r} + 1} \quad (3.37)$$

Where E is the aerodynamic efficiency. This explains the importance of stalled blade elements on the performance of the propellers, as stalling is characterised by a great drop in lift, followed up by an increase in drag which reduces dramatically the aerodynamic efficiency.

Aerofoil stall behaviour differs considerably from one to another and is very dependent on the Reynolds number. For low Reynolds numbers stall tend to happen at lower angles of attack. Aerofoils forming the blades of small scale propellers are generally specifically designed for low Reynolds number, for example the Eppler 63 used in the APC slow flyer modelled in chapter 8. This very thin aerofoil for example, at a Reynolds number of 50000, have a very low maximum lift angle of attack around 6°, however stall presents with a very low drop and then the flow is reattached and continues to increase its lift until approximately 10° where the flow completely detaches and a big drop of lift occurs. Another typically used aerofoil is the Clark Y, this one is considerably thicker, about 12% of the chord, presents a maximum lift coefficient at an angle of attack of 12° and is followed by a mild drop until about 16° where the flow completely detaches. The selection of an adequate aerofoil is vital for the performance characteristics of propellers not only to have a high efficiency but to be able to operate in a wide range of conditions, particularly for fixed pitch propellers, which necessarily have to operate in off-design conditions.

4 CFD simulation of Rotating flows

The main goal of this chapter is to give an overview of the different methods embedded in the commercial CFD software STAR CCM+ to model rotating flows, especially the flow around small scale propellers at low Reynolds Numbers. There are many ways to simulate rotating flows in STAR CCM+; Momentum-based approaches and volumetric body forces approaches are simple methods that may be able to give preliminary data about propeller performance, but they do not require fine meshes to represent adequately the propeller geometry. Conversely, more complex methods require precise meshing, especially to capture geometry at the leading edge, and thus large computational power. Within these complex methods, two kinds of approaches can be distinguished: steady state approaches and unsteady approaches.

4.1 Solvers selection

4.1.1 Steady state approaches

Constant rigid body motion can be solved using steady state approaches even though it is clear that the flow field will be unsteady. These approaches profit from the use of moving frames of reference which can be translating and/or rotating. If the moving elements are placed in a control volume which is associated to a non-stationary frame of reference, time averaged characteristics of the flow can be computed. However, as this is done with a steady state analysis, it is not possible to obtain time accurate results. In order for this method to give reasonable results the volume surrounding the rotating region has to be axisymmetric and the freestream velocity should be parallel to the axis of rotation. These approaches are useful when average values are important and transient effects are minor, such as the nominal operation of turbomachinery or performance of propellers. Within steady state approaches we can distinguish two different methods, the Multiple Frame of Reference Approach (MFRA or frozen rotor) and the Mixing Plane Approach (MPA). The difference between these two is essentially the way of treating the interfaces between the rotating and static regions. When the relative position of the blades is important, such as the rotor-stator interaction of a compressor, the frozen rotor approach has the problem that the solution will be dependent on the initial relative position of the two elements. This can be solved by running the code for different relative positions and then averaging. However a much better solution would be to use a mixing plane approach, which instead of using a direct interface at the boundaries uses an indirect mixing plane which averages circumferentially the flow variables, this eliminates the relative position dependence. Figure 4.1 shows the rotor-stator passage where the mixing plane approach is used.

It is important to point out that these approaches have static meshes. The grid fluxes are calculated according to the appropriate reference frame but the grid itself does not move. Also, it is worth mentioning that these methods try to solve an unsteady problem with a steady approach, so that some time related terms in the balance equation are not being considered. If these terms are big enough, simulations may have convergence problems and/or yield non-physical solutions. Steady state Navier-Stokes equations are presented in the following lines for both frames of reference.

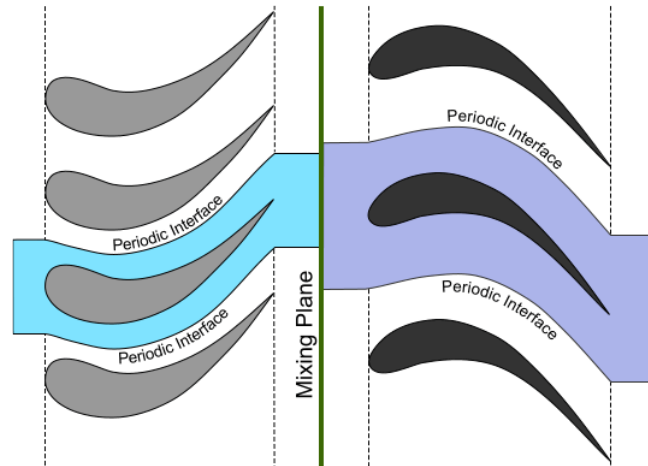


Figure 4.1: Turbomachinery simulation using mixing plane approach[15].

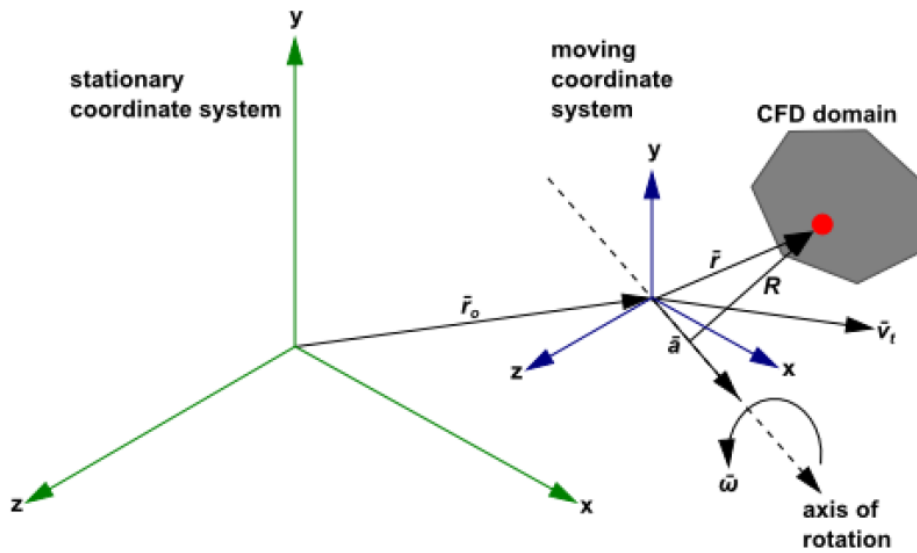


Figure 4.2: Coordinate system in static and rotating frames of reference [7].

Absolute velocity can be written in terms of the relative velocity as:

$$\vec{v} = \vec{v}_r + (\vec{\omega} \times \vec{r}) + \vec{v}_t \quad (4.1)$$

Where \vec{v}_r and \vec{v}_t are the relative rotational and translational velocities. Original steady state incompressible Navier-Stokes in conservative form can be expressed as:

$$\nabla \cdot (\rho \vec{v}) = 0 \quad (4.2)$$

$$\nabla \cdot (\rho \vec{v} \vec{v}) = -\nabla p + \mu \nabla \cdot \nabla (\vec{v}) \quad (4.3)$$

Navier-Stokes can also be expressed in the rotating frame of reference as:

$$\nabla \cdot (\rho \vec{v}) = 0 \quad (4.4)$$

$$\nabla \cdot (\rho \vec{v}_r \vec{v}) + \rho(\vec{\omega} \times \vec{v}) = -\nabla p + \mu \nabla \cdot \nabla(\vec{v}) \quad (4.5)$$

Finally the governing equations can be written in terms of relative velocity as:

$$\nabla \cdot (\rho \vec{v}_r) = 0 \quad (4.6)$$

$$\nabla \cdot (\rho \vec{v}_r \vec{v}_r) = -\nabla p + \mu \nabla \cdot \nabla(\vec{v}_r) - \rho(2\vec{\omega} \times \vec{v}_r) - \vec{\omega} \times \vec{\omega} \times \vec{r} \quad (4.7)$$

The two extra terms present in equation 4.7 represent Coriolis and Centripetal accelerations due to the non-inertial reference frame. These extra terms make the selection of the rotating domain enclosing the propeller critical. If the rotating domain is too small and therefore interfaces are close to the propeller, unphysical velocity distributions will be generated in the vicinity of the interfaces which separate the two regions. This domain selection will be addressed in more detail in section 6.3. STAR CCM+ uses the absolute velocity formulation shown in equations 4.4-4.5.

4.1.2 Unsteady approaches

These approaches involve grid movement. STAR CCM+ provides different ways of defining mesh motion: Rigid Body Motion (RBM), mesh morphing, Dynamic Fluid Body Interactions (DFBI) and Solid displacement. All of these are very demanding computationally, but if transient simulations need to be done this is the only way. Rigid Body Motion is the simplest approach that could be applied to simulate propeller rotation, and it is the one we are going to follow on this text. Dynamic Fluid Body Interactions (DFBI) would also be a possibility to simulate rotating flows. Its use is justified when the rigid body motion is driven by the flow. In this case the governing equations for rigid body motion are integrated to simulate the motion generated in response to the pressure and shear forces the fluid exerts on the body. Solid displacement motion is used along with the solid stress model to allow the solid mesh to deform responding to the forces that the fluid exerts on the solid mesh. It is justified for simulations involving interaction between the fluid and structure. Mesh morphing motion rearranges mesh vertices in response to the movement of control predefined control points. Control points and the displacements of these are used to modify the position of the vertices of the mesh. More information can be found in reference [15].

The Rigid Body Motion approach implies that the solid body is not deformed and the whole mesh, which is not deformed either, moves according to an imposed motion relative to the laboratory reference frame. Standard governing equations are solved for the moving mesh. This solution strategy, if adopted using correct meshing, enough inner iterations to converge at each time step and with a sufficiently small time step, is able to capture unsteady phenomena and their influences on the performance coefficients. However, these simulations are much more time consuming compared to steady state and therefore one of the objective of this study is to analyse the validity of steady state solution approaches comparing the computational cost of both possibilities. Another option that is not used in the present investigation is represented by the Sliding Mesh techniques that, combining regions assigned with Rigid Body Motion and static regions, are useful for non-axisymmetric domains. In these approaches the rotating region is assigned a rotational velocity and the mesh slides along the interface of the steady control volume.

4.2 Mesh selection

STAR CCM+ has an automated mesher which can perform both surface and volume meshing. These meshers are allowed to be customized to increase the number of cells in the most relevant regions and/or surfaces. There are different volume meshers that can be chosen. These are divided into two main groups: unstructured and structured meshers. There is also an option for special treatment near relevant surfaces, such as prism layer meshing to appropriately resolve the boundary layer.

4.2.1 Structured and unstructured meshing

Both meshing strategies are acceptable for external aerodynamics; however, there are several differences between the two kinds of meshes that may drive the meshing strategy selection. An unstructured grid allows varying the resolution over the same region in a more efficient way than a structured grid and reduces the number of elements. It also allows meshing complex geometries without increasing considerably the resolution and enables an easier grid refinement to perform mesh independence studies. On the other hand, structured meshing can be done massively parallel which makes it faster and they also require less memory. Unstructured grids have random face orientations which reduces numerical dissipation and structured grids can be aligned with the flow direction and which can also reduce numerical dissipation. STAR CCM+ has a polyhedral mesher which generates an unstructured grid and a trimmed cells mesher which generates a structured grid.

4.2.2 Prism layer mesher

In order to solve appropriately the boundary layer of the blade, it is necessary to include a prism layer in the near wall region. STAR CCM+ allows two kinds of wall treatments, one considering the whole boundary layer, the so-called ‘All- y^+ treatment’ and another one, the ‘High y^+ treatment’, which models with wall functions up to the buffer layer and attempts to solve the logarithmic layer. In the ‘All y^+ treatment’ the normalized height of the first cell should be about $y^+=1$. It has been shown that further decreasing the normalised height does not produce any improvement in the results and so it only implies an increase in the number of cells. In the ‘High y^+ treatment’ the first cell height should be placed at around $y^+=30$. In order to estimate the first cell height we can use Prandtl’s simplified flat plate theory if the flow is turbulent and Blasius’ solution for the flat plate for laminar boundary layer. Starting with the turbulent boundary layer, following Prandtl’s suggestion a velocity profile can be defined such as:

$$\frac{U}{U_e} = \left(\frac{y}{\delta}\right)^{\frac{1}{7}}, \text{ for } y < \delta \quad (4.8)$$

And a friction coefficient such as:

$$C_f \approx \frac{1}{50} Re_\delta^{-\frac{1}{6}} \quad (4.9)$$

Considering Karman integral equation for incompressible flow and no pressure gradient:

$$\frac{d\theta}{dx} = \frac{1}{2} C_f \quad (4.10)$$

Being θ , the momentum thickness:

$$\theta = \int_0^{\infty} \frac{U}{U_e} \left(1 - \frac{U}{U_e}\right) dy = \delta \int_0^1 \eta^{\frac{1}{7}} \left(1 - \eta^{\frac{1}{7}}\right) d\eta = \frac{7\delta}{72} \quad (4.11)$$

Transforming Karman's equation into:

$$\frac{7}{72} \frac{dRe_{\delta}}{dRe_x} = \frac{1}{100} (Re_{\delta})^{-\frac{1}{6}} \quad (4.12)$$

Which can be integrated as:

$$Re_{\delta} = \left(\frac{6}{50} Re_x\right)^{\frac{6}{7}} \quad (4.13)$$

Introducing equation 6.13 in 6.9 the friction coefficient can be expressed as:

$$C_f \approx 0.027 Re_x^{-\frac{1}{7}} \quad (4.14)$$

The wall friction can be computed as:

$$\tau_w = \frac{1}{2} \rho U_{\infty}^2 C_f \quad (4.15)$$

And the friction velocity as:

$$U^* = \sqrt{\frac{\tau_w}{\rho}} \quad (4.16)$$

And so height of the first cell to accomplish $y^+=1$ and $y^+=30$ should be:

$$\Delta s_{All y^+} = \frac{\mu}{U^* \rho}, \quad \Delta s_{High y^+} = \frac{30\mu}{U^* \rho} \quad (4.17)$$

The Reynolds number is replaced by the Reynolds number over the blade:

$$Re_x \approx \frac{\rho(\Omega 0.75R) C_{0.75R}}{\mu} = 21662 \quad (4.18)$$

And taking the reference values at 75% of the chord the wall thickness results in the values can be computed.

The other input parameter for the prism layer would be the prism layer total thickness. This value should be equal to the maximum thickness of the boundary layer along the blade surface in order for the boundary layer to be always contained inside the prism layer. The flat plate theory can be again used, from equation 6.13:

$$\delta = \frac{\mu}{\rho U_\infty} Re_\delta = \frac{\mu}{\rho U_\infty} \left(\frac{6}{50} Re_x \right)^{\frac{6}{7}} = \frac{\left(\frac{\mu}{\rho} \right)^{\frac{1}{7}} \left(\frac{6}{50} \right)^{\frac{6}{7}} x^{\frac{6}{7}}}{U_\infty^{\frac{1}{7}}} \quad (4.19)$$

This value would be an upper limit as in this calculation the whole boundary layer is considered turbulent which is not exactly true. However the result would be over dimensioning the boundary layer which is not a problem as the whole boundary layer could be captured. To correctly dimension the prism layer for the whole blade the section with the thicker boundary layer should be selected. Figure 4.3 shows the radial distribution of the maximum boundary layer thickness of a full scale propeller with a turbulent boundary layer. From this plot the maximum value can be found.

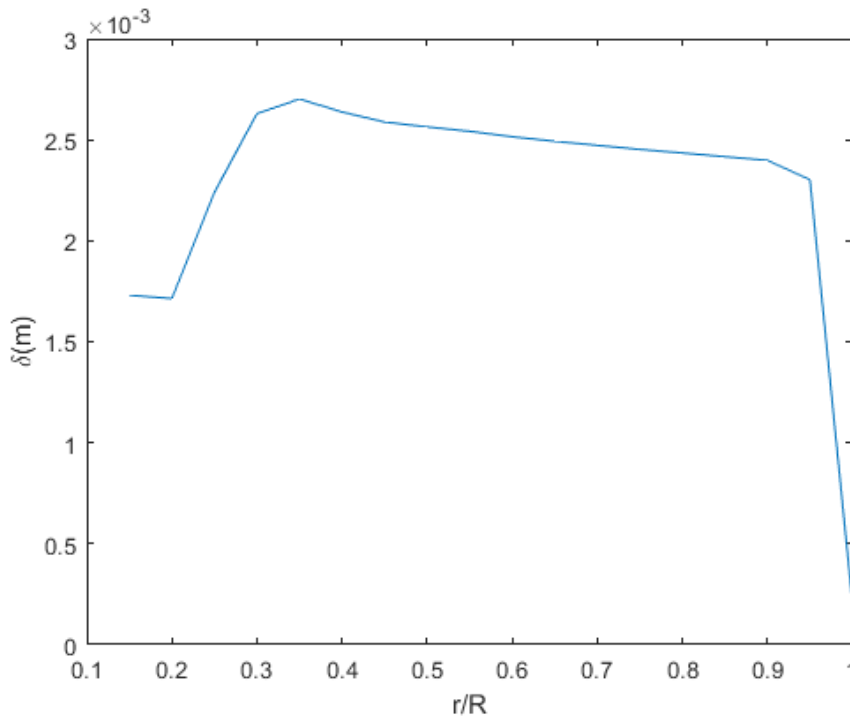


Figure 4.3: Boundary layer thickness estimation for a full scale propeller with a turbulent boundary layer.

For laminar boundary layers the estimation of both magnitudes defining the prism layers is different. Blasius solution can be used. Using the standard definition of prism layer thickness:

$$u(\delta) = 0.99U_\infty \quad (4.20)$$

Blasius self-similar solution defines velocity as:

$$u = U \frac{df}{d\eta}, \text{ where } \eta = y \sqrt{\frac{U}{2\nu x}} \quad (4.21)$$

The function $f(\eta)$ is the solution to the transformed boundary layer differential equation:

$$\frac{d^3 f}{d\eta^3} + f \frac{d^2 f}{d\eta^2} = 0, \quad f(0) = \left(\frac{df}{d\eta}\right)_{\eta=0} = 0 \quad \text{and} \quad \left(\frac{df}{d\eta}\right)_{\eta \rightarrow \infty} = 1 \quad (4.22)$$

This equation can be solved numerically finding the function $f(\eta)$. To calculate $\delta(x)$ is necessary to find the value of η for which $\left(\frac{df}{d\eta}\right)_{\eta} = 0.99$, this is found out to be $\eta \approx 3.5$.

From the definition of the variable η the boundary layer thickness can be calculated as:

$$\delta(x) \approx \frac{4.9x}{\sqrt{Re_x}} \quad (4.23)$$

The same as in the turbulent case the maximum value should be selected in order to capture all the boundary layer. Figure 4.4 shows the radial distribution of the maximum boundary layer thickness of a small scale propeller with a laminar boundary layer.

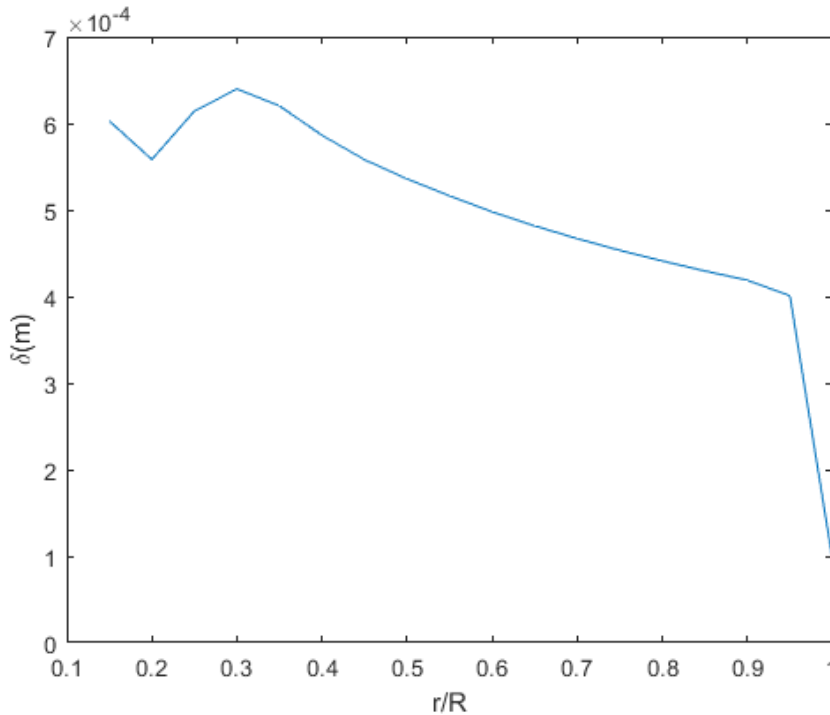


Figure 4.4: Boundary layer thickness estimation for a small scale propeller with a turbulent boundary layer.

4.3 Turbulence modelling

Even though the boundary layer can be laminar, the Reynolds numbers involved in our problem could produce a turbulent wake. This means that turbulent scales have to be either solved or modelled to obtain accurate results. STAR CCM+ provides 3 approaches; Reynolds Averaged Navier-Stokes Equations (RANS) and Unsteady Reynolds Averaged Navier-Stokes Equations (URANS), Detached Eddy Simulation (DES) and Large Eddy Simulation (LES).

4.3.1 Reynolds Averaged Navier-Stokes Equations (RANS)

This approach gets the Navier-Stokes original equations, performs a temporal average and attempts to solve the flow in terms of mean variables, which can be expressed as:

$$\Phi(\vec{x}, t) = \langle \phi \rangle(\vec{x}, t) = \frac{1}{2T_0} \int_{t-T_0}^{t+T_0} \phi(\vec{x}, t') dt' \quad (4.24)$$

If these mean or averaged values depend on time turbulence is considered statistically unsteady and if they do not depend on time, statistically steady. For statistically unsteady turbulence ensemble averages have to be taken into account and the definition above would not be completely rigorous. We can define a fluctuation of the variables as:

$$\phi'(\vec{x}, t) = \phi(\vec{x}, t) - \Phi(\vec{x}, t) \quad (4.25)$$

The mean value of the fluctuation can be expressed as

$$\langle \phi' \rangle = \langle \phi \rangle(\vec{x}, t) = \frac{1}{2T_0} \int_{t-T_0}^{t+T_0} \Phi(\vec{x}, t') dt' - \frac{1}{2T_0} \int_{t-T_0}^{t+T_0} \phi(\vec{x}, t') dt' \cong 0 \quad (4.26)$$

As mean value can go out of the integral directly in statistically steady turbulence and even in statistically unsteady turbulence considering a sufficiently small T_0 , $\phi(\vec{x}, t') \cong \phi(\vec{x}, t)$. Defining the variables present in Navier-Stokes equations as:

$$\vec{u} = \vec{U} + \vec{u}', \quad p = P + p', \quad T = \Theta + T' \quad (4.27)$$

Then this equations are averaged cancelling any term which in average will be zero, the resultant system is:

$$\nabla \cdot \vec{U} = 0 \quad (4.28)$$

$$\rho \frac{\partial \vec{U}}{\partial t} + \rho \nabla \cdot (\vec{U} \vec{U}) = -\nabla P + \nabla \cdot (\tau'_U - \rho \langle \vec{u}' \vec{u}' \rangle) \quad (4.29)$$

$$\rho c_p \frac{\partial \Theta}{\partial t} + \rho c_p \vec{U} \nabla \Theta = \nabla \cdot (k \nabla \vec{U} - \rho c_p \langle T' \vec{u}' \rangle) \quad (4.30)$$

Where:

$$\tau'_U = \mu \left[\nabla \vec{U} + (\nabla \vec{U})^T \right] \quad (4.31)$$

Equations 4.28-4.30 represent the Reynolds equations for a gas at low Mach numbers without volume forces and neglecting thermal viscous dissipation. For statistically steady turbulence time dependant terms will be neglected. The term $-\rho \langle \vec{u}' \vec{u}' \rangle$ is called the Reynolds Stress Tensor or Turbulent Stress Tensor as looking into the equations it has a similar role to the viscous stress tensor. This term is unknown and has to be modelled. There are two main kind of turbulence models; Eddy viscosity models and Reynolds-Stress Models. The first kind attempts to predict turbulent viscosity and the second kind uses transport equations for the Reynolds stresses also modelling some terms in these transport equations. This last method is suitable for complex 3D turbulent flows but increases significantly computational cost and complicates convergence. The eddy viscosity approach is the most popular and there are three main families of models; Spalart-Allmaras (1 equation), $k - \epsilon$ (2 equations) and $k - \omega$ (2 equations). Spalart-Allmaras is mainly designed for transonic/supersonic flows where separation is mild, however its applicability to other scenarios is subject of current studies. $k - \epsilon$ model, especially the realizable is possibly the most well-known model and the more robust, however they may have some problems when dealing with rapidly rotating flows. And finally the $k - \omega$ family of models which is widely used method for aerospace and turbo-machinery applications. Different models will be applied in the following chapters to see the effect on propeller performance of selecting a particular model. STAR CCM+ recommends for aerospace applications the use of $k - \omega$ SST.

4.3.2 Unsteady Reynolds Averaged Navier-Stokes Equations(URANS)

Actually Equations 4.28-4.30 are the Unsteady Reynolds Averaged Navier Stokes Equations. As commented in the previous section the definition of the mean variables is not completely rigorous for statistically unsteady turbulence, an ensemble averages have to be done:

$$\Phi(\vec{x}, t) = \langle \phi \rangle(\vec{x}, t) = \lim_{N \rightarrow \infty} \frac{1}{N} \sum_1^N \phi(\vec{x}, t) \quad (4.32)$$

Repeating the experiment sufficient times would allow obtaining a mean value that may depend on time. A simpler interpretation of this comes from the less rigorous but more practical definition given in equation 4.16 is that if the Time T_0 is sufficiently large compared to the period of the oscillations and relatively small compared to the main flow variations, this mean is able to vary in time, and filters only the turbulent frequency oscillations. This is possible due to the fact that turbulent time scale is much shorter than mean flow time scale. Obviously this kind of approach is justified only for unsteady flows.

4.3.3 Large Eddy Simulation(LES) and Detached Eddy Simulations(DES)

LES attempts to solve the real flow, not the averaged flow. It is not yet possible to perform DNS simulations of real industrial applications as the grids and computational costs would be

really large in order to simulate below Kolmogorov's scale. LES filters the turbulent eddy spectrum and solves only the scales above the grid resolution, the smaller scales are modelled with the commonly called subgrid models or subgrid stresses. LES is intrinsically unsteady. LES requires a very big cell count near the wall which normally makes it unviable for external aerodynamics applications which are correctly approximated by RANS. However LES is popular in applications where RANS is not successful such as; combustion, mixing or flow around bluff bodies. Detached Eddy Simulations(DES) is a middle way solution between RANS and LES, which tries to mitigate the prohibitive cell count near the wall that LES requires. These simulations basically apply RANS in the near wall regions and LES elsewhere; this makes the simulations not too expensive and is becoming popular in performance simulations.

5 Benchmark test: DA-4022 5x3.75 Inches

In order to validate and evaluate the capability of the different approaches embedded in STAR CCM+ to simulating propeller performances, the DA-4022 propeller, designed by the Department of Aerospace Engineering at the University of Illinois at Urbana-Champaign (UIUC) [1], has been chosen for simplicity and data availability. In fact, most commercial propellers manufactures are reluctant to disclose geometry specifications. DA-4022 was designed with a rectangular blade with $\frac{c}{R} = 0.23$ and a constant pitch of 3.75 inches. The aerofoil used along the whole blade is the SDA1075 (Figure 5.1), which has a relative thickness of around 12%. The coordinates can be found on appendix A.



Figure 5.1: SDA1075 aerofoil.

It is really difficult to have a CAD model that represents precisely a real geometry, especially for these small scale propellers with thicknesses around 1mm considering that leading edge and pitch resolution are so important. This prototype was CAD modelled and 3D printed at the UIUC [1] and then scanned with the open software PropellerScanner, developed by Martin Hepperly[18]. PropellerScanner results showed small deviations in the chord distributions, except on the tip where the image resolution fails to represent adequately the geometry, and slightly higher deviations on the pitch angle, however these were of a maximum of 2.5° which showed that the manufacturing process was relatively accurate. Figures 5.2 and 5.3 show the variation of the pitch and chord distributions of the manufactured model respect to the designed values.

5.1 CAD Modelling

Considering the relatively small errors between scanned and designed blades, a CAD model was created with scanned data. A systematic procedure, described in the following lines, was created to enable the generation of Blade geometries in a CAD modeller from the aerofoil coordinates, chord and pitch distributions.

A MATLAB routine (Appendix B) was created to prepare data to be imported into the CAD modeller. This routine centres the profile on the reference axis, in our case 50% of the chord (as the propeller projections are symmetric), and then it moves the profile along the Z-axis (that is radially) to its corresponding radial position, it scales the airfoil to its corresponding chord and finally it rotates the profile via the rotation matrix:

$$R = \begin{pmatrix} \cos(\alpha) & -\sin(\alpha) \\ \sin(\alpha) & \cos(\alpha) \end{pmatrix} \quad (5.1)$$

With α :

$$\alpha = -90 + \beta \quad (5.2)$$

Where β is the pitch angle.

This is done for all the radial positions in which the geometric data is provided. Once all the profiles are generated they are imported on to CAD. All the points forming each profile are splined and these splines are then lofted to obtain a final closed surface which can be converted into a volume easily. To obtain the opposite blade a simple 180° rotation about the rotational axis is required. For simplicity and due to the lack of detail about the original hub, a cylindrical hub was generated to link the two blades. Figures 5.4 and 5.5 show the final geometry.

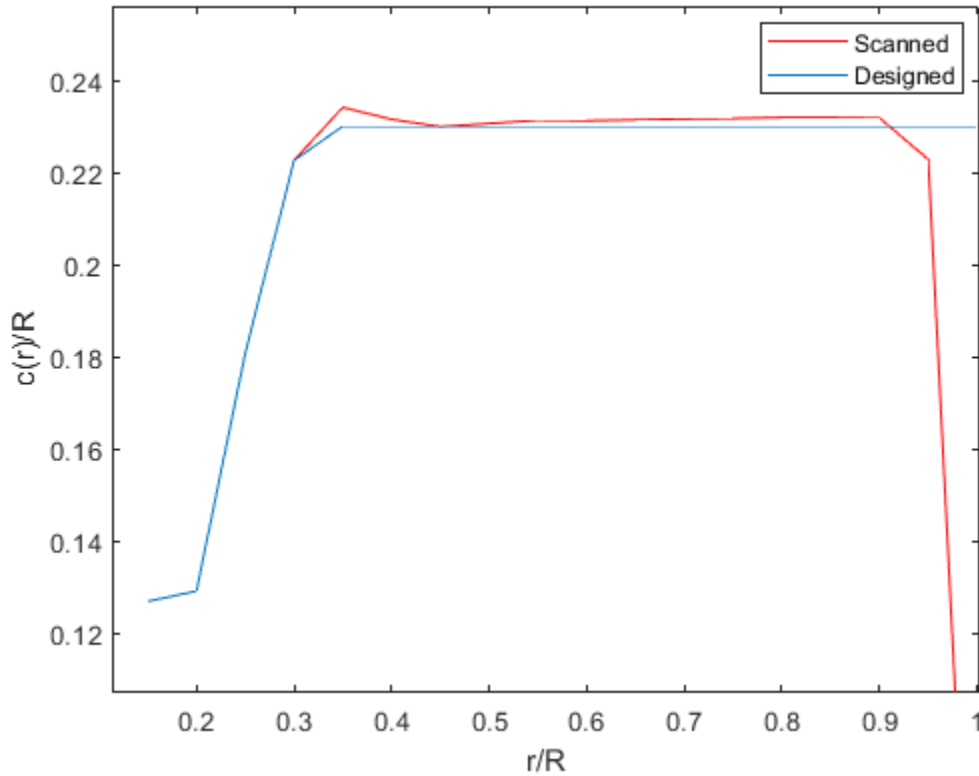


Figure 5.2: Chord distribution of the manufactured and designed models.

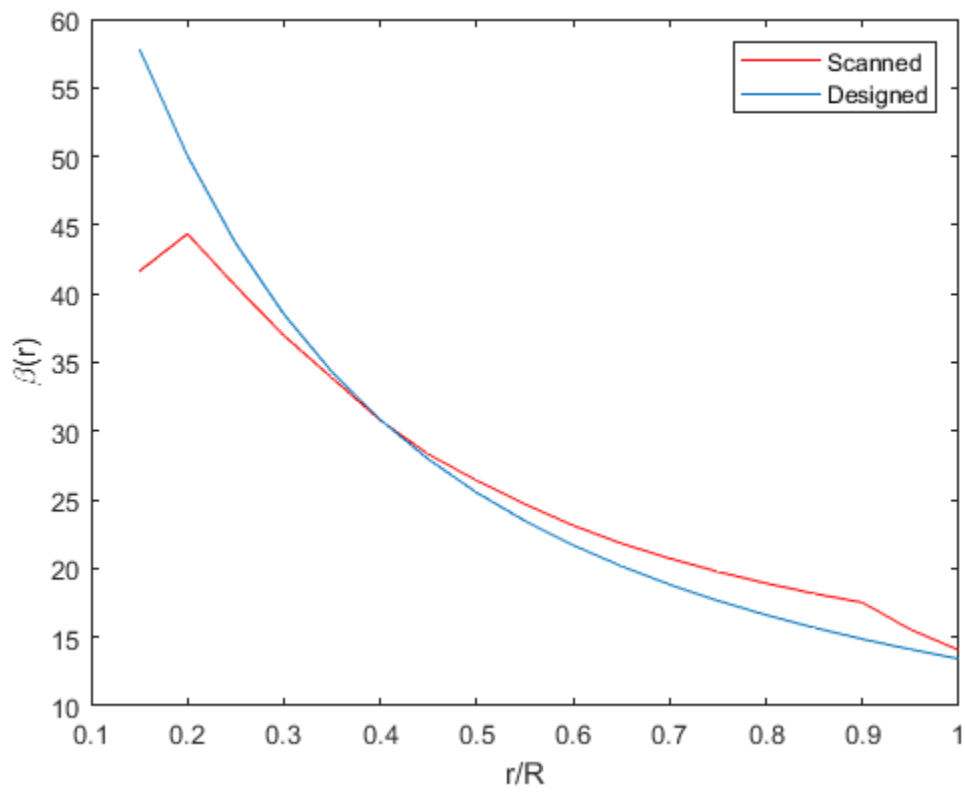


Figure 5.3: Pitch angle distribution of the manufactured and designed models.

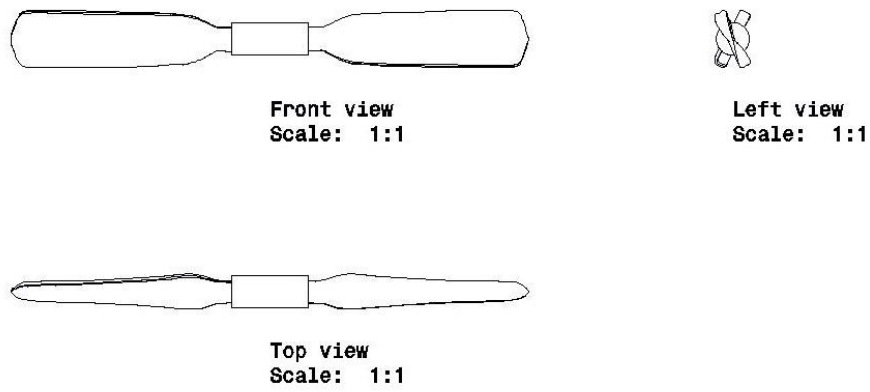


Figure 5.4: Top, front and side views of the CAD modelled geometry.



Figure 5.5: Rendered Image of CAD modelled Geometry.

5.2 Experimental performance

UIUC has conducted wind-tunnel tests for this propeller [1]. These data are going to be used to validate the CFD simulations in the following chapters. In particular, the advance ratio study will be reproduced to check if results are coherent at different operating conditions. Chapter 3 showed how the performance of a propeller depends essentially on three non-dimensional parameters:

$$C_T, C_P, \eta = f(Re, M, J) \quad (5.3)$$

Due to the dimensions of the propeller and rotation rates, the Mach number is going to be low enough to consider negligible compressibility effects, as shown on section 6.1.4. Therefore, propeller performance would be only dependent on the advance ratio and the Reynolds number. Considering a constant rotation rate, with our definition of Reynolds number, this will remain constant and so the dependence study on J can be done. If a different rotation rate is considered, this would mean a different Reynolds number and so the performance curves would vary. Varying the advance ratio with a constant rotation rate essentially means increasing the inflow velocity, this is done experimentally by increasing the speed in the wind tunnel. Figures 5.6, 5.7 and 5.8 show the experimental results obtained in reference [1], for the advance ratio study associated to a rotation rate of 4546 RPM, which has been chosen to check the validity of the CFD simulations.

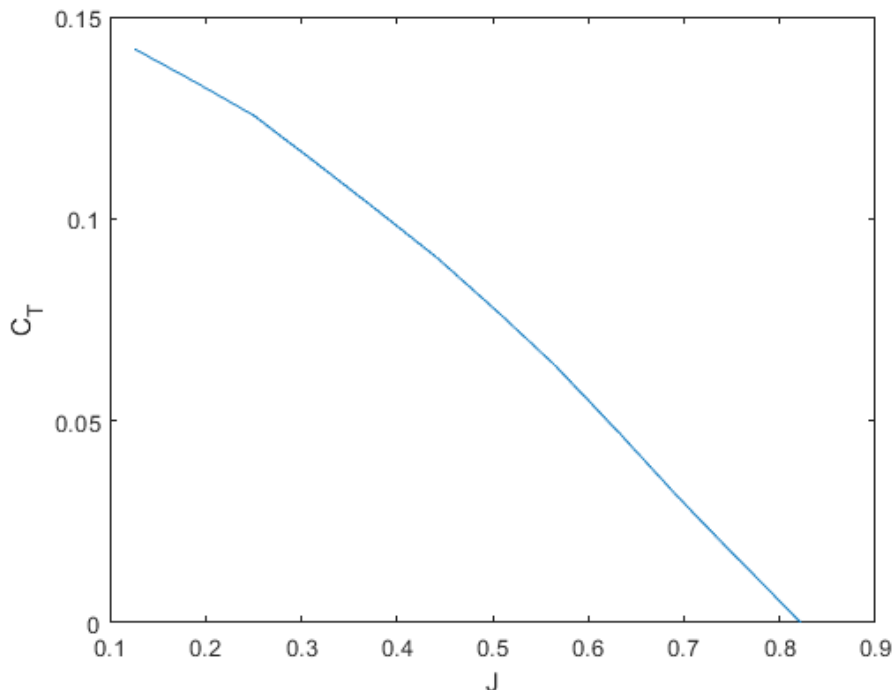


Figure 5.6: Thrust coefficient for rotation rate 4546 RPM.

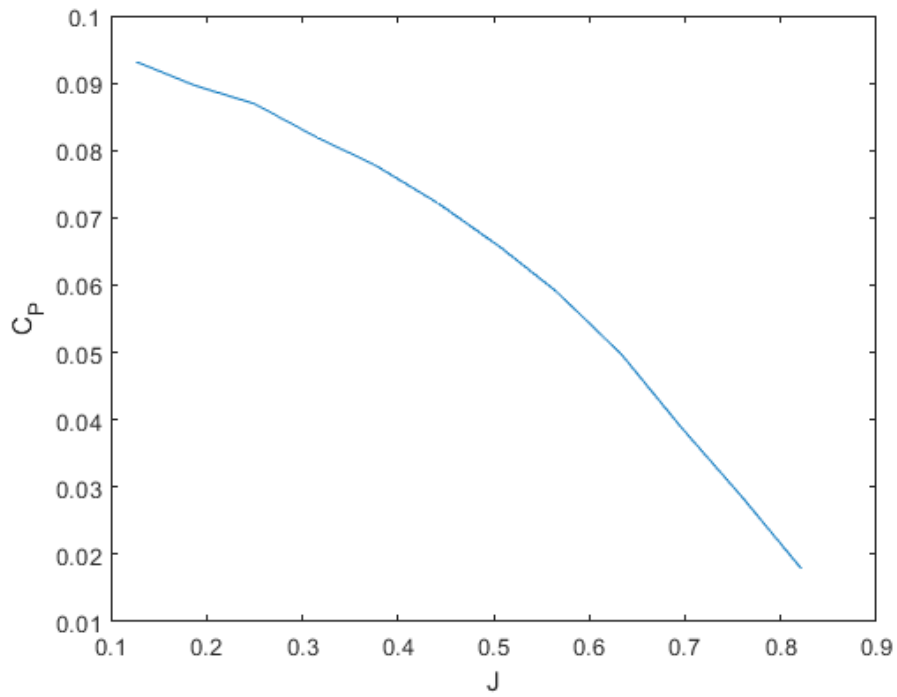


Figure 5.7: Power coefficient for rotation rate 4546 RPM.

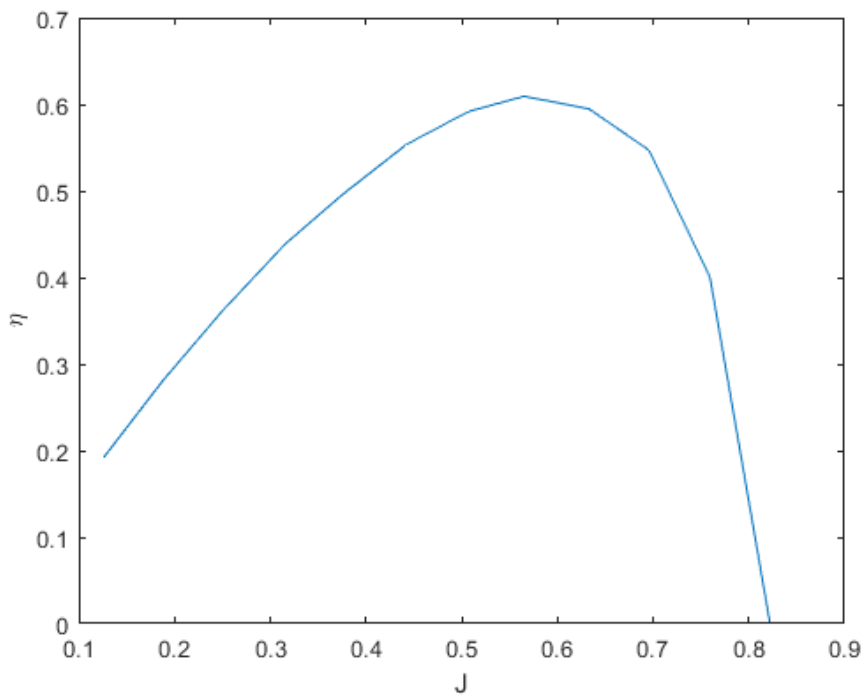


Figure 5.8: Efficiency for rotation rate 4546 RPM.

Table 5.1: Experimental Results for rotation rate 4546RPM from[1].

J	C_T	C_P	η
0.1266	0.1419	0.0932	0.1928
0.1884	0.1339	0.0896	0.2816
0.2502	0.1256	0.0869	0.3615
0.3159	0.1138	0.0819	0.4388
0.3753	0.1028	0.0779	0.4955
0.4424	0.0902	0.0721	0.5537
0.5070	0.0766	0.0656	0.5916
0.5652	0.0637	0.0591	0.6093
0.6331	0.0468	0.0498	0.5947
0.6958	0.0306	0.0389	0.5469
0.7595	0.0150	0.0285	0.4002
0.8220	0.0000	0.0178	0.0012

6 CFD simulations: Validation studies

6.1 Problem definition

As commented in chapter 5, steady state approaches are a potentially interesting way of solving certain rotating flows due to the considerably lower computational cost compared to unsteady simulations. In order to check the validity of this model, experimental data are used to check how appropriate the mesh, the rotating fluid region and the turbulent model selections are.

6.1.1 Fluid domain

The fluid domain is going to be subdivided into two regions; the exterior region, which will be solved in a steady reference frame and the inner region which encloses the propeller and will be solved on a rotating reference frame moving with the propeller. Figures 6.1 and 6.2 provide a sketch of the situation.

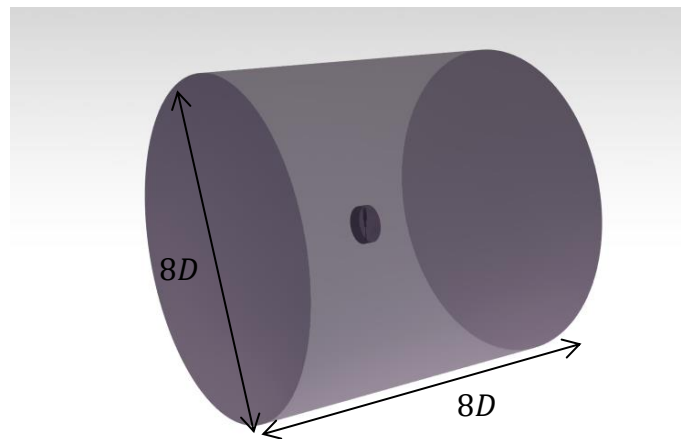


Figure 6.1: Fluid domain geometry.

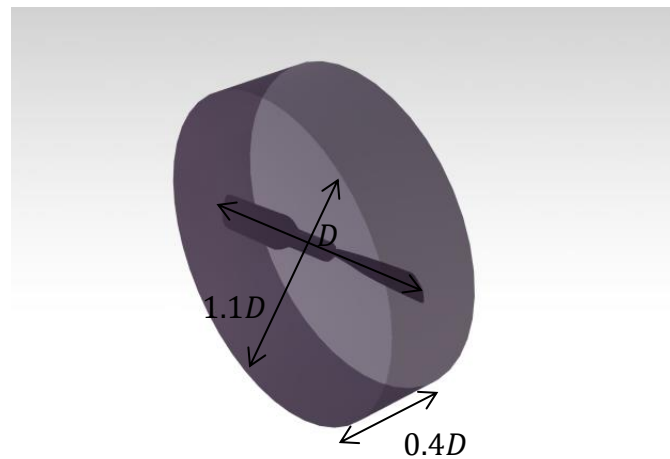


Figure 6.2: Rotating domain detailed geometry.

These dimensions or similar ones were used by various authors, for example [17]. The correct selection of this rotating region is important to obtain physically relevant solutions. These dimensions are going to be used to validate an appropriate mesh and afterwards a sensitivity analysis on the dimensions of this rotating region will be done.

6.1.2 Mesh generation

The following sections show the controls which have been defined relative to a base size, which is going to be our parameter for the mesh refinement study and will be defined in section 6.2.

6.1.2.1 Surface meshing

Table 6.1 shows the settings variation from default STAR CCM+ settings used for our surface mesher:

Table 6.1: Surface mesher controls.

Minimum face quality	0.2
Surface curvature	45 pts/circle
Surface Growth Rate	1.10

Then in order to perform local refinement on the blade surface the custom controls showed in table 6.2 were assigned to the blade surface.

Table 6.2: Propeller surface custom controls.

Curvature	76pts/circle
Edge proximity	3
Target size	10%(relative to the base)
Minimum target size	0.3% (Relative to the base)
Growth rate	1.05

These settings concentrate more faces on the leading edge where the curvature is higher and also allows resolving a finite trailing edge. The inner and outer faces of the rotating control volume have custom settings showed on table 6.3.

Table 6.3: Rotating region surface custom controls.

Target size	20%(relative to the base)
Minimum target size	4% (Relative to the base)
Wake refinement	Length: 1m, Size: 20% (Relative to the base)

These settings will generate a finer mesh downstream the rotating region, which is important to prevent mesh induced dissipation of the wake. Finally custom controls imposed on the outer surface are shown in table 6.4.

Table 6.4: Outer region surface custom controls.

Target size	400%(relative to the base)
Minimum target size	150% (Relative to the base)

These settings will increase the size of the cells in the outer region where the flow is almost axial and its small variations do not affect greatly the flow field over the propeller blades. This reduces considerably the amount of cells in our simulation and so the computational cost is reduced.

6.1.2.2 Volume mesh

The polyhedral mesher (Unstructured) was chosen over the trimmed cell mesher(Structured) to try to reduce the number of cells needed to represent correctly the complex propeller geometry. Table 6.5 shows the controls on the polyhedral mesher.

Table 6.5: Polyhedral mesher settings.

Growth Rate	On
Volume Growth Rate	1.2
Maximum Cell Size	1000% (Relative to the base)
Optimization Cycles	4

Activating the growth rate reduces the cell number between different surfaces and the optimizer increases mesh quality.

6.1.2.3 Prism layer mesher

As seen in chapter 4 the prism layer has to attempt to capture all the boundary layer. For this aerofoil, which relative thickness is 12%, it is expected that in the vicinity of the leading edge, when the aerofoil has a certain angle of attack, a recirculation bubble forms, however this is normally small, around 1% of the chord, and so it will not affect greatly the boundary layer configuration. As the angle of attack increases this bubble moves towards the leading edge into areas of higher curvature making reattachment more difficult. At a certain angle of attack the bubble bursts extending stall to all the top surface of the aerofoil. Nevertheless as the recirculation bubble is relatively small the prism layer estimations done in chapter 4 should remain valid. The chord at 75% blade span is 1.46 cm.

$$Re_x \approx \frac{\rho(0.75 R \Omega) c_{0.75R}}{\mu} = 21662 \quad (6.1)$$

A usual estimation of the Reynolds number that triggers transition to turbulent flow for a flat plate is $Re_x = 5 \cdot 10^5$, this value is clearly under and so, transition should not occur and the boundary layer should remain laminar along the chord. From equation 4.15 and figure 4.3, which actually refers to our propeller, a value of at least $\delta = 0.65mm$ should be used. However, taking into account that this estimate where done for a flat plat with no angle of

attack and that adverse pressure gradients tend to thicken the boundary layer, a value of $\delta = 0.9mm$ was finally selected for our prism layer.

Even though theory suggests that the boundary layer should remain laminar, the simulations have been carried out using turbulence models to model the wake's turbulence. These models require $y^+=1$ and therefore the height of the first cell at the wall has been calculated as:

$$\Delta s = \frac{0.0982x}{\sqrt{Re_x}} = 0.018mm \quad (6.2)$$

The prism layer settings are shown in table 6.6 and prism layer controls applied to the propeller are in table 6.7.

Table 6.6: Prism Layer Settings.

Stretching function	Hyperbolic Tangent
Stretching Mode	Wall Thickness
Minimum Thickness Percentage	0.01
Layer percentage Reduction	0.0

This settings attempt to perform a conformal mesh, the number of layer is constant.

Table 6.7: Prism Layer Controls Propeller surface.

Number of Layers	24
Wall Thickness	$1.8 \cdot 10^{-5}m$
Total Thickness	$9.0 \cdot 10^{-4}m$

Figure 6.3 shows the prism layer mesh generated.

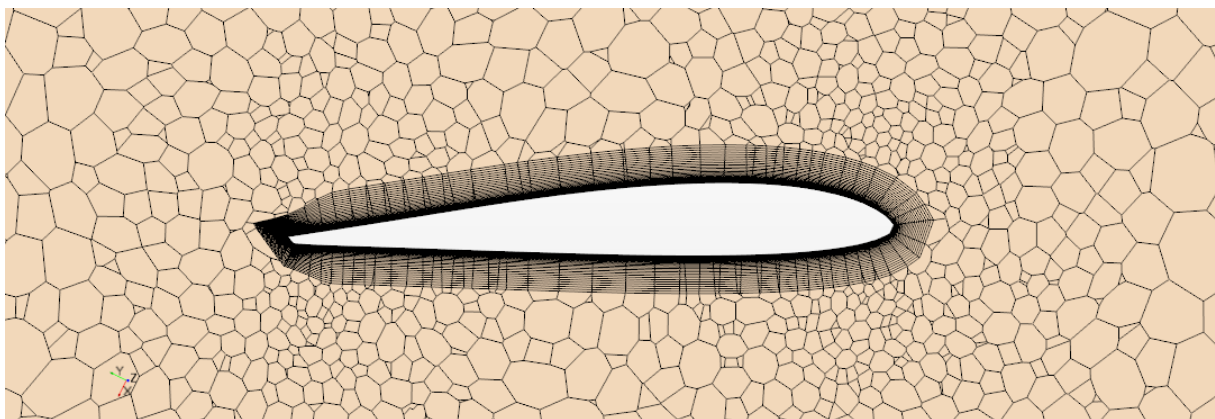


Figure 6.3: Prism layer mesh at the plane $z=-0.02$.

6.1.3 Interfaces and Boundary conditions

In order to reduce the number of cells, and so the computational cost, only half of the domain is being solved, considering the plane $z=0$ as a periodic boundary matching the $y < 0$ semi-plane with the $y > 0$ semi-plane. Figure 6.4 shows a sketch of the situation.

The inlet boundary is specified as a velocity inlet with the value of the freestream velocity which depends on the advance ratio, table 6.8 shows the freestream velocity for each advance ratio at the rotation rate used, 4546 RPM.

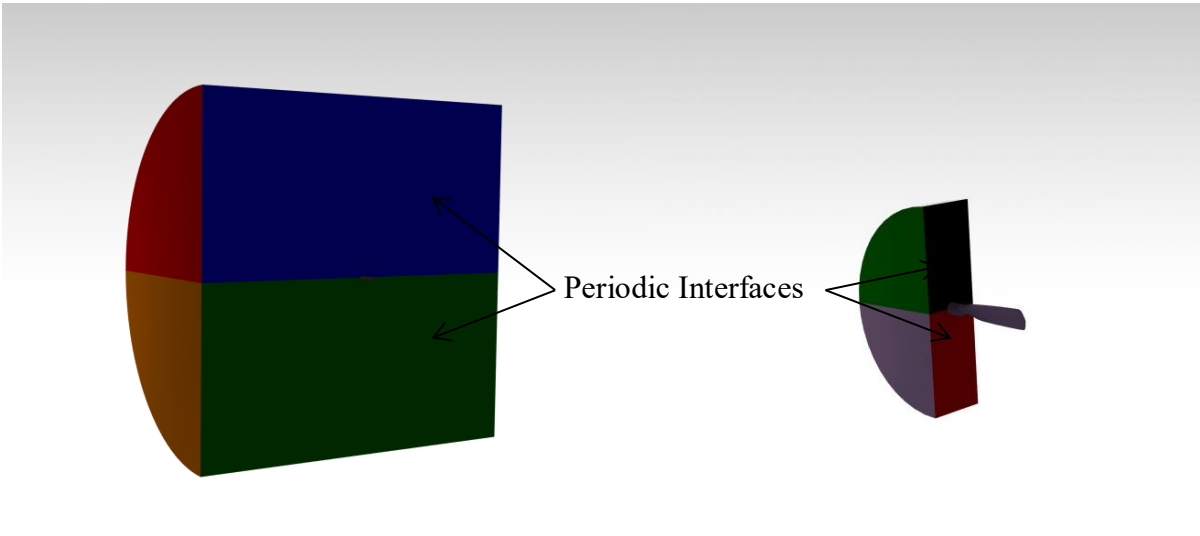


Figure 6.4: Periodic interfaces sketch.

Table 6.8: Example of freestream velocities for rotation rate 4546 RPM.

J	$V(m/s)$
0.1884	1.809
0.3753	3.608
0.5070	4.879
0.5652	5.467
0.6331	6.091
0.7595	7.303

The outlet boundary is specified as a pressure outlet and in the lateral surface a non-slip condition was assigned to mimic the walls on a wind tunnel, however it was also tested (Section 6.5) with freestream conditions and there was no difference in the resultant coefficients as these walls are sufficiently far away from the rotating body.

The rotating region is assigned to a rotating reference frame rotating at 4546 RPM. Therefore, at the common interfaces a reference frame transformation takes place to adapt the rotating and stationary frames of reference. STAR CCM+ provides two suitable interfaces for this application; internal interfaces and mixing plane interfaces. In section 6.5 both models will be applied to check the differences in the global coefficients and convergence to the final solution. For the validation test internal interfaces will be used.

6.1.4 Physics models

Due to the geometry, the simulation had to be 3D, RANS equations were used, different turbulence models were tested but for validation purposes the model $k - \omega SST$ was used.

The ‘ALL y^+ treatment’ option was selected. The simulation was done for air at 300K and pressure 101325 Pa. Ideal gas model was used. In order to choose the segregated solver or the coupled solver the Mach number on the tip of the blade can be computed. An estimate of the velocity can be found using momentum theory (Equation 2.15) and experimental thrust.

$$w = (1 + a)U_\infty = \frac{U_\infty}{2} \left(1 \pm \sqrt{1 + 8 \frac{C_T}{\pi J^2}} \right) \quad (6.3)$$

This function is shown in figure 6.5, where we can see that is a crescent function and so the maximum value will be associated with the maximum advance ratio in our simulation which was 0.759 (Table 6.8) which has a velocity value of 7.5 at the rotor, therefore the Mach number on the tip may be calculated as:

$$M_{tip} = \frac{\sqrt{(\Omega R)^2 + w^2}}{a} = 0.0897 \quad (6.4)$$

In order to justify the segregated solver the pressure has to be a weak function of temperature and density, this can be shown by estimating density and temperature variations orders of magnitude from the enthalpy equation:

$$\rho c_p \frac{\partial T}{\partial t} + \rho c_p \vec{v} \cdot \nabla T = \frac{\partial p}{\partial t} + \vec{v} \cdot \nabla p + \nabla \cdot (\kappa \nabla T) + \bar{\tau}' : \nabla \vec{v} \quad (6.5)$$

- Temperature variations due to pressure.

$$\frac{\Delta T_p}{T_0} \sim \frac{\Delta p}{\rho c_p T_0} \sim \frac{U^2}{c_p T_0} \sim M^2 \quad (6.6)$$

- Temperature variations due to heat conduction.

$$\frac{\Delta T_q}{T_0} \sim \frac{T_1 - T_2}{T_0 Pr Re} \quad (6.7)$$

- Temperature variations due to viscous dissipation.

$$\frac{\Delta T_{dis}}{T_0} \sim \frac{U^2}{C_p T_0 Re} \sim \frac{M^2}{Re} \quad (6.8)$$

It is clear that all terms are really small compared to unity and can therefore be neglected. Density variations can be estimated from the speed of sound definition:

$$a^2 = \left(\frac{\partial p}{\partial \rho} \right)_{ds=0} \quad (6.9)$$

$$\frac{\Delta \rho}{\rho} \sim \frac{\rho U^2}{\rho a^2} \sim M^2 \quad (6.10)$$

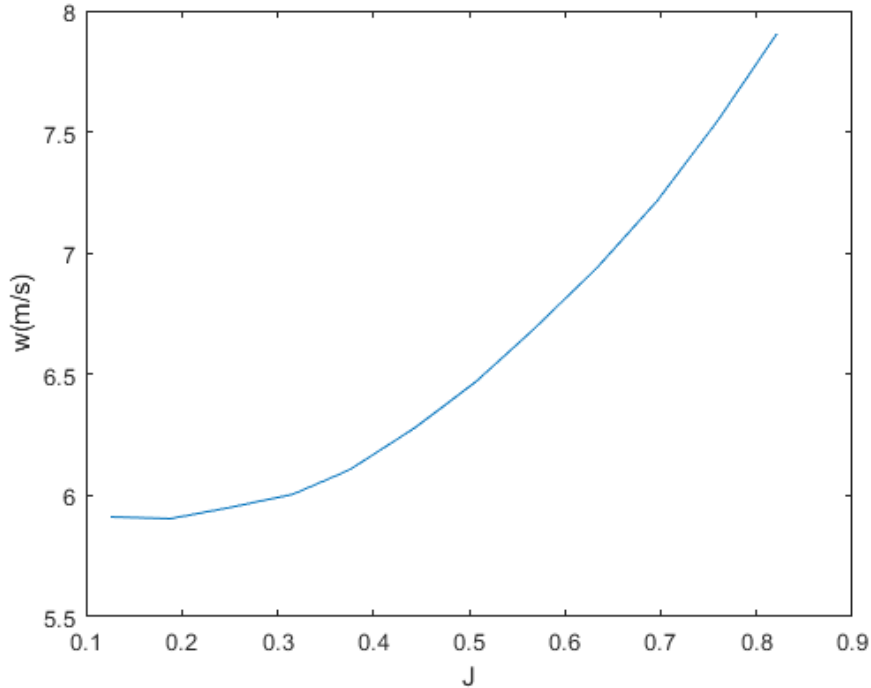


Figure 6.5: Induced velocity on the disc calculated from momentum theory.

As density and temperature variations prove to be of the order of the square of the Mach number and this is small, the choice of the segregated solver is justified. STAR CCM+ couples pressure and velocity with the Semi-Implicit Method for Pressure Linked Equations also known as SIMPLE.

6.2 Mesh refinement study

Three different meshes have been generated, named; course, standard and fine and they perform refinements in both surface and volume meshes. The prism layer parameters have been maintained constant thickness to maintain unaffected the resolution of the boundary layer. Table 6.9 shows the cell count for the different meshes.

Table 6.9: Trial Grids Characteristics.

	Base size(m)	Number of Cells
Coarse	0.075	419,422
Standard	0.050	664,791
Fine	0.025	1,643,324

Figures 6.6-6.8 show different snapshots of all three meshes where the cell count difference is appreciable.

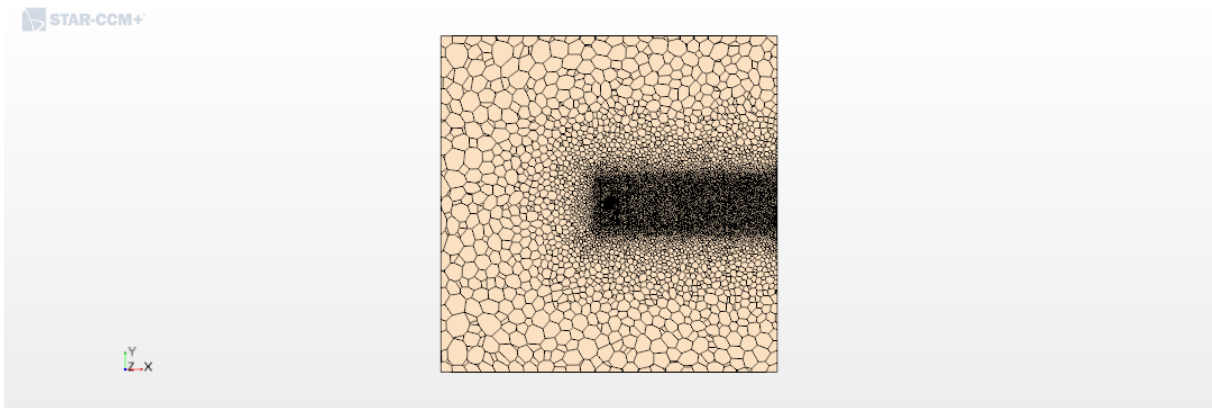


Figure 6.6: Fine mesh. Blade surface mesh (Top). Volume mesh at the plane $z=-0.02$ (Bottom).

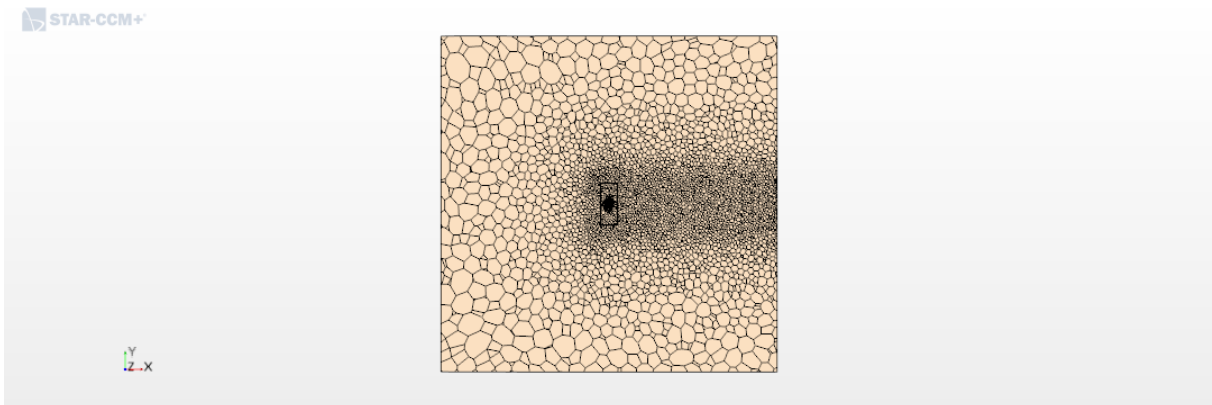
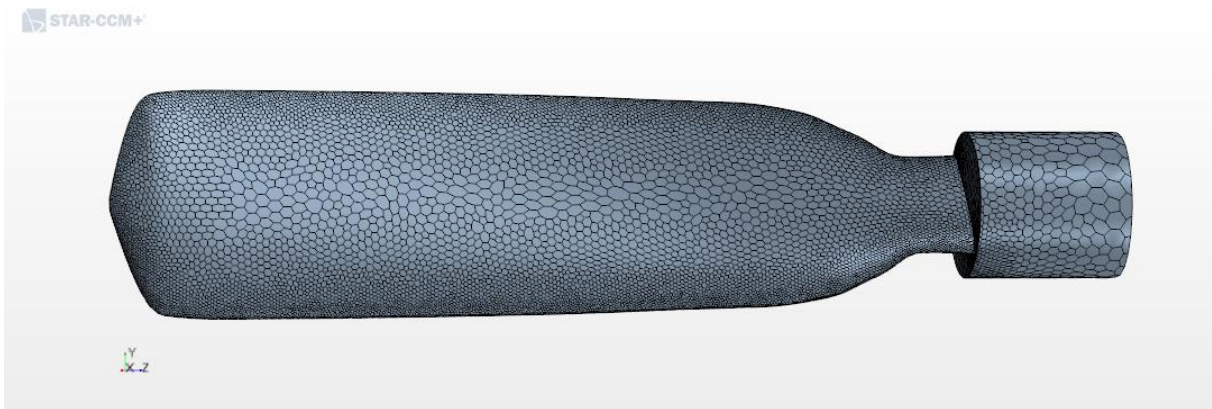


Figure 6.7: Standard mesh. Blade surface mesh (Top). Volume mesh at the plane $z=-0.02$ (Bottom).

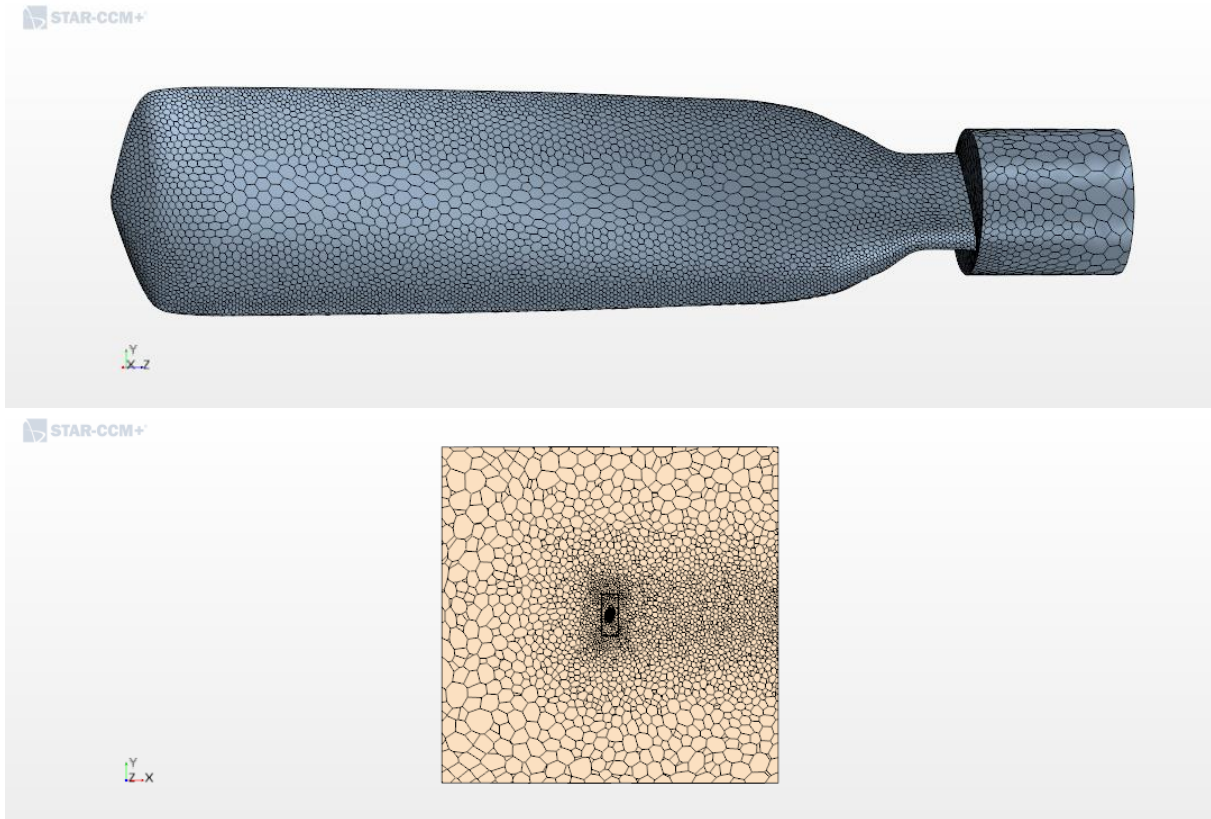


Figure 6.8: Course mesh. Blade surface mesh (Top). Volume mesh at the plane $z=-0.02$ (Bottom).

For all cases it is clear how there is a specific refinement towards the leading edge, important to capture correctly this high curvature area. Also the wake refinement is evident in order to capture adequately the flow in these area avoiding mesh induced effects as dispersion of the wake. Going from fine to coarse it is clear the significant reduction on the cell count.

In order to assess appropriately the validity of the different meshes, the following errors based on the definitions of the performance non-dimensional coefficients defined in chapter 3 are defined in equations 6.11-6.13.

$$\Delta C_T = \frac{C_{T_{CFD}} - C_{T_{EXP}}}{C_{T_{EXP}}} \times 100 \quad (6.11)$$

$$\Delta C_P = \frac{C_{P_{CFD}} - C_{P_{EXP}}}{C_{P_{EXP}}} \times 100 \quad (6.12)$$

$$\Delta \eta = \frac{\eta_{CFD} - \eta_{EXP}}{\eta_{EXP}} \times 100 \quad (6.13)$$

Two sets of simulations were done for all three meshes to check that the mesh was valid for two very different values of the advance ratio which has a really big influence on performance due mainly to the variation of effective angle of attack that each aerofoil sees. Table 6.10 shows the averaged values of the performance coefficients for the different meshes and

experimental results. Running this simulation as steady state means that the intrinsic unsteadiness of the problem is not being solved and even though the solver tries to converge, it does not succeed remaining a periodic oscillation in the solution. This is why the results have to be averaged. Figures 6.9-6.10 show the oscillations in Thrust and Power coefficients for the case of advance ratio 0.375 in the fine mesh.

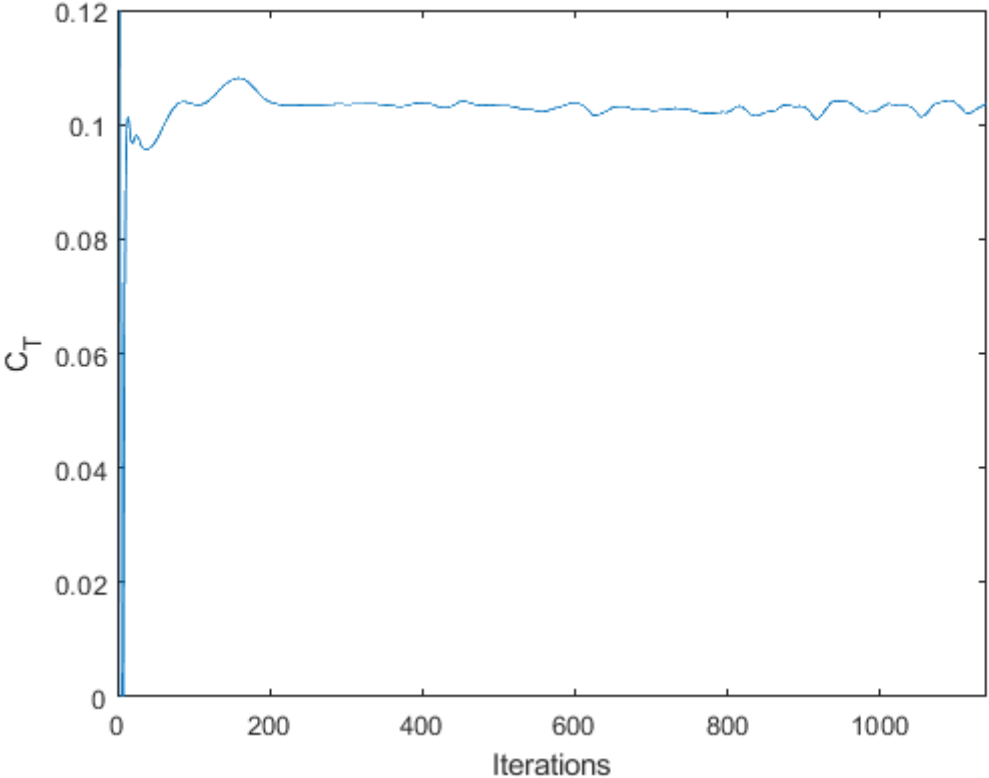


Figure 6.9: Thrust coefficient convergence on fine mesh J=0.375.

Table 6.10: Mesh refinement results.

Mesh	J=0.375			J=0.633		
	C_T	C_P	η	C_T	C_P	η
Fine(25mm)	0.1030	0.0807	0.4784	0.0486	0.0527	0.5830
Standard(50mm)	0.1017	0.0807	0.4723	0.0491	0.0538	0.5776
Coarse(75mm)	0.1012	0.0826	0.4597	0.0498	0.0548	0.5744

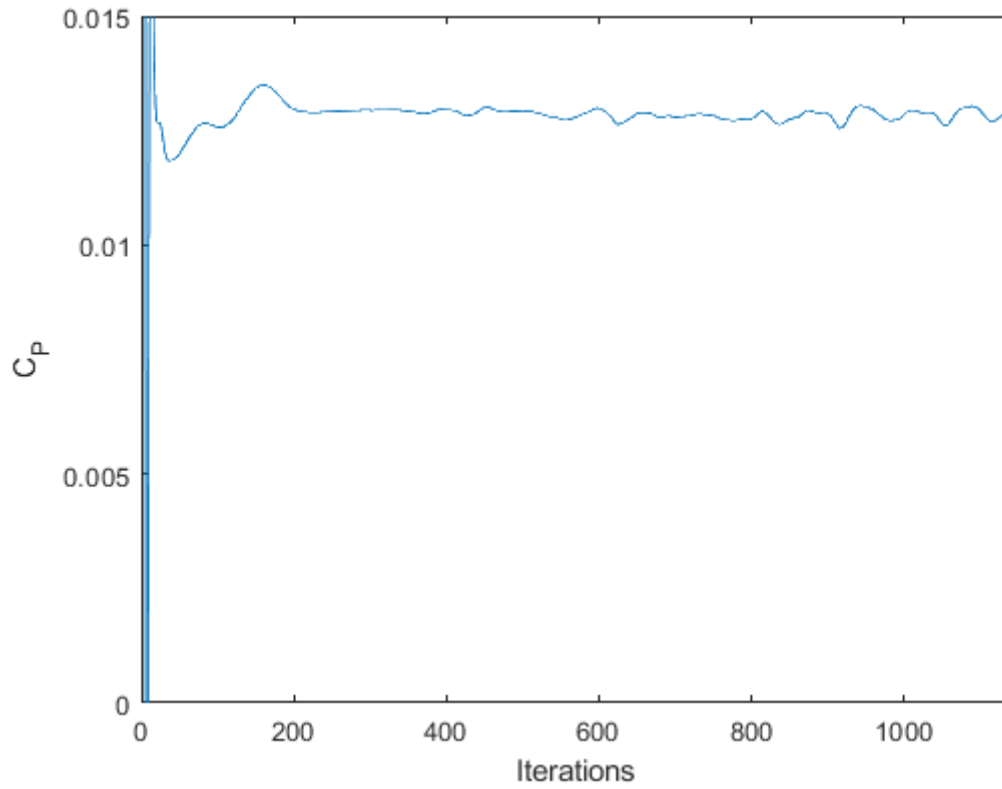


Figure 6.10: Power coefficient convergence on fine mesh for $J=0.375$.

Table 6.11: Relative Errors compared with experimental results.

Mesh	$J=0.375$			$J=0.633$		
	C_T	C_P	η	C_T	C_P	η
Fine(25mm)	0.1497	3.6670	-3.4588	3.8494	5.9168	-1.9663
Standard(50mm)	-1.1143	3.6750	-4.6846	5.0043	8.1005	-2.8785
Coarse(75mm)	-1.6005	6.0065	-7.2393	6.4157	10.1580	-3.4114

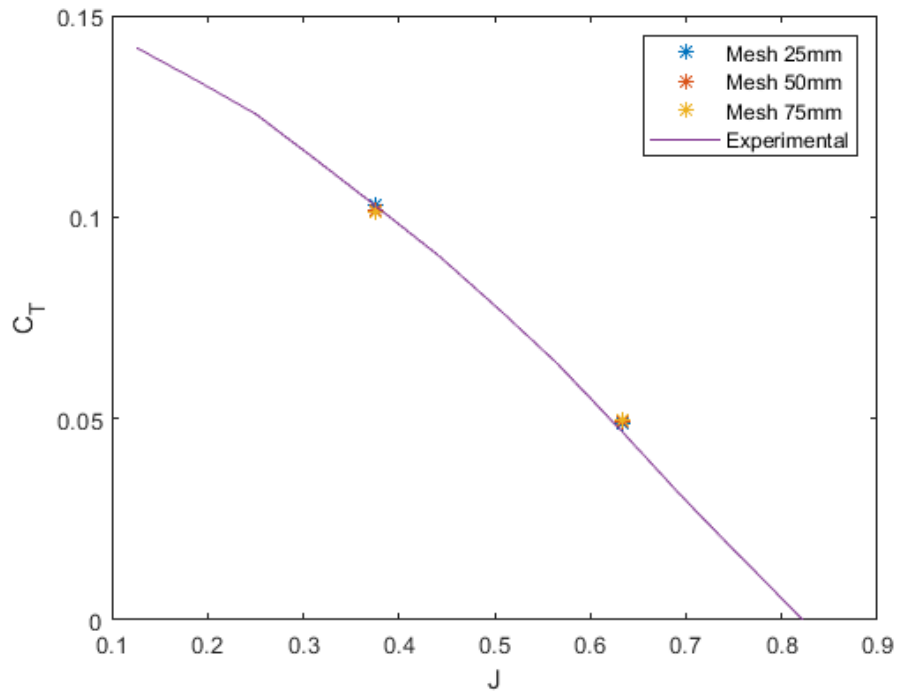


Figure 6.11: Thrust coefficient against advance ratio.

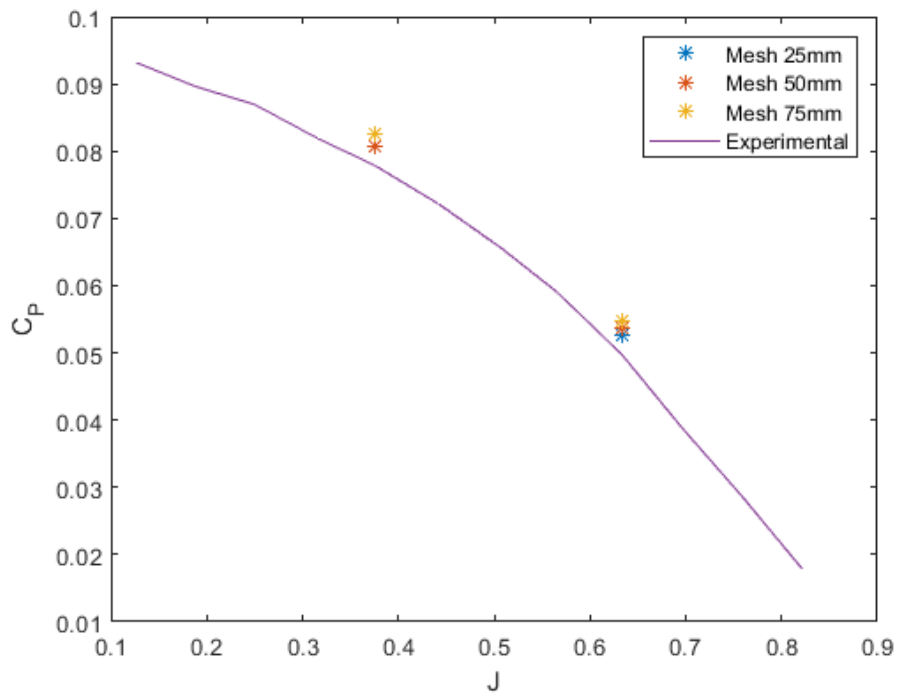


Figure 6.12: Power coefficient against advance ratio.

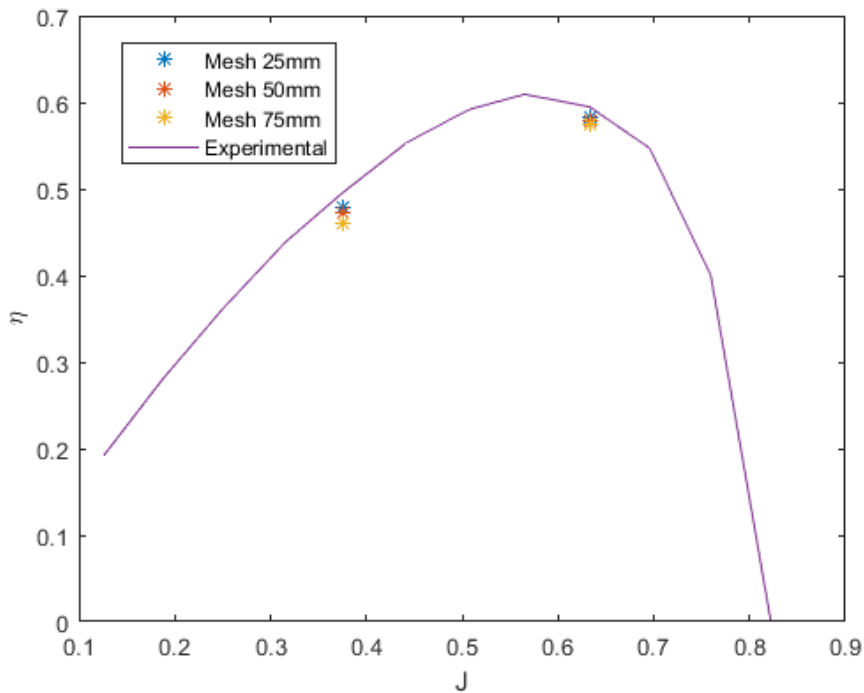


Figure 6.13: Efficiency for increasing advance ratio.

Results show in every case mesh refinement improves the solution. The fine and the standard grids result in very similar errors for $J=0.375$ whereas the coarse grid differs slightly more. Increasing the advance ratio reports bigger errors in both thrust and power coefficients whereas the efficiency errors are reduced for the second case. The influence of the advance ratio on the quality of the solution will be correctly studied in chapter 7. Overall errors between the fine and the standard mesh are under 2.2% difference between them therefore in the rest of this text the standard mesh is going to be used in order to save computational cost as fine grid has over double the number of cells than the standard grid.

6.3 Rotating region sensitivity analysis

The definition of the rotating domain dimensions is important to prevent reversed flow which may cause convergence problems and non-physical results. There is not much information about what should be this domain size, especially for UAV's propellers. Kutty et al [17] uses $0.4D$ and $1.1D$ and Mehdipour[11] uses $0.38D$ $1.15D$ although this is for a marine propeller. The selection of this domain needs to be large enough in order to allow the rotating flow to evolve correctly in the tangential and radial directions before leaving the rotating frame of reference. As commented on chapter 4, in order for this approach to produce realistic results, there should not be significant gradients in the radial direction. In a simple problem like ours where the whole geometry is axisymmetric and so the whole geometry could be assigned as the rotating region imposing the adequate boundary conditions on the outer walls. However the outer control volume could be any shape, for example if you are trying to reproduce a wind tunnel section, that may not be axisymmetric and therefore this approach is generally

mandatory. As seen in Chapter 4 STAR CCM+ uses the absolute velocity formulation where there is a source term which depends on the velocity, $\omega \times \vec{v}$, this means that if the velocity is not aligned with the rotation axis at the interfaces spurious fluxes will be created. Therefore it is important to ensure that the rotating domain is axisymmetric and big enough so that the normal components to the rotation axis of the flow velocity near these interfaces are almost zero. Table 6.12 shows the results to the sensitivity analysis respect to the length of the cylindrical rotating domain.

Table 6.12: Region’s length sensitivity analysis.

Region’s Length	C_T	C_P	η
0.2D	0.0964	0.0771	0.4688
0.4D	0.1017	0.0807	0.4723
0.6D	0.1018	0.0809	0.4718

It is clear that for 0.4D and 0.6D the values are almost the same and this is because of the axisymmetric outer control volume, the upper limit for the dimension of the volume of control is unbounded, nevertheless for real applications it is convenient to maintain the region enclosing the propeller as small as possible. The lower limit, on the other hand, presents a marked reduction in all the coefficients. The most probable cause for this reduction is that the flow at the interface is not completely perpendicular to the interface and as mentioned previously, unrealistic fluxes are being computed. Figures 6.14-6.16 show the velocity components variations with the axial coordinate measured by a probe set at $z=0.75R$ and $y=0$ compared with the unsteady simulations done with a single frame of reference approach.

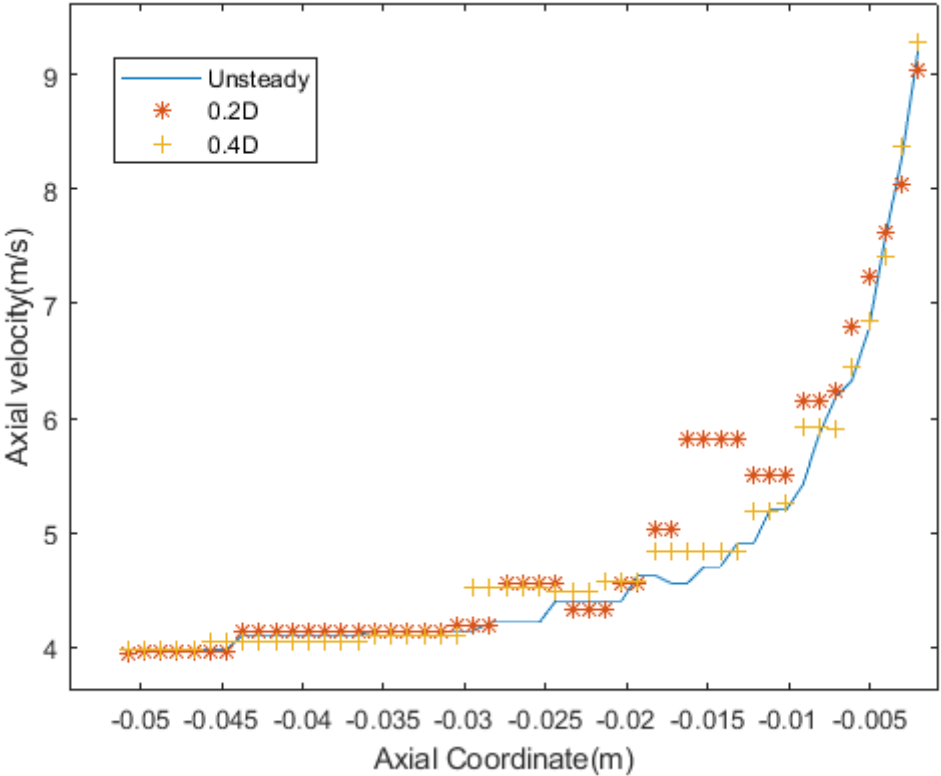


Figure 6.14: Axial velocity distribution along the axial coordinate measured by a probe set at $z=0.75R$ and $y=0$.

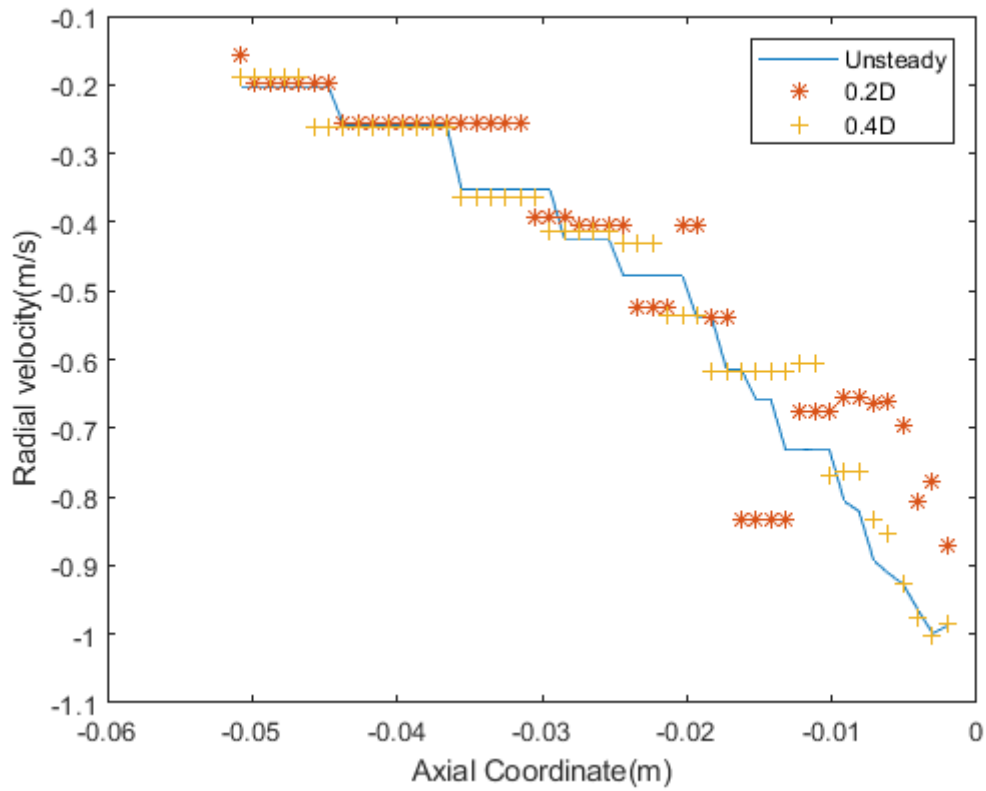


Figure 6.15: Radial velocity distribution along the axial coordinate measured by a probe set at $z=0.75R$ and $y=0$.

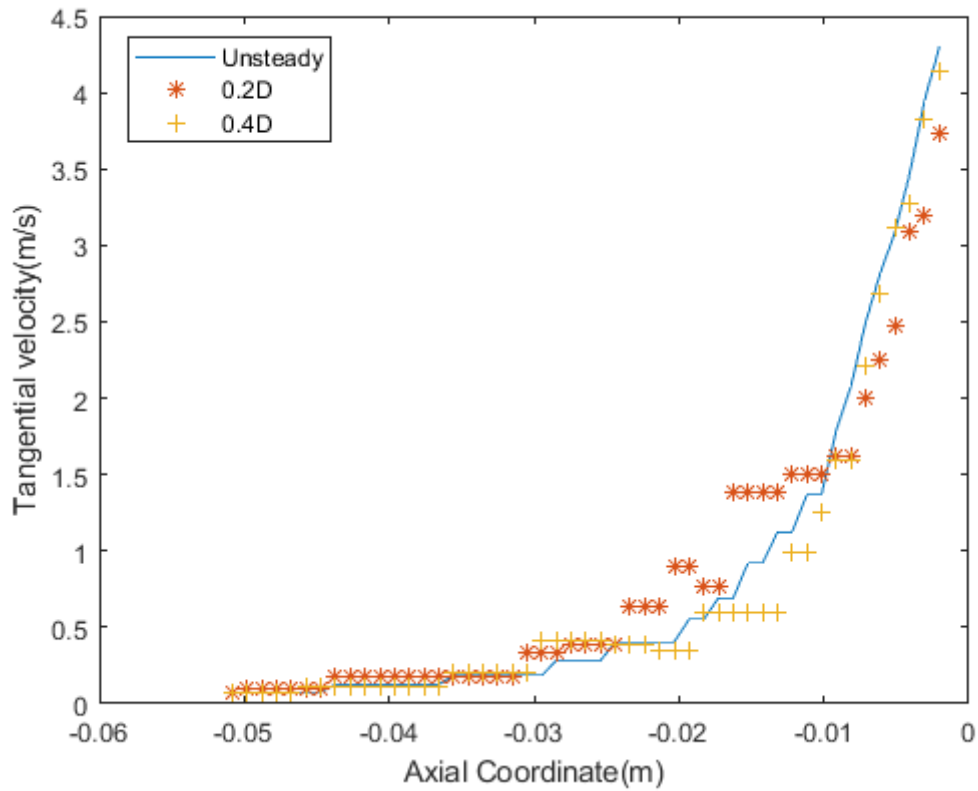


Figure 6.16: Tangential velocity distribution along the axial coordinate measured by a probe set at $z=0.75R$ and $y=0$.

It is clear that when the length of the rotating domain is 0.4D the velocity distributions reproduces significantly well the results from the unsteady simulation which should represent fairly well the real situation. On the other hand for the case 0.2D is clear that the flow has had no time to evolve, this generates different velocity distributions near the blade causing reduced thrust and power coefficients. The interface is placed at $x=-0.0127$ for the 0.2D case and $x=-0.0254$ for the case 0.4D. In both cases it is appreciable a transition from the steady reference frame to the rotating frame, characterized by a small jump, due to the previously commented extra fluxes that appear in the conservation equations. Nevertheless this transition for the 0.4D is much smoother than for 0.2D and does not affect the velocity distributions in the vicinity of the blade which is what really influences the performance of propellers.

An equivalent analysis is now done for the radial direction of our volume of control. Table 6.13 shows the results to the sensitivity analysis respect to the diameter of the cylindrical rotating domain.

Table 6.13: Region's Diameter sensitivity analysis.

Region's Diameter	C_T	C_P	η
1.05D	0.0996	0.0795	0.4688
1.1D	0.1017	0.0807	0.4723
1.15D	0.1025	0.0813	0.4728
1.25D	0.1028	0.0816	0.4724

Table 6.12 shows how the solution converges as the diameter grows. The biggest variation is between the cases 1.05D and 1.1D after this point differences are under 1% so all of them would provide reasonable approximations to the actual results. In this case something similar to the previous analysis occurs. Figures 6.17-6.20 show the evolution of the tangential velocity along the radial direction. The effect of setting the lateral boundary too close to the blade tip is clearly affecting the velocity distribution near the blade. The sudden jump in the value of tangential velocity can be explained by the change of the constitutive equations in the transition from the rotating to the steady state region as commented for the region's length sensitivity analysis. Equations in both regions are solved separately and the boundary conditions at the interface are interpolated via the local reference frame transformation shown at equation 4.1. The jump is progressively smoothed out as the interface moves away from the tips due to the fact that transition from one region to another occurs at a point in which the real tangential velocity is closer to zero and so the previously commented source term is approximately 0, making the fluxes more similar to the ones that would be generated in a single frame of reference approach such as in the unsteady simulation that will be explained on section 6.6. For the other velocity components the same behaviour occurs, however the effect is much clearer for tangential velocity.

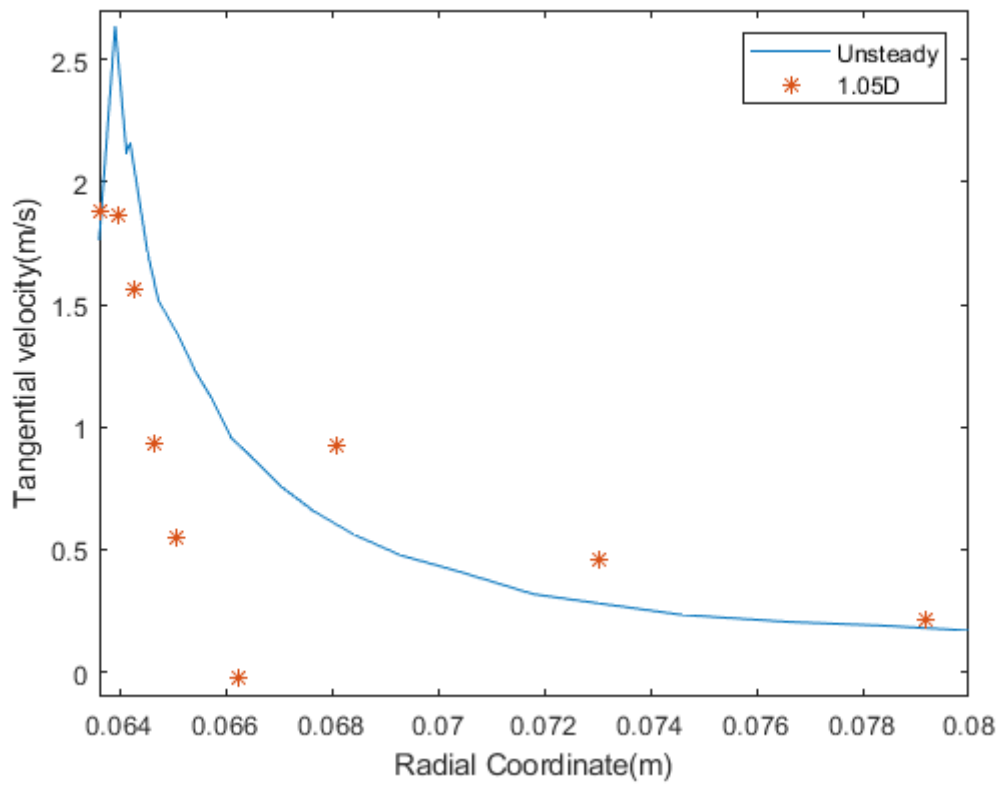


Figure 6.17: Tangential velocity along the radial coordinate for a rotating volume diameter of 1.05D.

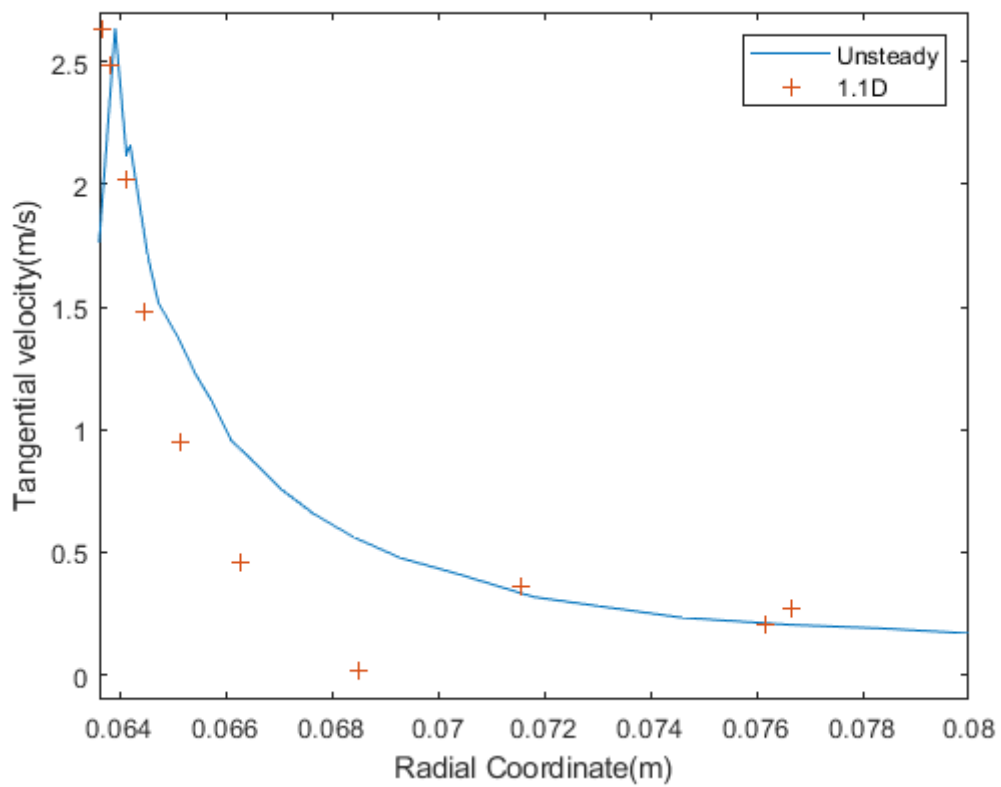


Figure 6.18: Tangential velocity along the radial coordinate for a rotating volume diameter of 1.1D.

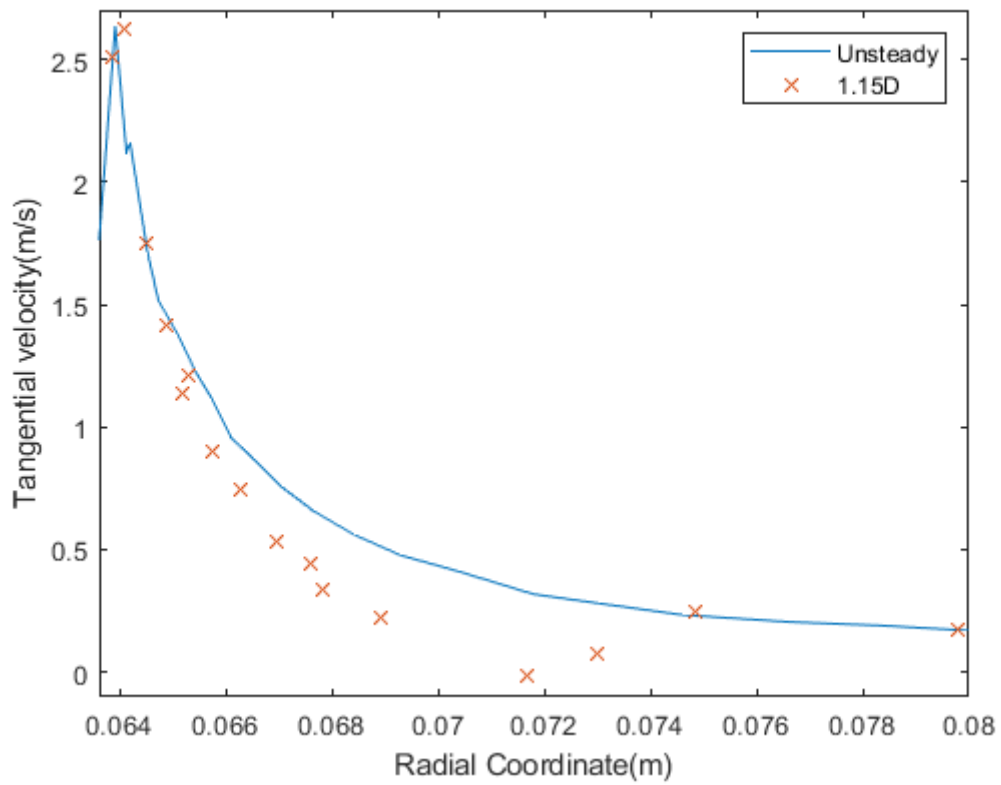


Figure 6.19: Tangential velocity along the radial coordinate for a rotating volume diameter of 1.15D.

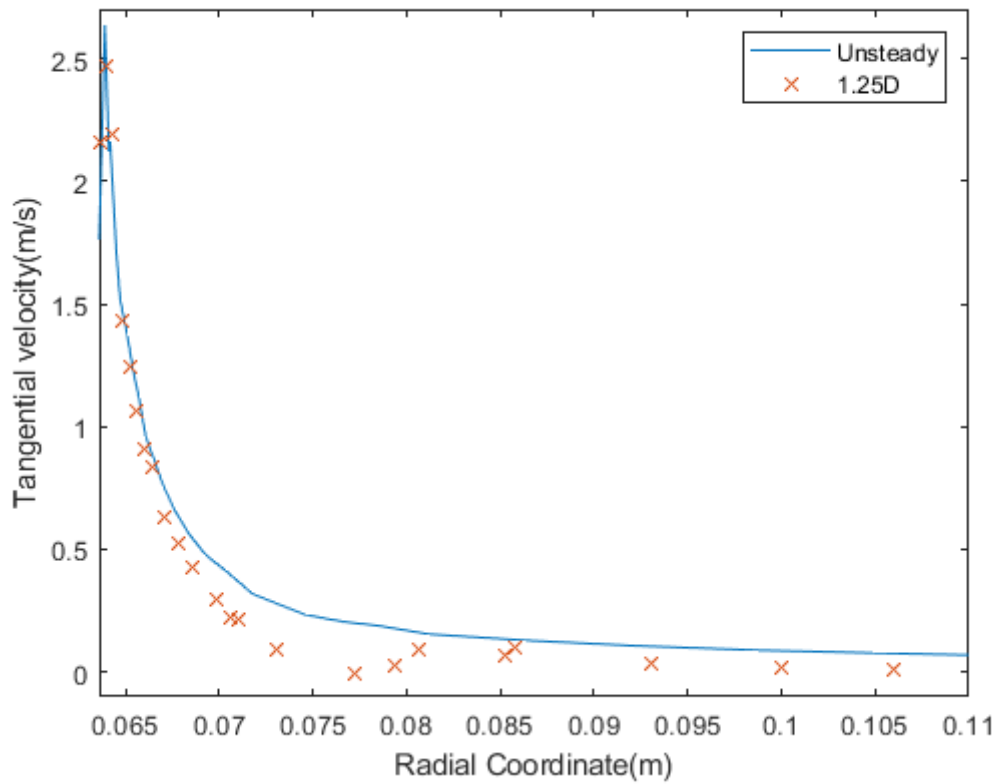


Figure 6.20: Tangential velocity along the radial coordinate for a rotating volume diameter of 1.25D.

6.4 Turbulence models

For the mesh refinements and sensitivity studies the $k - \omega$ SST model as it is the recommended selection within this popular family of turbulence models in aerospace applications by the STAR CCM+ User Guide [15] and as the results provided were concordant with experimental results. In this section different turbulence models will be tested to evaluate the influence, if any, on the prediction of propeller performance. The test will be carried out for an advance ratio of $J=0.375$. Table 6.14 shows the results accomplished by the different models tested. Due to the relatively low Reynolds number of our flow, around 25000, the problem was also solved with a laminar solver to see the global influence, if any, of the turbulence models.

Table 6.14: Results for advance ratio $J=0.375$ and different turbulence models.

Model	C_T	C_P	η
$k - \epsilon$ Realizable	0.0993	0.0768	0.4886
Standard $k - \omega$	0.1028	0.0821	0.4688
$k - \omega$ SST	0.1017	0.0809	0.4717
Spalart-Almaras	0.1063	0.0858	0.4646
Laminar	0.1063	0.0870	0.4581

Table 6.14 shows that there is a certain influence in the performance coefficients as the turbulence model is changed. It is clear that the Spalart-Almaras model provides very similar results to the laminar simulation this means that the model is not being able to predict accurately the presence of turbulence. Figures 6.21-6.24 show the distribution of the turbulent viscosity ratio for the different models tested, the Spalart-Almaras model is virtually solving the flow with a negligible turbulent viscosity apart from a small region in the wake. The results for the Laminar case and the Spalart-Almaras model overpredict experimental results. The $k - \epsilon$ model under predicts the experimental results, figure 6.21 shows that clearly the model is having some issues dealing with the rotation, generating unphysical distributions of turbulent viscosity. On the other hand both versions of the $k - \omega$ family seem to predict turbulence reasonably, with a transition towards the trailing edge and a fully developed turbulent wake. Furthermore the results represent adequately experimental performance.

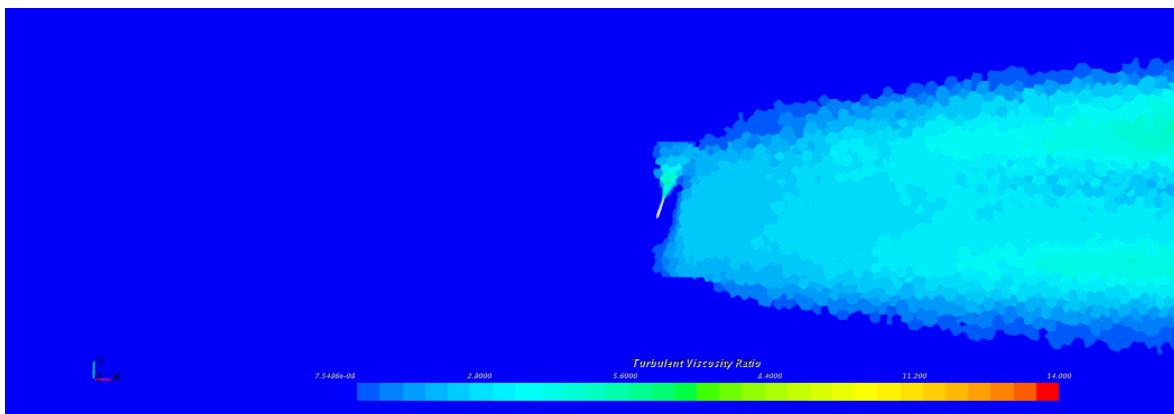


Figure 6.21: Turbulent Viscosity ratio for model: $k - \omega$ SST. $z=-0.03$.

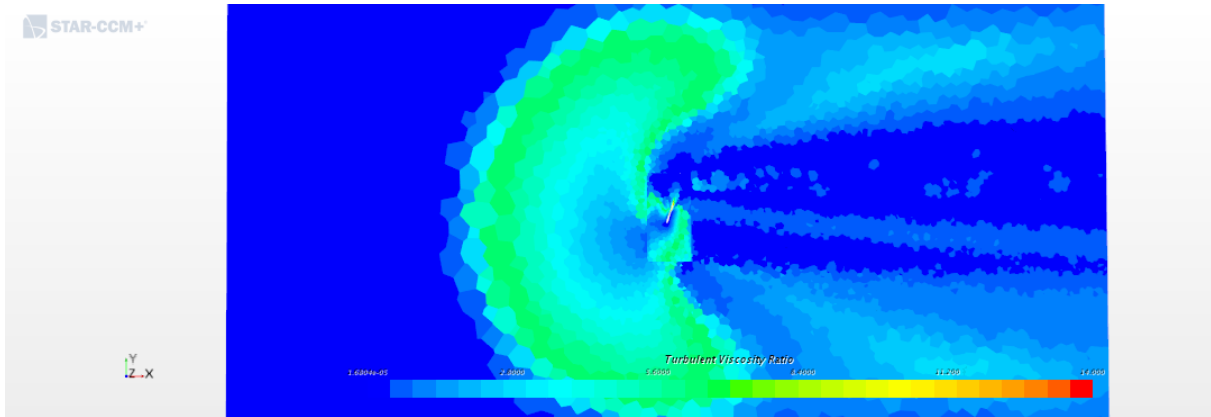


Figure 6.22: Turbulent Viscosity ratio for model: $k - \epsilon$ Realizable . $z=-0.03$.

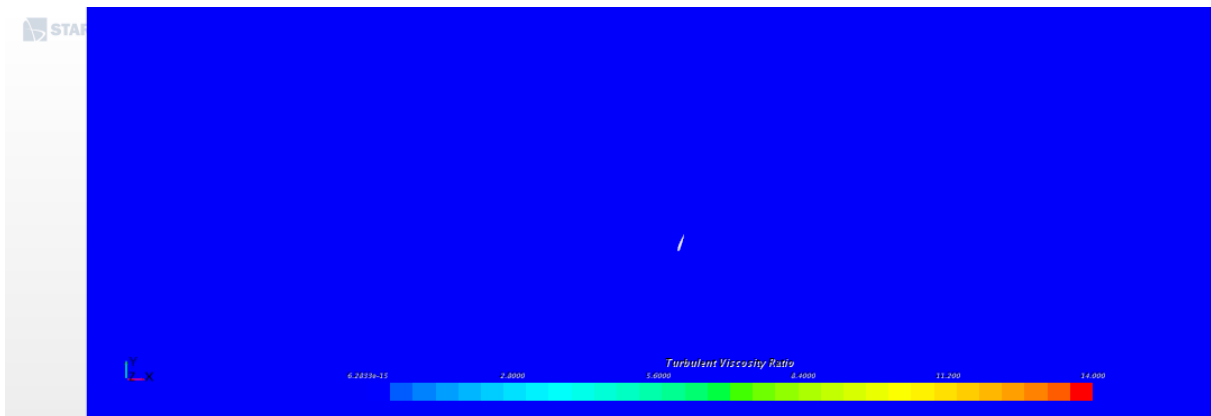


Figure 6.23: Turbulent Viscosity ratio for model: Spalart-Almaras. $z=-0.03$.

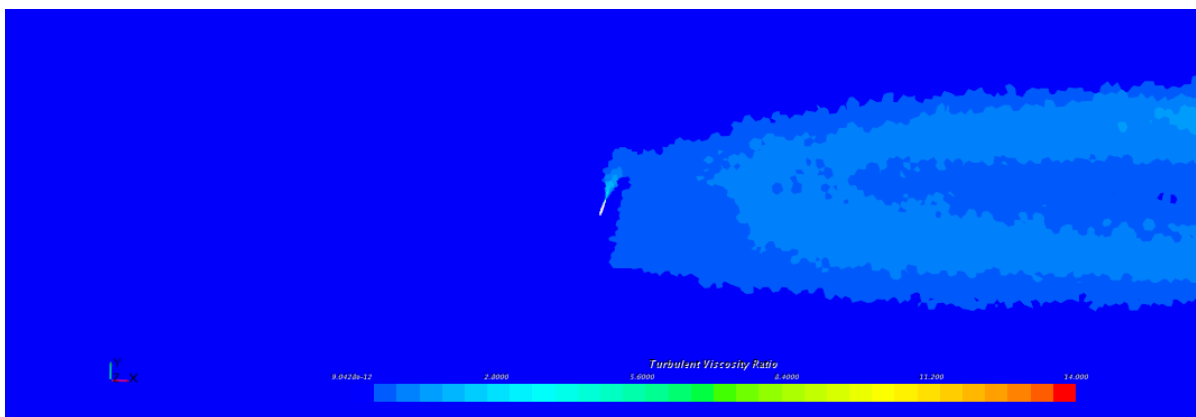


Figure 6.24: Turbulent Viscosity ratio for model: $k - \omega$ standard. $z=-0.03$.

6.5 Interface and boundary conditions effects

Different boundary conditions at the lateral outer surface were considered. A no-slip boundary condition could be implemented to mimic the case of a real wind tunnel in validation cases or a freestream boundary condition could be imposed to model the actual flight conditions of UAV's for example. However the problem is defined with this lateral surface sufficiently far away from the propeller and therefore is shown unaffected by the kind of boundary condition.

Table 6.15: Lateral boundary condition effect on performance for $J=0.375$.

Lateral B.C	C_T	C_P	η
Freestream	0.1028	0.0817	0.4718
No slip(Wall)	0.1028	0.0816	0.4724

Errors are insignificant considering that they are obtained averaging an oscillatory solution.

Another study was performed to assess the influence of the type of interface done to link fluid variables in the rotating and static regions. Two kind of interfaces were studied, an internal interface which performs a direct frame of reference transformation at the interface and a mixing plane interface which takes the values of the fluid variables, performs a circumferential average and these values are then passed to the other region. This second approach is interesting as the circumferential average mimics the effect of the propeller being rotated smoothing the gradients at the interface. Nevertheless the domain has been chosen in a way that the non-axisymmetric components of velocity are very close to zero, therefore big differences are not expected.

Table 6.16: Lateral boundary condition effect on performance for $J=0.375$. Rotating domain 1.25D.

Interface	C_T	C_P	η
Mixing plane	0.1028	0.0818	0.4717
Internal interface	0.1028	0.0816	0.4724

Errors are once again insignificant considering that they are obtained averaging an oscillatory solution. If the problem's geometry required a smaller rotating domain where gradients were not yet evolved at the interface the difference will be more important. To show this effect the case of rotating domain having a diameter of 1.05D was also studied with the mixing plane approach.

Table 6.17: Interface effect on performance for $J=0.375$. Rotating domain diameter=1.05D.

Interface	C_T	C_P	η
Mixing plane	0.1007	0.0804	0.4694
Internal interface	0.0996	0.0795	0.4688

It is clear that for small diameter rotating control volume the mixing plane approach provides slightly more accurate results as unphysical gradients created at the interphase would be smoothen out. The effect with short lengths of the volume will also be assessed, in this case this boundary condition will act as an extra stirring of the flow which hasn't had time to evolve into an axisymmetric wake, and this will presumably improve the approximation of the results.

Table 6.18: Interface effect on performance for $J=0.375$. Rotating domain length=0.2D.

Interface	C_T	C_P	η
Mixing plane	0.09961	0.0792	0.4719
Internal interface	0.0964	0.0771	0.4688

As it was predicted, in this case, the mixing plane interface performed an improvement on the estimation of the experimental results. Nevertheless this technique improves the result by imposing an unphysical condition so it must be done carefully. The best way to proceed will be to apply any of the interface techniques but keeping in mind that the rotating domain has to be big enough to let the flow field evolve completely inside the rotating frame of reference. This way is the only way to ensure that the approximation represents adequately the real velocity gradients.

6.6 Unsteady Simulation: Rigid Body Motion

As commented on chapter 4, unsteady simulations are very expensive computationally, especially for high rotation rates as, in order to obtain time accurate results, the time step should be as small as 1° - 2° per time step. Therefore, these simulations are normally restricted to situations where transient effects are important. In order to check the validity of the steady-state simulations, an unsteady simulation has been performed with a similar mesh and considering a single frame of reference approach to allow also the validation of the rotating region domain. In this simulation the fact of having a cylindrical outer boundary was used to allow the whole mesh to rotate, imposing a no-slip condition on the propeller and a wall relative velocity of $-\Omega$ on the outer wall to emulate the no slip conditions. STAR CCM+ provides the possibility of implementing an equivalent method to Multiple Frame of Reference Approach for unsteady simulations by using Sliding mesh techniques. These approaches consist on two regions, one with an assigned rotational motion in which the grid rotates and another with a static grid. At the interface the rotating grid slides over the static domain. This allows the possibility of having complex, non-axisymmetric geometries, for example a complete helicopter or a UAV model or if the outer wall was representing a non-circular section of a wind tunnel.

Except the implicit unsteady and Rigid Body Motion solvers, the setup for the simulation was identical as in the previous case. SST $k - \omega$ turbulence model was selected, segregated solver and same boundary conditions. The mesh is slightly different due to the fact that the boundary of the rotating region is not available to impose surface controls. The wake refinement was applied to the propeller instead.

Time step selection was done according to the STAR CCM+ user guide which recommends 1° - 2° per time step. Considering a rotational velocity of 4546 RPM as in the previous case, the time step selected should be between $(3.66-7.33) \cdot 10^{-5}s$ solving 1° - 2° per time step, this is very small considering that at least a few revolutions have to be solved. The computational cost of this unsteady simulation is very high; this is the reason why the validity of the steady state approaches is being studied. Nevertheless the unsteady simulation was done only for one advance ratio to check both the performance coefficients and the flow field around the propeller especially to account for the modifications in this caused by the rotating and static domains interface and also the unsteady effects which may have a non-zero average effect on the performance coefficients. Simulations were done with time steps $2.5 \cdot 10^{-5}s$ and $5 \cdot 10^{-5}s$ reporting no differences in the performance coefficients. Figures 6.27 and 6.28 show the evolution in time of the thrust and power coefficients for time step $2.5 \cdot 10^{-5}s$. It is clear how they arrive to an oscillatory regime; the mean values are compared with the values obtained for the steady state simulations in table 6.19.

Table 6.19: Performance coefficients results of the unsteady simulation for $J=0.375$ and $\Omega = 4546 \text{ RPM}$

	C_T	C_P	η
MFRA(0.4Dx1.25D)	0.1028	0.0816	0.4724
Unsteady	0.1031	0.0819	0.4721

Considering the differences in the meshes and that one simulation strategy is steady state and uses a multiple frame of reference approach, the results differing under 0.5% shows that with an appropriate mesh and correctly chosen rotating region the steady state approach is able to represent adequately the mean values obtained by unsteady simulations for propeller performance analysis. This is a huge advantage as the computational cost is much lower. Considering simulating only 10 revolutions with the recommended time step of $3.66 \cdot 10^{-5}s$, starting from a previously calculated steady state solution the computational time using 2 processors would be 105 hours, whereas a steady state run, which takes around 700 iterations to converge which will result in 2.9 hours. Figures 6.27 and 6.28 show the evolution in time of the thrust and power coefficients for approximately 10 revolutions of the propeller. The previous steady state solution from which this simulation started was calculated with the unsteady solver using a high time step for simplicity. Figures 6.25 and 6.26 show the pressure contours on the propeller blades, it is clear how the low pressure regions generated on the rear parts of the blades and the high pressure regions on the front, are responsible for the blade to be propelled forward. Figures 6.29-6.31 show the pressure contours over the propeller and the axial distribution for both Multiple Frame of Reference Approach and unsteady simulations. Pressure contours are almost identical which combined with the very small discrepancy in the performance coefficients proves that the unphysical gradients generated at the interfaces of the rotating domain are not affecting the results and that unsteady effects do not influence greatly the performance of propellers under this operating conditions. Figure 6.31 shows a global agreement in the slipstream characteristics provided by both simulations, but some slight differences can be pointed out, for example slightly lower velocities on the unsteady simulations and different wake behind the cylindrical hub. It is interesting to comment on the wake generated behind the cylindrical hub, which clearly differs in both simulations; this is due to the fact that the steady simulation is not able to reproduce typical unsteady vortex emission downstream of a blunt body whereas the unsteady simulation can. Figure 6.32 shows a detailed image of the wake for the unsteady simulation, where an oscillating wake

pattern can be appreciated. Nevertheless these small differences do not affect significantly the overall pressure distribution and therefore the performance coefficients.

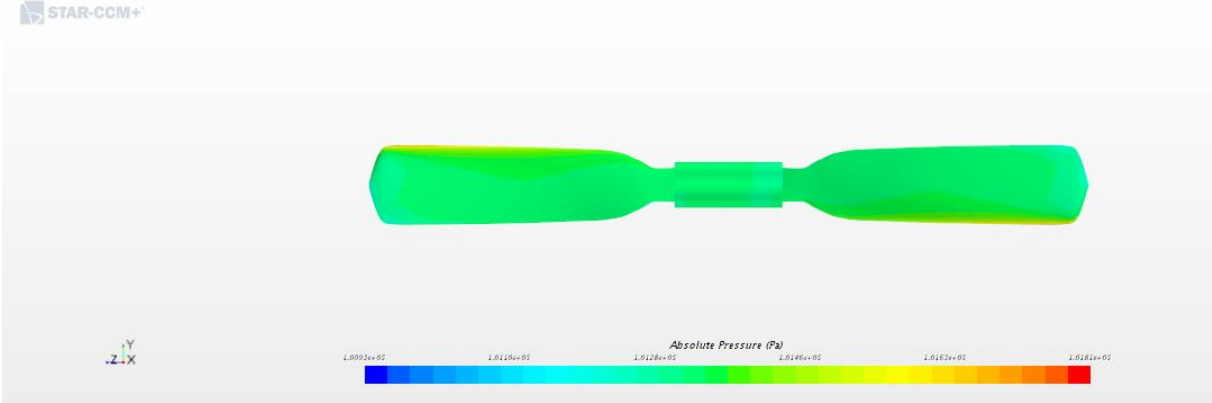


Figure 6.25: Back view of the propeller with pressure contours.

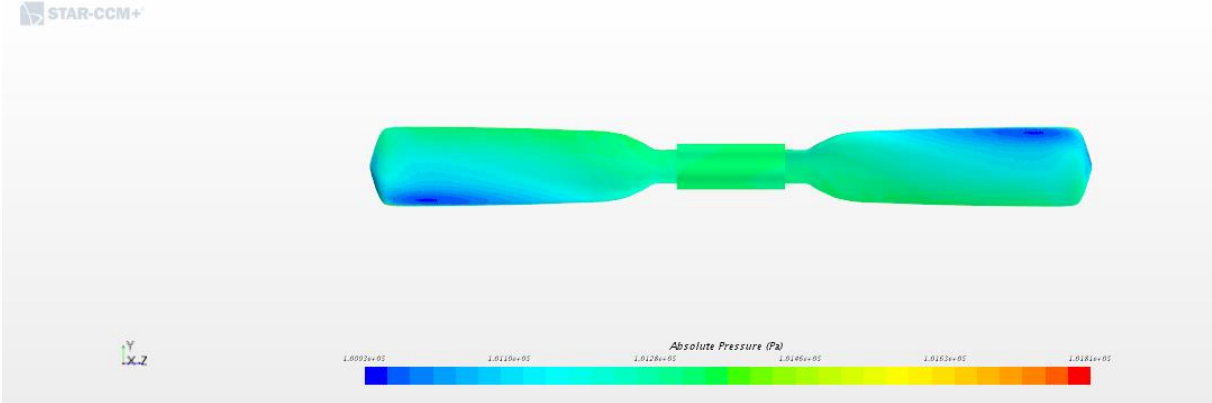


Figure 6.26: Front view of the propeller with pressure contours.

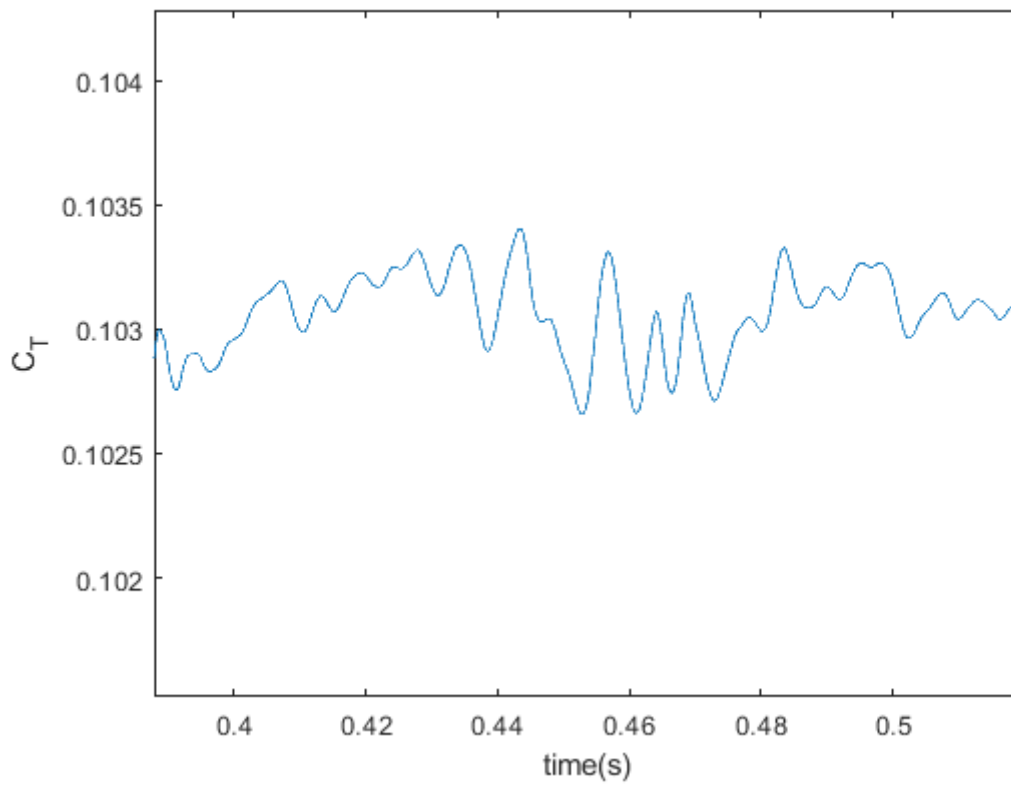


Figure 6.27: Thrust coefficient evolution in time for unsteady simulation.

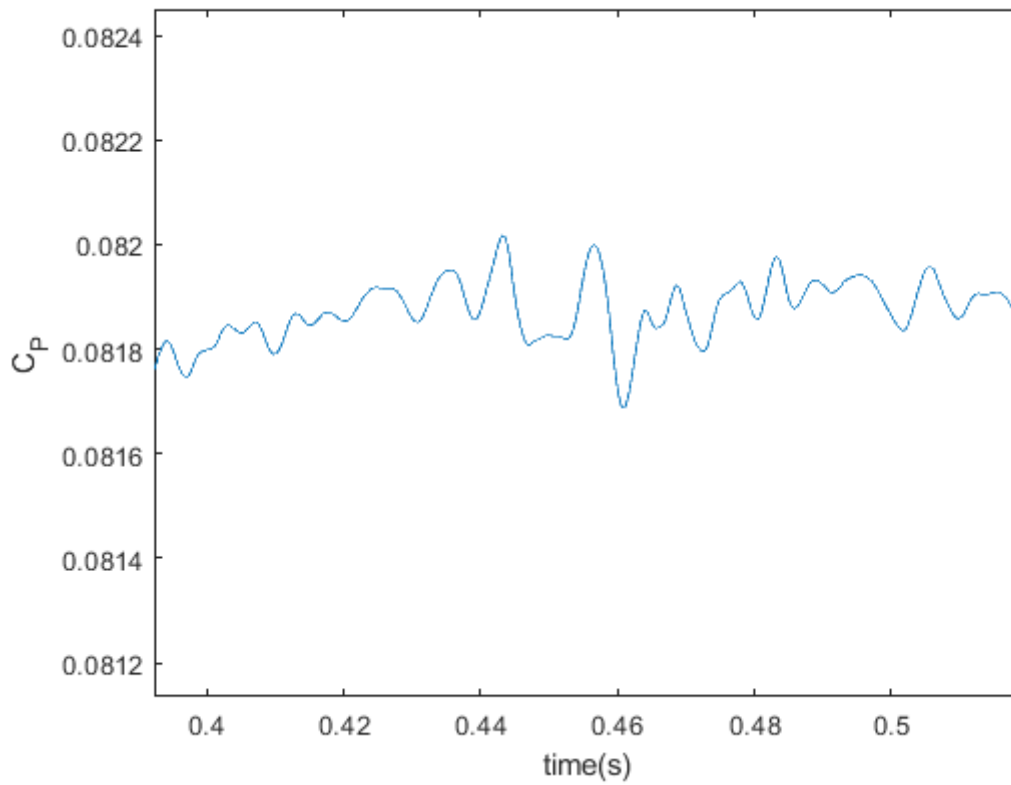


Figure 6.28: Power coefficient evolution in time for unsteady simulation.

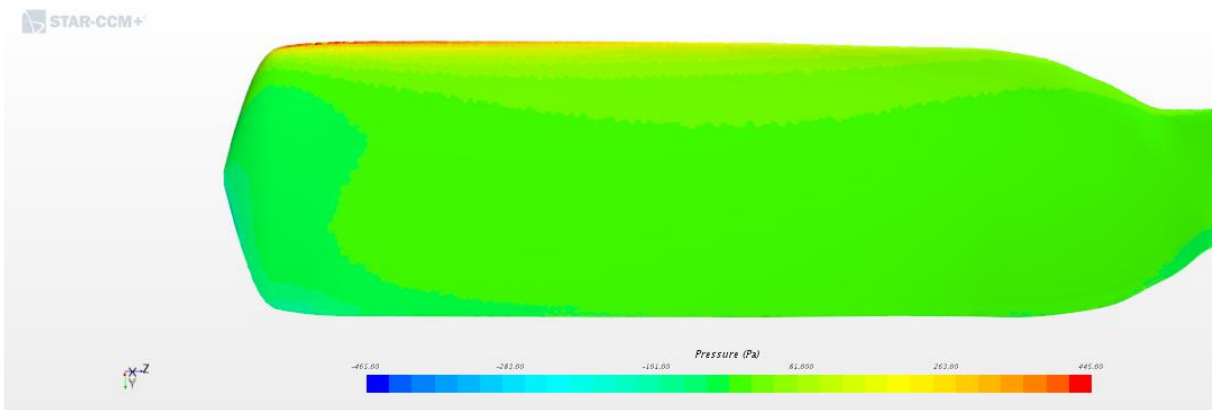
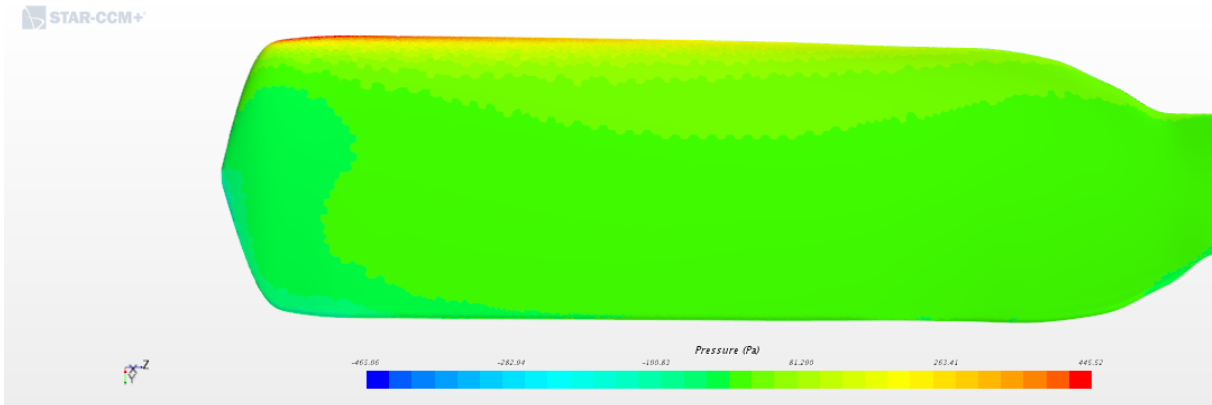


Figure 6.29: Back view of the propeller with pressure contours. Multiple frame of reference(Top). Unsteady(Bottom).

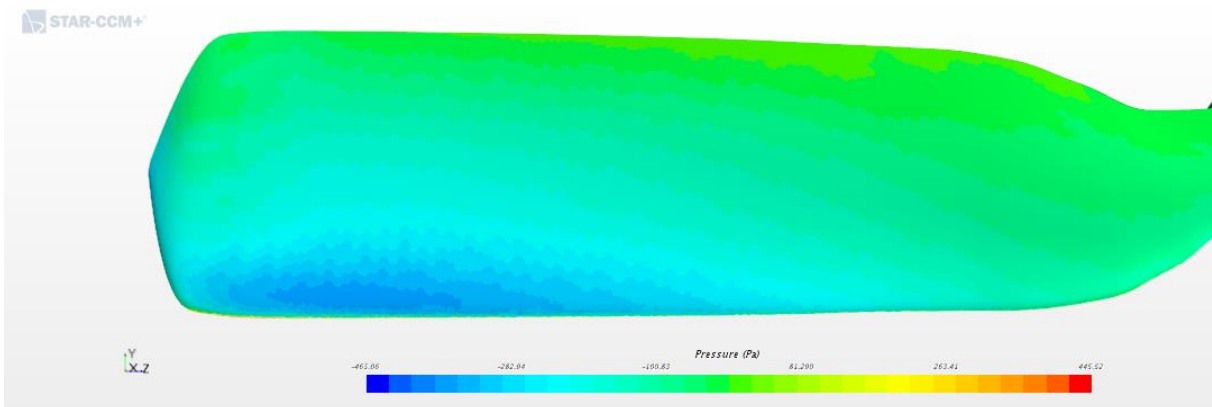
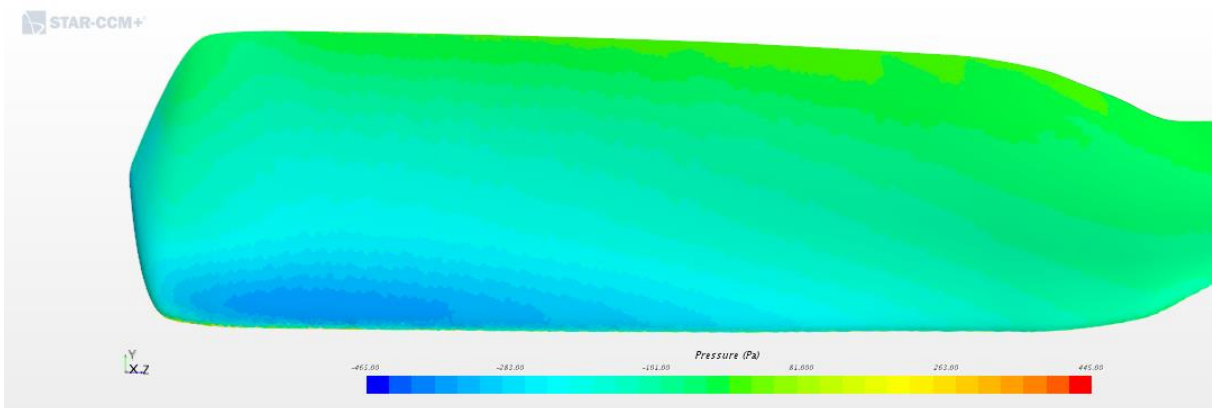


Figure 6.30: Front view of the propeller with pressure contours. Multiple frame of reference(Top). Unsteady(Bottom)

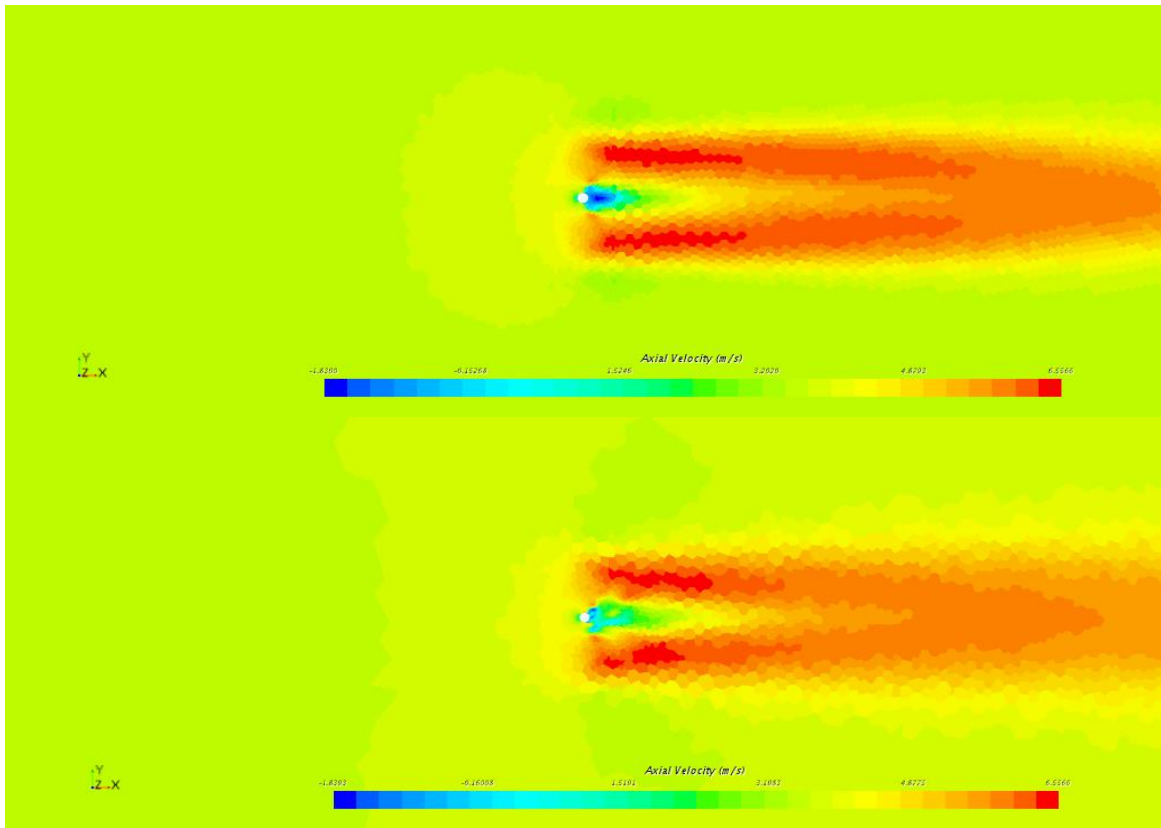


Figure 6.31: Axial velocity contours at $z=0$. Multiple frame of reference(Top). Unsteady(Bottom)

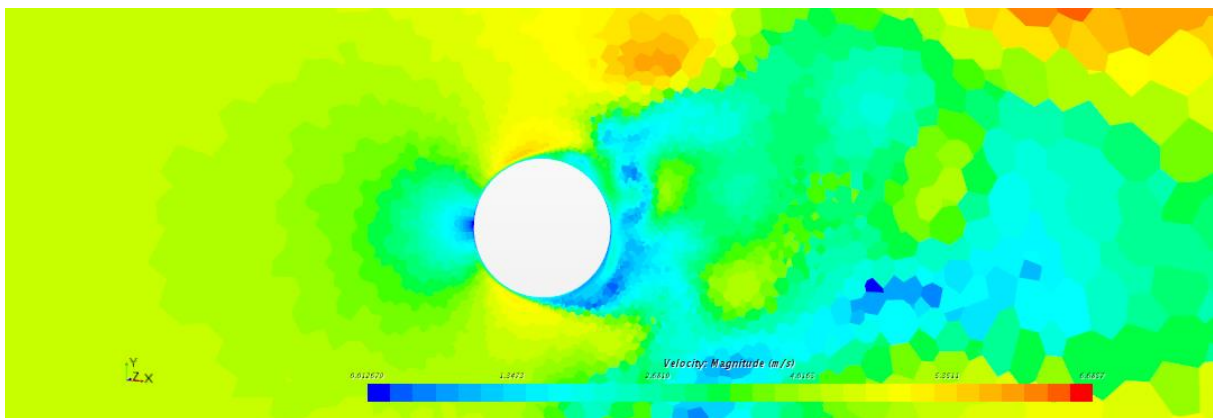


Figure 6.32: Detail of wake behind cylindrical hub in unsteady simulation.

7 Performance Results: DA4022

Taking into account the validation studies exposed in the previous chapter the full performance tests will be carried out for the standard mesh, a rotating domain of $0.4D$ length and diameter $1.25D$ and $k - \omega$ SST turbulence model. Figures 7.1-7.6 show the performance curves for the experimental tests and CFD simulations. First set of simulations were done for 4546 RPM as the validation case. Then a new set of simulations were performed with a higher rotational speed to try to account the influence of the Reynolds Number. In this case the rotation rate will be of 7559 RPM. Figures 7.1-7.3 account for the performance coefficients of the simulation associated with $\Omega = 4546 \text{ RPM}$ and figures 7.4-7.6 for $\Omega = 7559 \text{ RPM}$. CFD simulations are able to reproduce experimental results. Table 7.1 show the relative errors for both sets of simulations with the experimental results. For $\Omega = 4546 \text{ RPM}$ relative errors are below 10% for all coefficients except for the higher advance ratios where the small value of the coefficient makes this error rise, especially for the thrust coefficient error which reaches a value of 39% error for the highest advance ratio. Figure 7.1 shows how for low advance ratios CFD simulations under predicts experimental results for the thrust coefficient, whereas for higher advance ratios they over predict experimental results. Figure 7.2 shows how the power coefficient is globally over estimated for all advance ratios. As explained in section 3.2, the power coefficient is a crescent function of both the lift coefficient and the power coefficient whereas the thrust coefficient is a crescent function of the lift coefficient and a decreasing function of the drag coefficient. These trends suggest that both the drag and the lift coefficients are being overestimated. For $\Omega = 7559 \text{ RPM}$ relative errors are below 10% for all coefficients. Figure 7.4 shows how for low advance ratios CFD simulations under predicts experimental results, being the under prediction for low advance ratios considerably bigger than for the higher ones. Figures 7.4-7.5 shows how the power coefficient has a similar trend as the thrust coefficient. A possible explanation of these trends would be a reduction in the lift coefficient and increase in the drag coefficient in some sections of the blade due to the erroneous prediction of stall effects in our model. This erroneous prediction of stall could be due to an increase in the pitch angle in our geometric model or due to the turbulence model used. Another possible explanation would be more significant aeroelastic effects for higher rotation rates and low advance ratios where the outer region is more loaded increasing thrust and power coefficients.

Table 7.1: Comparison between CFD and experimental results.

$\Omega = 4546 \text{ RPM}$				$\Omega = 7559 \text{ RPM}$			
J	Error C_T	Error C_P	Error η	J	Error C_T	Error C_P	Error η
0.188	-3.1027	4.7268	-7.472	0.1131	-9.0052	-6.1606	-3.027
0.24	-4.1516	1.812	-5.7297	0.1693	-8.4044	-5.5618	-2.9467
0.2919	-2.9812	2.7284	-5.3104	0.2256	-7.9263	-5.0574	-3.0124
0.3439	-1.1886	3.9818	-4.7044	0.2818	-6.2392	-3.6084	-2.6389
0.3958	-0.0902	4.7924	-4.3956	0.3381	-6.4984	-3.6496	-2.9276
0.4478	0.394	5.7321	-4.9342	0.3943	-5.2202	-2.4873	-2.6934
0.4998	1.8216	6.8901	-4.587	0.4506	-5.6061	-3.1109	-2.5272
0.5517	2.9247	8.0227	-4.4277	0.5068	-6.2431	-3.1311	-3.0575
0.6037	5.5699	9.4735	-2.6229	0.5631	-5.2682	-1.9361	-3.325
0.6557	9.761	12.144	-0.8163	0.6193	-3.1291	-0.0621	-2.7798
0.7076	18.2141	17.6858	2.433	0.6756	-0.456	2.3485	-2.3621
0.7596	39.0873	23.8482	12.3863	0.7318	7.6642	6.6905	1.9454

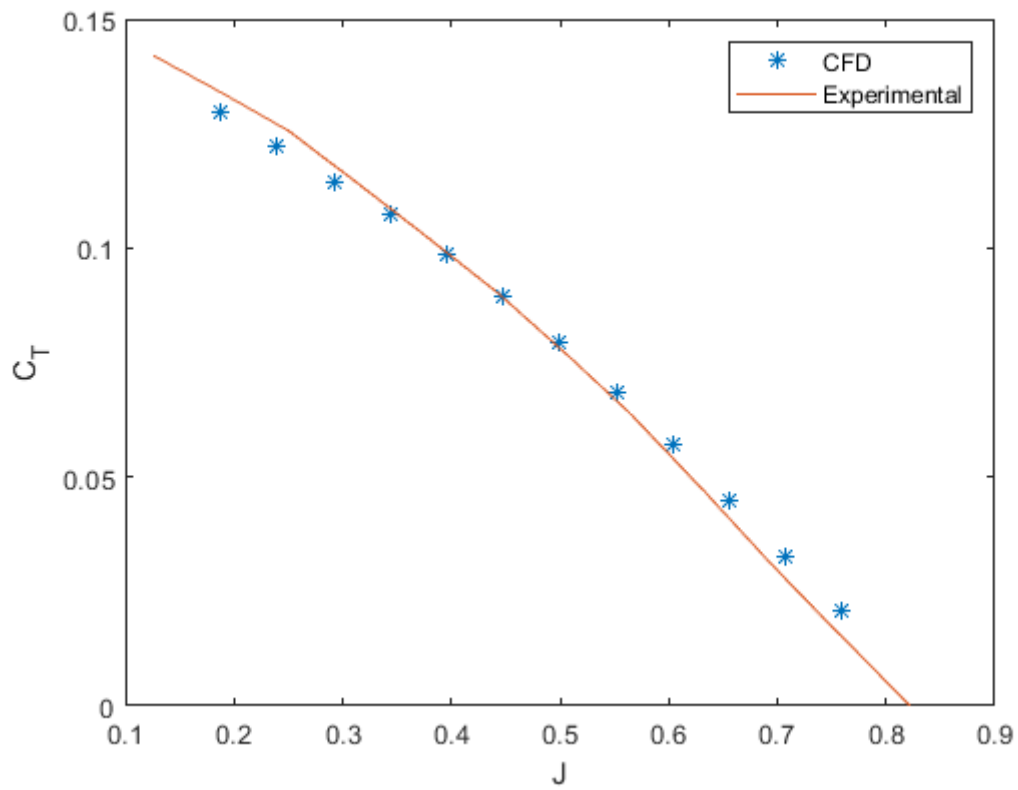


Figure 7.1: Thrust coefficient for $\Omega = 4546$ RPM .

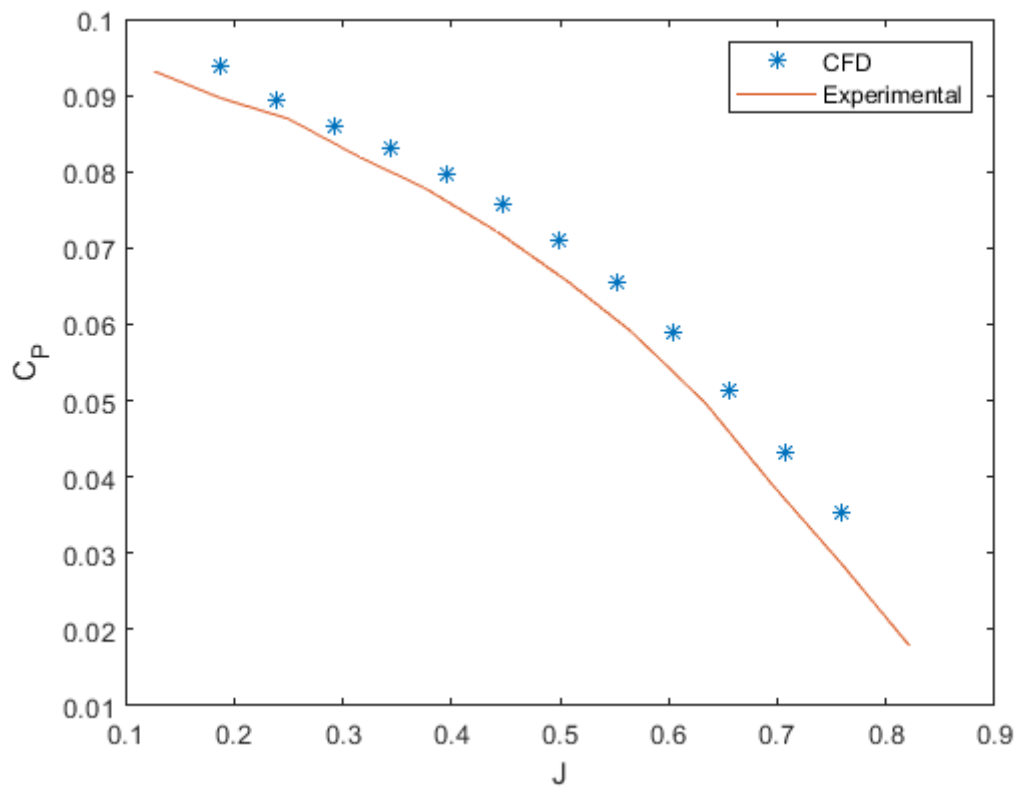


Figure 7.2: Power coefficient for $\Omega=4546$ RPM .

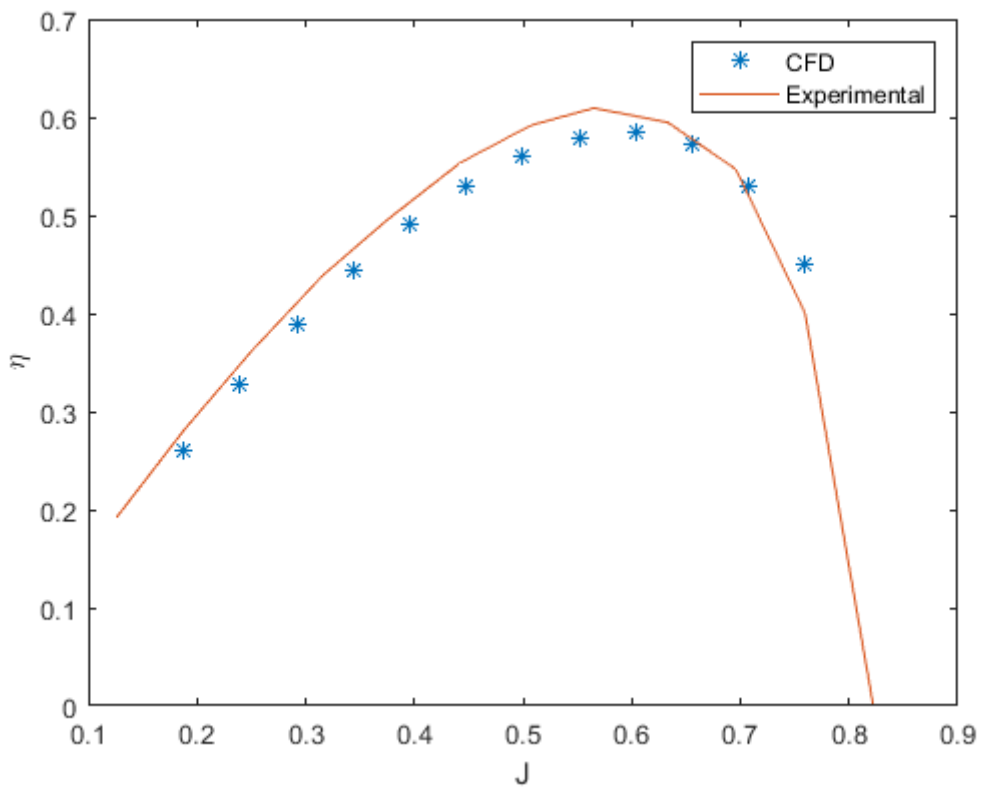


Figure 7.3: Efficiency for $\Omega=4546$ RPM .

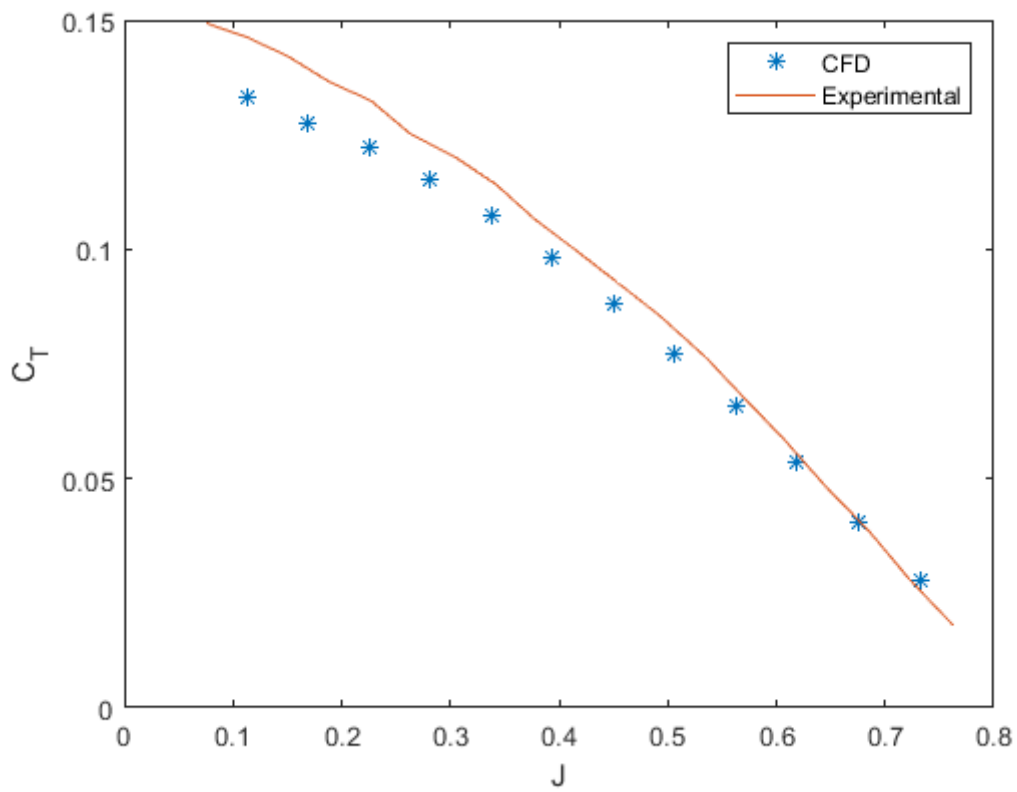


Figure 7.4: Thrust coefficient for $\Omega=7559$ RPM .

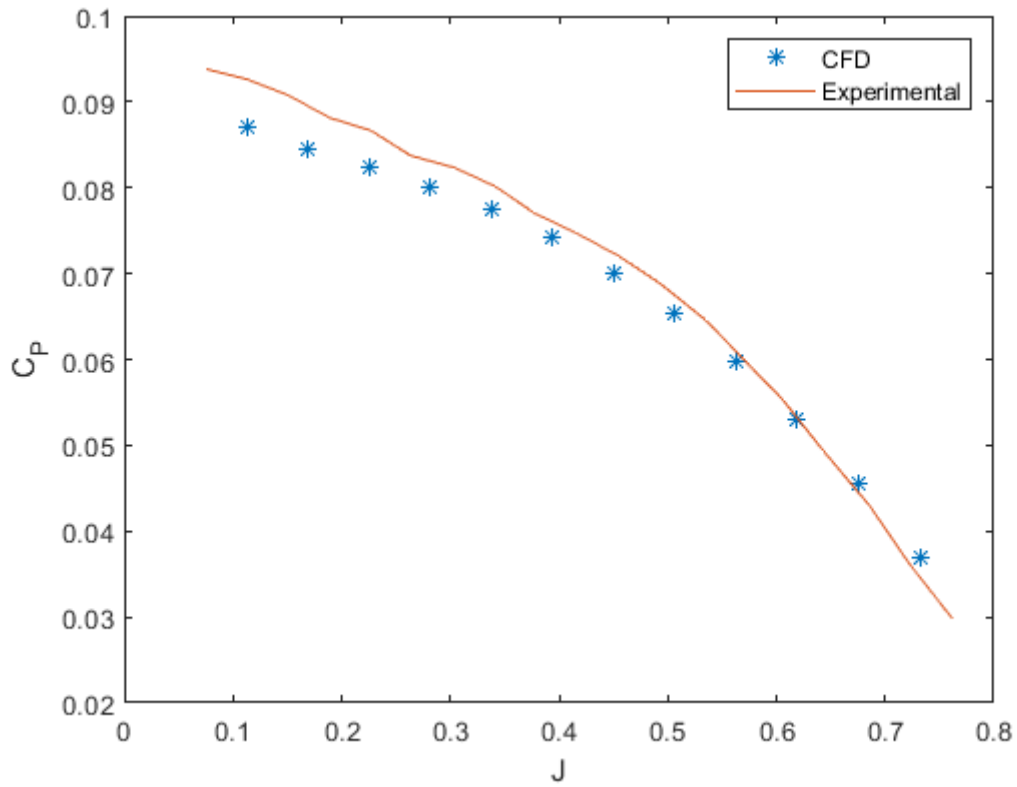


Figure 7.5: Power coefficient for $\Omega=7559$ RPM.

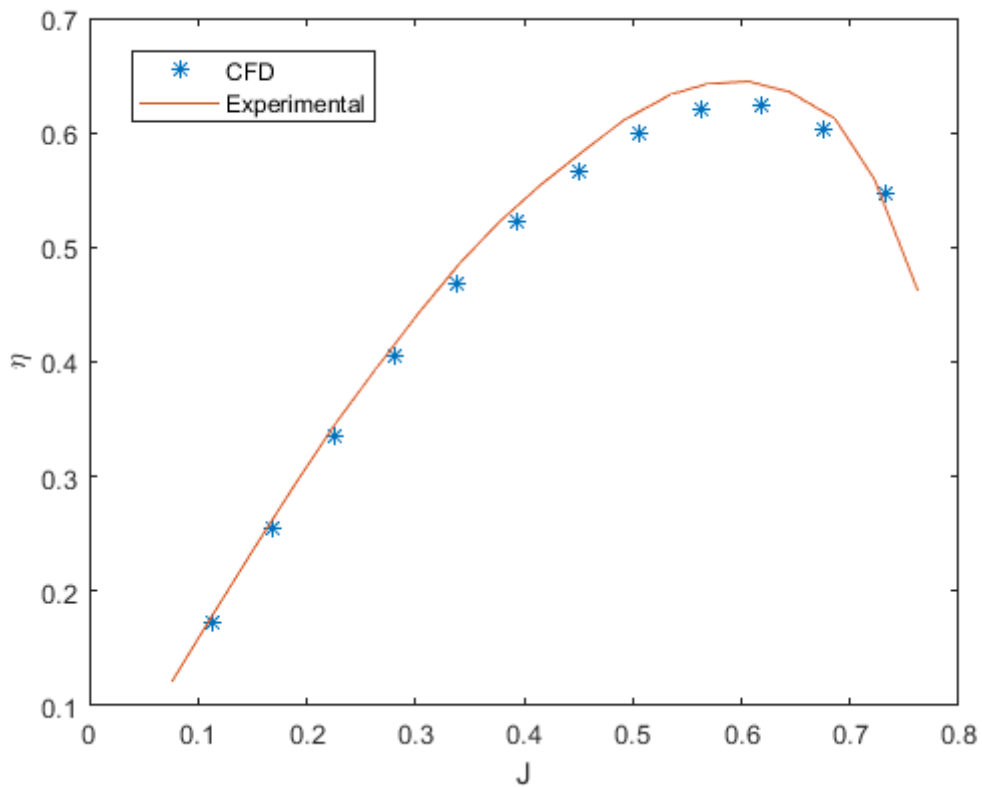


Figure 7.6: Efficiency for $\Omega=7559$ RPM.

Figures 7.7-7.9 show the comparison of the CFD simulations performed for the two previous rotational speeds. The Reynolds Number associated to these rotation rates are:

$$\Omega = 4546 \text{ RPM} \rightarrow Re = 21662 \tag{7.1}$$

$$\Omega = 7559 \text{ RPM} \rightarrow Re = 36020 \tag{7.2}$$

Figure 7.9 shows how CFD simulations are able to reproduce the predicted deterioration of performance for decreasing Reynolds numbers. Being able to predict these low Reynolds number effects is a really important aspect of CFD approaches compared with other approaches such as Blade Element Momentum method (BEM) which has problems predicting performance for small scale propellers. Increasing the Reynolds number by only 66% produces an increase in the maximum efficiency of 3.85%.

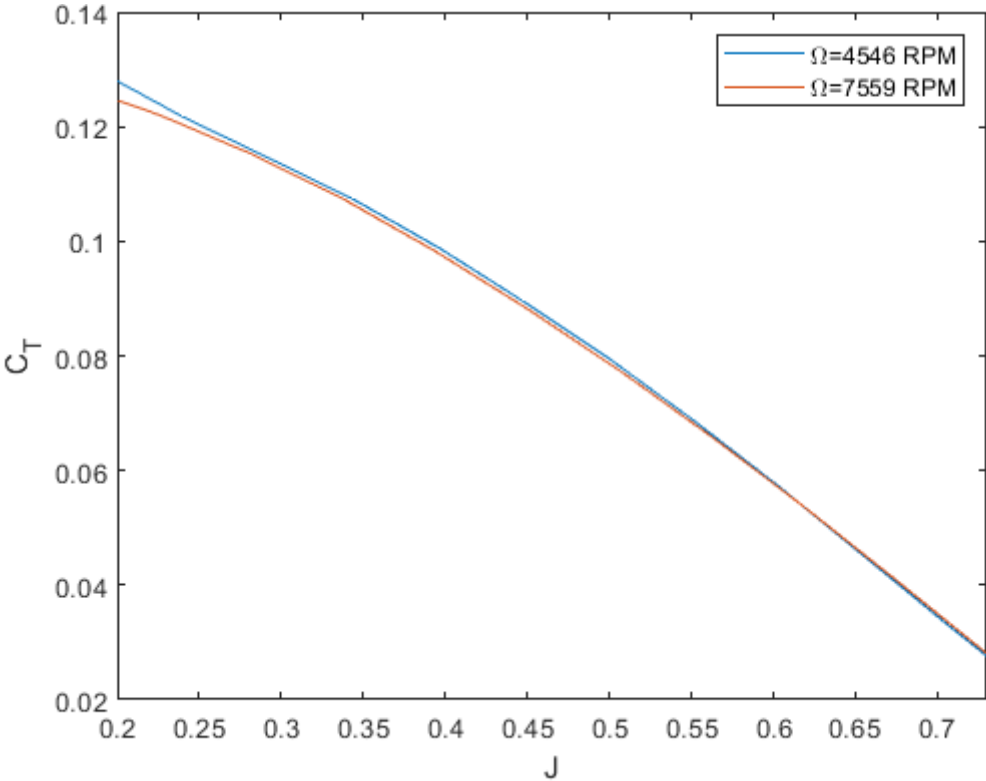


Figure 7.7: Thrust coefficient for different rotation rates.

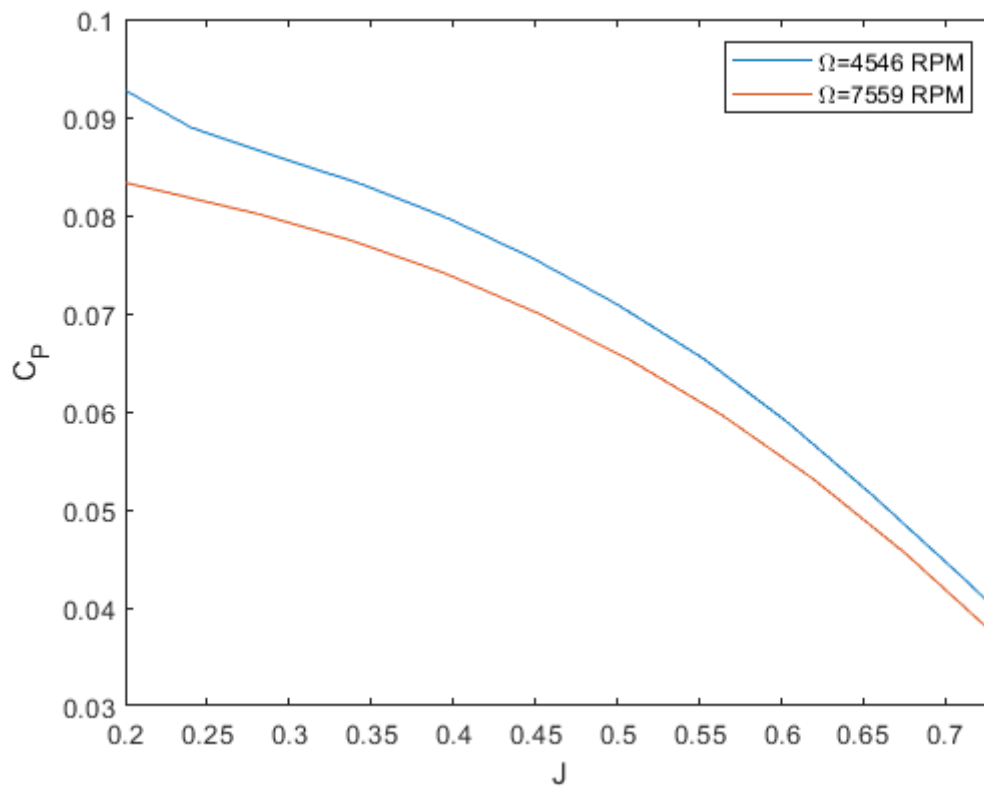


Figure 7.8: Power coefficient for different rotation rates.

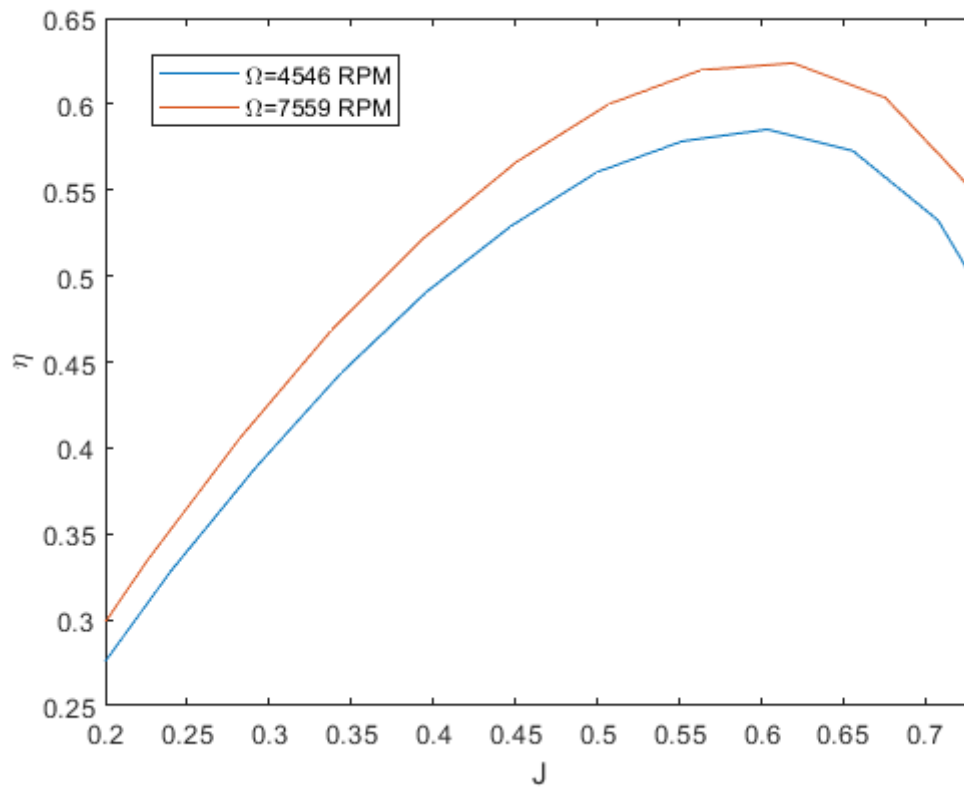


Figure 7.9: Efficiency for different rotation rates.

8 APC slow flyer:10x7

After the consistent results found for the benchmark case of the prototype DA4022, a new, more complex propeller model was modelled. The APC slow flyer 10x7 is a commercial propeller with a considerably complex geometry, variable chord, pitch, non-straight 50% chord line and a transition from an Eppler-63 low Reynolds number aerofoil inboard to a Clark Y aerofoil near the tip. One of the most problematic aspects of CFD simulations for small scale propellers is the difficulty of being sure that the actual geometry is represented well by the CAD model used for the simulations. Manufacturing of these propeller blades are often not very accurate due to the chord being about 2 cm and the thickness of the aerofoils about 2mm. This causes deviations on the pitch distributions for which propeller performance has a great sensitivity. This problem is even bigger considering that manufacturers do not provide geometry details of their blades apart from the diameter and pitch at 75% chord. In order to try to reproduce well the geometry of this blade the following procedure has been followed:

1. Take pictures of the top and front views of the propeller.



Figure 8.1: Front view of APC 10x7 slow flyer.[1]



Figure 8.2: Top view of APC 10x7 slow flyer.[1]

2. Using the software PropellerScanner created by Martin Hepperly[18] and the previous pictures obtain the chord and the pitch distributions. Uhlig et al [19,20] sliced a propeller and contrasted the values of the chord and pitch distributions provided by PropellerScanner and showed that the chord distributions were in very good agreement and the pitch distributions had errors between 1°-2° for the propeller they measured. Nevertheless this approach provides a quick and cheap estimation of the pitch distribution without destroying the propeller. Results of the scanning are showed in appendix D.
3. PropellerScanner provides the chord and pitch distribution, however in order to reproduce accurately leading and trailing edges it is necessary to have the axis where the aerofoils are centred. In order to obtain this axis the software ImageJ was used. This software identifies the pixel intensity and provides an option for edges detection. Scaling correctly the front and top views images, the coordinates of the projected leading and trailing edges can be obtained. The axis coordinates can be estimated as:

$$y_{axis}(r) = \frac{y_{LE}(r) + y_{TE}(r)}{2} \quad (8.1)$$

$$x_{axis}(r) = \frac{x_{LE}(r) + x_{TE}(r)}{2} \quad (8.2)$$

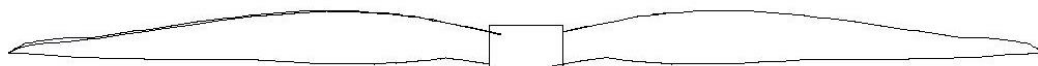
The coordinates of the axis are provided in the fourth and fifth columns of the geometry matrix in Appendix E.

- Using the same procedure as in section 5.1, generate the CAD model. Matlab routines have been slightly modified to include the transition from Eppler-63 to Clark Y aerofoils and to centre the aerofoils in the axis calculated using equation 8.1. The modified Matlab routines can be found in Appendix F and the aerofoils coordinates on Appendix G.

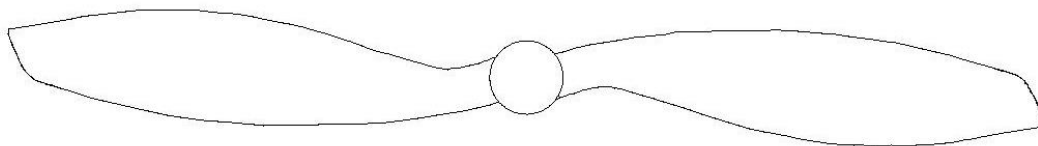
The final geometry is shown on figures 8.3-8.4.



Figure 8.3: Rendered Image of the CAD model of the propeller APC 10x7 Slow flyer.



Bottom view
Scale: 1:1



Front view
Scale: 1:1

Figure 8.4: Bottom and front views of the CAD model of the propeller APC 10x7 Slow flyer.

Considering the uncertainties and the lack of information on the propeller geometry the CAD model represents satisfactorily the original geometry.

As the previous chapter's results were concordant with the available experimental data the setup for this simulation is going to be done using the same setup as for the propeller DA4022. The turbulence model will be $k - \omega$ SST, segregated solver and same geometry of the static and rotating regions, scaled with the diameter. The mesh was first generated with the same parameters as the standard to try to maintain similar characteristics. Generating the mesh with these parameters results in a mesh which is too fine and the computational costs are high. To try to reduce the cell count the base size was increased to 0.12m but as this aerofoil is slightly thinner, the minimum surface size on the propeller blade cannot be increased if leading edge resolution is maintained. Therefore the relative minimum size was decreased to compensate this effect. The prism layer was also adapted to the new Reynolds number which is:

$$\Omega = 3008 \text{ RPM} \rightarrow Re = 49108 \quad (8.3)$$

Tables 8.1-8.2 Show the parameters for mesh generation which changed respect to the ones presented in chapter 6.

Table 8.1: Modified propeller's surface custom controls.

Curvature	76pts/circle
Edge proximity	3
Target size	10%(relative to the base)
Minimum target size	0.1% (Relative to the base)
Growth rate	1.05

Table 8.2: : Modified Prism Layer Controls for Propeller's surface.

Number of Layers	24
Wall Thickness	$1.5 \cdot 10^{-5} \text{m}$
Total Thickness	$1.0 \cdot 10^{-3} \text{m}$

These parameters result in a considerable increase in the cell count, from 664,791 to 1,455,011. Nevertheless this is the price to pay if the leading edge resolution is maintained. Actually it was slightly increased as the leading edge for E-63(4.24%) aerofoil is thinner than SDA1075(12%).

A performance study was done on this propeller for the rotation rate 3008 RPM. The propeller performance coefficients are shown on figures 8.5-8.7. Table 8.3 shows the relative errors between the CFD calculated values and the experimental available data from [1].

Table 8.3: Comparison between CFD and experimental results.

J	Error C_T (%)	Error C_P (%)	Error η (%)
0.1920	-2.1881	0.4960	-2.8362
0.2472	0.1066	3.0277	-2.6819
0.3024	1.1998	4.1758	-2.6633
0.3576	1.1954	4.3562	-2.8562
0.4128	0.8738	4.3140	-3.1966
0.4680	0.8513	4.4824	-3.3784
0.5233	0.1114	4.2575	-4.0190
0.5785	-1.5762	3.8832	-5.2146
0.6337	-2.6923	3.7648	-6.0826
0.6889	-3.9048	3.5849	-6.0333
0.7441	-5.8123	5.0004	-7.1896
0.7993	-21.7055	6.0598	-25.7839

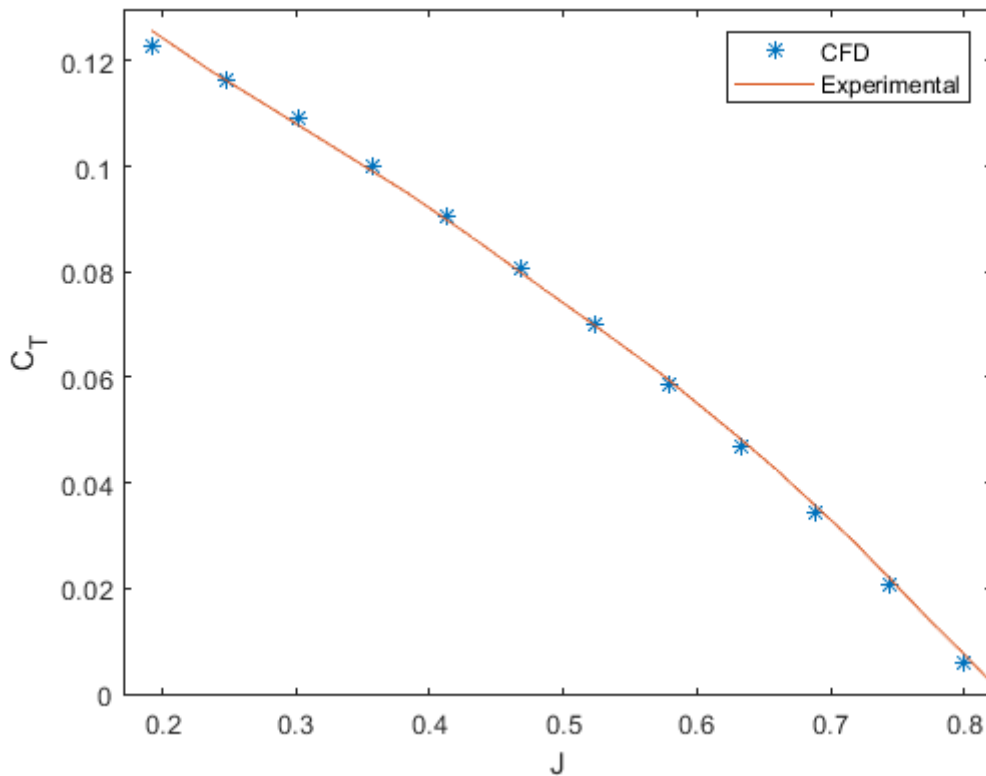


Figure 8.5: Thrust coefficient for rotation rate 3008 RPM.

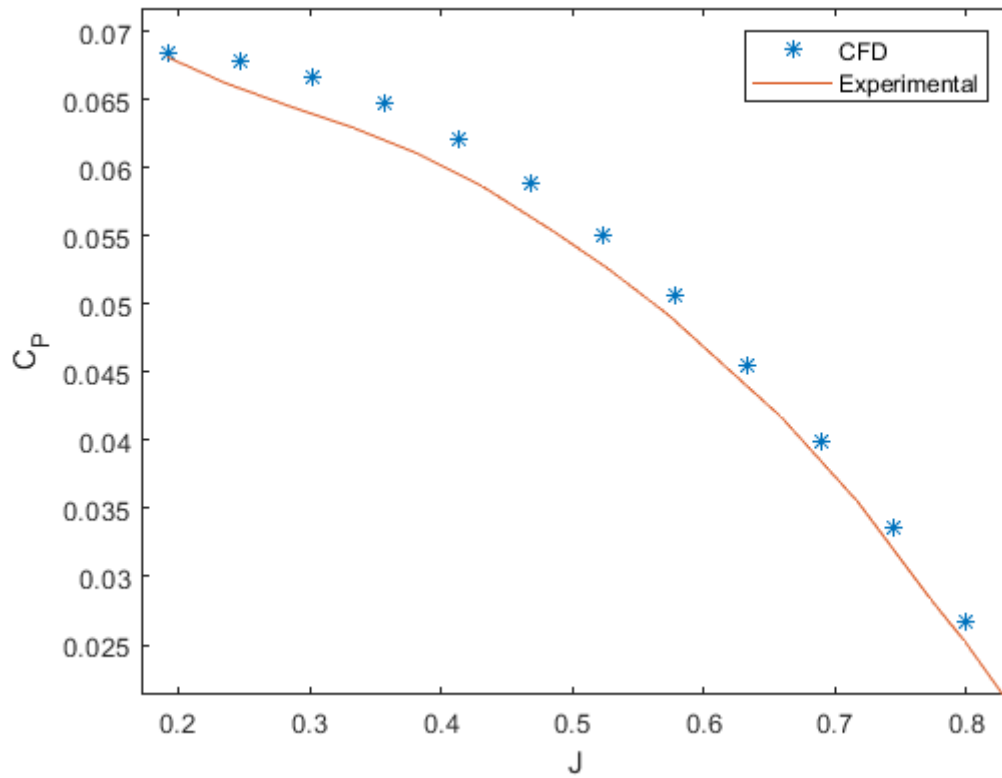


Figure 8.6: Power coefficient for rotation rate 3008 RPM.

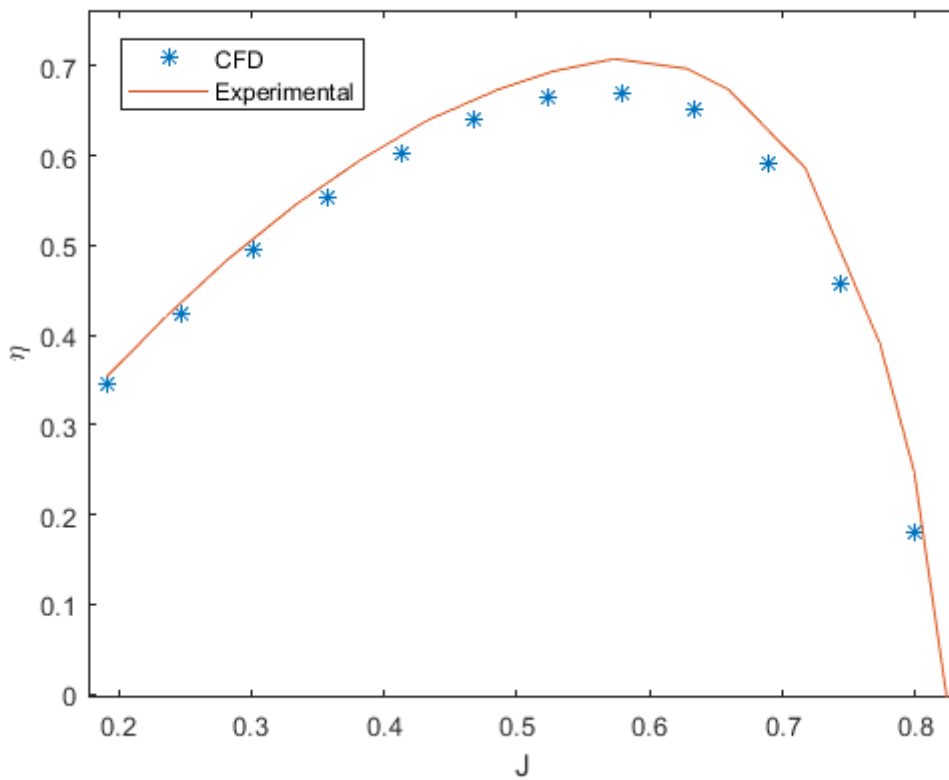


Figure 8.7: Efficiency for rotation rate 3008 RPM.

Table 8.3 shows how relative errors are under 7% for all coefficients except for the last advance ratio which has a higher relative error due to the fact that thrust is almost 0, nevertheless the absolute error is still small. Considering the uncertainty in the geometry and the great sensitivity of propeller performance to the pitch angle the CFD results mimic well experimental results carried out by UIUC [1].

It is also interesting to compare the results obtained by the performed CFD simulations with the available performance data from the manufactures, Advanced Precision Composites(APC) [6]. Figures 8.8-8.10 show considerable disagreement between the manufacturers performance data and CFD simulations. The performance data provided by the manufacturers are based on vortex theory, using actual propeller geometry. The NASA Transonic Airfoil Analysis Computer Program is used to generate estimates for section lift and drag, which would provide incorrect predictions for low Reynolds numbers scenarios. The manufacturers are currently working on ways to improve these results and they acknowledge that the actual way leads to errors for low Reynolds numbers.

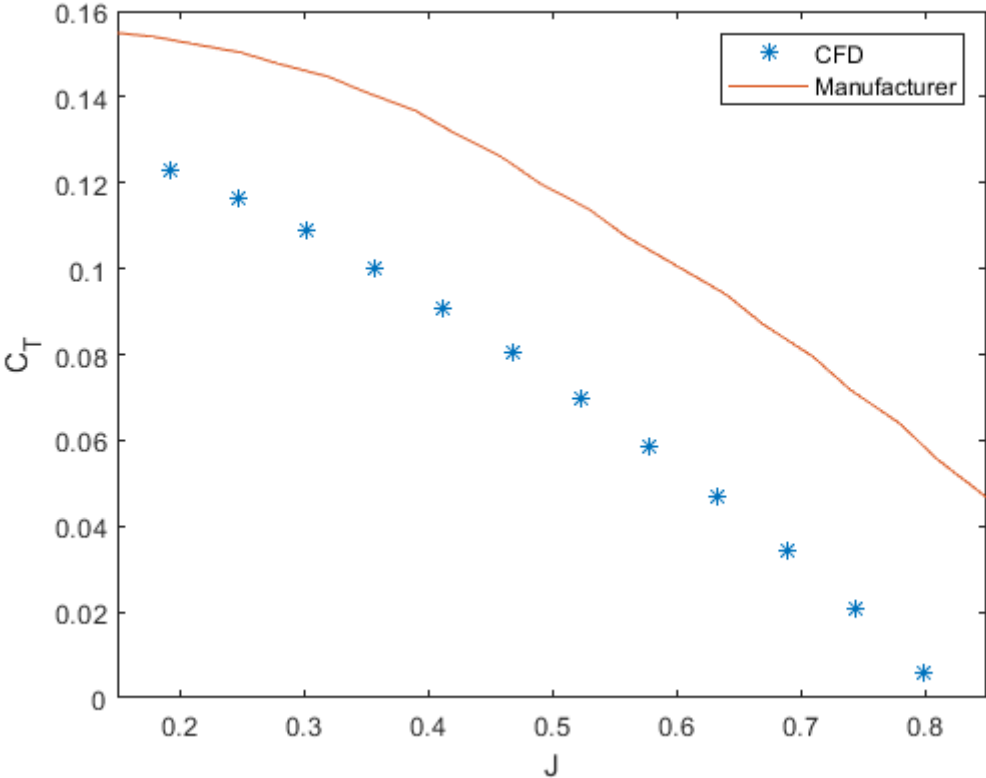


Figure 8.8: Thrust coefficient CFD results (3008RPM) and manufacturers data(3000RPM).

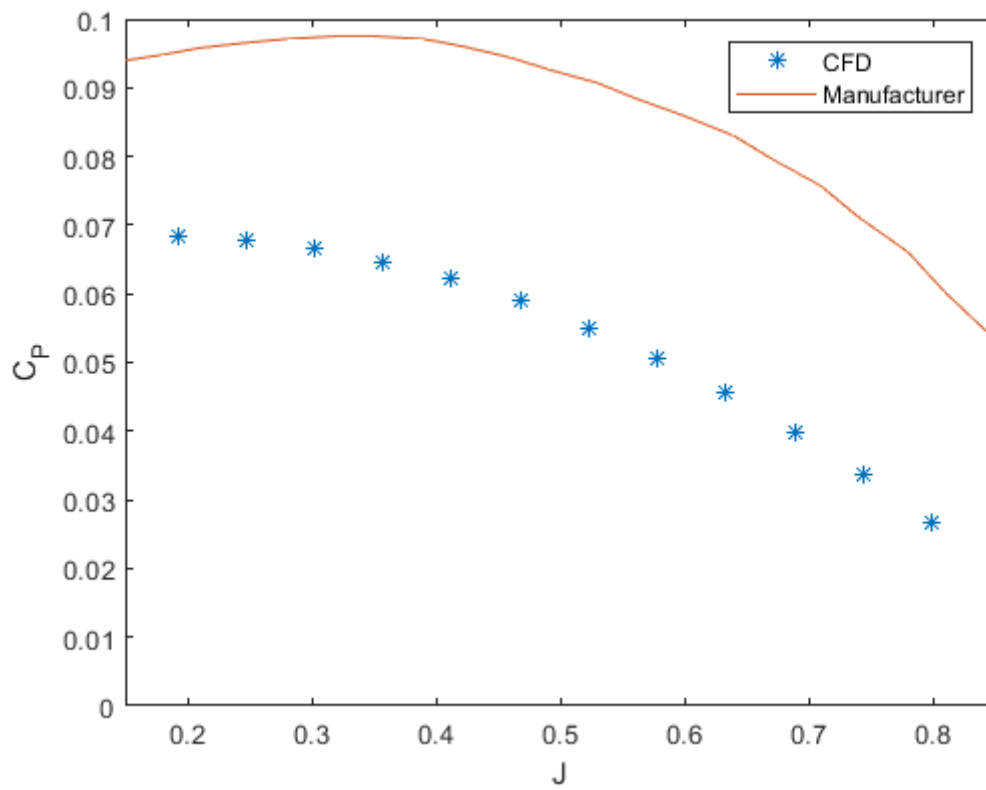


Figure 8.9: Power coefficient CFD results (3008RPM) and manufacturers data(3000RPM).

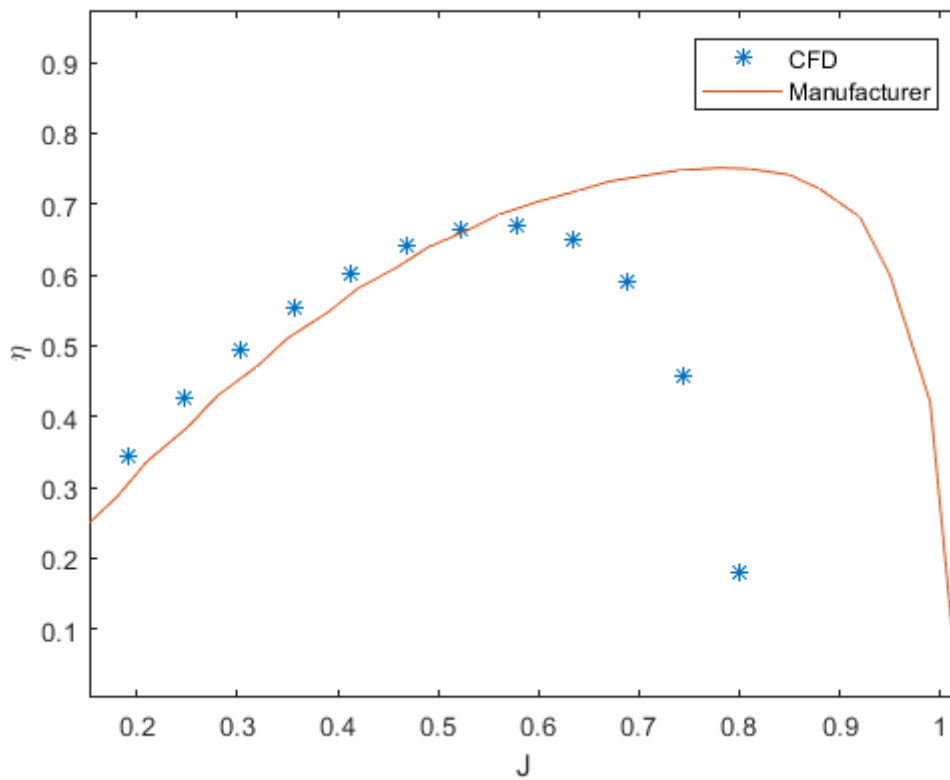


Figure 8.10: Efficiency CFD results (3008RPM) and manufacturers data(3000RPM).

9 Conclusions and Future work

The CFD model developed in this work has been proven reliable for the propellers and conditions tested being able to reproduce the performance degradation seen in experiments for low Reynolds number. The mesh refinement study shows that the fine mesh improves slightly the prediction of the performance coefficients compared to the standard mesh most probably due to the better resolution of the leading edge. Nevertheless the improvement is under 2% in all coefficients for both advance ratios tested and considering the uncertainty on the modelled geometry and that the cell count increased by over 250% the standard mesh was used for the different studies performed on this work.

Sensitivity analysis performed on the rotating region shows that if the enclosing domain's radial dimension is over 10% higher than the propeller's radius the performance coefficients differ less than 1%. Similarly, when the length of the cylinder that constitutes the rotating domain is bigger than 40% of the propeller's diameter the performance coefficients differ less than 1%.

The turbulence modelling study shows that both methods of the $k - \omega$, standard and SST, model adequately turbulence in our problem. On the other hand the realizable $k - \epsilon$ model seems to have problems dealing with the rotating reference frame, providing unphysical turbulent viscosity distributions and the Spalart-Allmaras model under predicts turbulence magnitudes obtaining results comparable to the laminar case.

Performance coefficients remain unchanged when varying the boundary condition set on the outer walls from no-slip condition to freestream boundary condition.

The study performed on the type of interface selected to act as a link between both, static and rotating regions, shows that if the rotating domain is large enough both type of interfaces provide similar results. If the rotating region is not large enough to let the flow evolve into an axisymmetric distribution, the mixing plane interface shows a small improvement in the prediction of the performance coefficients.

The comparison between the unsteady simulation and the Multiple Reference Frame approach reveals that, for the advance ratio and rotational rate tested, the overall impact of the unsteady effects on the performance coefficients is almost negligible and therefore reinforces the applicability of this steady state approach to propeller performance analysis.

The performance study done on the propeller DA-4022 shows relative errors under 10% for all coefficients apart from those associated to advance ratios near thrust reversal where the relative errors increase considerably. When the rotation rate was increased from 4546 RPM to 7559 RPM similar discrepancies with experimental results were obtained. For low advance ratios and high rotation rates, CFD simulations show a systematic decrease in thrust and power coefficients. This is probably due to an increase in pitch by deformation of the blade towards the tip due to the higher rotational speeds.

The comparison between the CFD simulations associated to both rotational rates shows an almost constant thrust coefficient and a considerable drop of the power coefficient when the rotation rate increases (and so does the Reynolds number). This causes a generalised rise in the propeller's efficiency when the Reynolds number increases as experimental results suggest. The peak efficiency for the higher rotational rate shows an increase of 3.85% respect to the lower one.

An Advanced Precision Composites(APC) propeller, the prototype 10x7 Slow Flyer, was satisfactorily CAD modelled with the help of PropellerScanner and ImageJ softwares to obtain geometrical parameter from propeller images. The performance analysis carried out for this propeller shows good agreement with experimental results, with errors under 6% for all coefficients and advance ratios except the ones very close to thrust reversal. Comparisons

with the data provided by the manufactures obtained by vortex theory, show big discrepancies reinforcing the need to find an alternative way to estimate appropriately small scale propeller performance and so low Reynolds numbers effects.

One of the main issues in validating CFD models for small scale propellers precisely is the considerable uncertainty in the propeller's geometry. It is really difficult to assure that the geometry for which the experiments are performed is the same as the one in the CFD model. The best way will probably be to CAD model a propeller, use precise 3D printing and then perform the experiments on that propeller. There will still be some errors due to the manufacturing process, but in this way they could certainly be reduced.

Another possible improvement would be to perform a more comprehensive and detailed turbulence modelling study, checking more complex and computationally demanding models such as Reynolds Stress Modelling or resolving scale simulations such as LES and DES.

An interesting development would be to modify and test the applicability of this model to compressible and low Reynolds numbers conditions which can be found in propellers operating at very high altitudes and also in Mars atmosphere. If the model was proven reliable, expensive experimental tests could be replaced by CFD simulations.

Another possible future work could be to integrate this CFD model into a design and/or optimisation tool to provide insides of the most adequate propeller geometry for unconventional flow conditions in which propeller design is not as well documented, for example the conditions mentioned on the previous paragraph.

10 Bibliography

1. J.B. Brandt, R.W. Deters, G.K. Ananda, and M.S. Selig (8 January 2019), *UIUC Propeller Database*, University of Illinois at Urbana-Champaign, retrieved from <http://m-selig.ae.illinois.edu/props/propDB.html>.
2. Brandt, J. B., "Small-Scale Propeller Performance at Low Speeds," M.S. Thesis, Department of Aerospace Engineering, University of Illinois at Urbana-Champaign, Illinois, 2005.
3. Brandt, J.B. and Selig, M.S., "Propeller Performance Data at Low Reynolds Numbers," *49th AIAA Aerospace Sciences Meeting*, AIAA Paper 2011-1255, Orlando, FL, January 2011.
4. Deters, R.W., Ananda, G.K., and Selig, M.S., "Reynolds Number Effects on the Performance of Small-Scale Propellers," *AIAA Aviation and Aeronautics Forum and Exposition (Aviation 2014)*, AIAA Paper 2014-2151, Atlanta, GA, June 2014.
5. Deters, R.W., "Performance and Slipstream Characteristic of Small-Scale Propellers at Low Reynolds Numbers," Ph.D. Dissertation, Department of Aerospace Engineering, University of Illinois at Urbana-Champaign, Urbana, IL, 2014.
6. APC Slow Flyer. Available online: <https://www.apcprop.com/Articles.asp?ID=262#airfoil> (accessed on 10 January 2019).
7. ANSYS, Inc. ANSYS Fluent User's Guide. Available online: <http://159.226.251.229/videoplayer/ANSYS%20Fluent%20Users%20Guide.pdf?ichuri=4430682d62b326e212655a3feab3426a&ichstart=0&ichend=0&ichkey=1745028923750463592455&ichtype=1&ichdiskid=1&ichunit=1> (accessed on 15 January 2019).
8. ANSYS, Inc. Modeling Turbulent Flows, Introductory Fluent Training. Available online: http://www.southampton.ac.uk/~nwb/lectures/GoodPracticeCFD/Articles/Turbulence_Notes_Fluent-v6.3.06.pdf(accessed on 15 January 2019).
9. Tognaccini, R. Lezioni di Aerodinamica dell'Ala Rotante. Università degli Studi di Napoli. Available online: http://wpage.unina.it/rtogna/Aerodinamica_del_rotore.pdf (accessed on 15 November 2018)
10. Zaza, D. Analisi delle prestazioni e del campo di moto indotto da un'elica in ambiente marziano, M.S Thesis , Politecnico di Torino, Turin, Italy, 2017.
11. Mehdipour, R. Simulating propeller and Propeller-Hull Interaction in OpenFOAM, Master of Science Thesis ,Autumn 2013,Master's Thesis at Centre for Naval Architecture,Royal Institute of Technology, Stockholm, Sweden.
12. M. Knight, R. A. Hefner. Static Thrust Analysis of the Lifting Airscrew. 1973.

13. W. Z. Stepniewski. Rotary-Wing Aerodynamics, Vol. I. Philadelphia, Pennsylvania.
14. McGranahan, B. D. Surface Oil Flow Measurements on Several Airfoils at Low Reynolds Numbers. M.S. Thesis, University of Illinois at Urbana-Champaign, Urbana, IL, 2003.
15. STAR CCM+ Documentation. Version 12.04. Siemens PLM Software, 2017.
16. Schlichting, H., Gersten, K., Krause, E. and Oertel, H. (n.d.). *Boundary-layer theory*. 9th Edition, 2017.
17. Kutty, H. and Rajendran, P. 3D CFD Simulation and Experimental Validation of Small APC Slow Flyer Propeller Blade. *Aerospace*, 4(1), p.10., 2017.
18. Hepperle, M., PropellerScanner. <http://mh-aerotools.de>, (Accessed February 1st, 2019.)
19. Uhlig, D. V. Post Stall Propeller Behaviour at Low Reynolds Numbers. M.S. Thesis, University of Illinois at Urbana-Champaign, Urbana, IL, 2007.
20. Uhlig, D. V. and Selig, M. S. Post Stall Propeller Behaviour at Low Reynolds Numbers. AIAA Paper 2008-0407, 2008.
21. Theodorsen, T., Stickle, G. and Brevoort, M. (1937). *Characteristics of Six Propellers Including the High-Speed Range*. [online] Ntrs.nasa.gov. Available at: <https://ntrs.nasa.gov/search.jsp?R=19930091669> [Accessed 10 Mar. 2019].
22. Subhas, S. CFD analysis of a propeller flow and cavitation. *Int. J. Comput. Appl.* **2012**, 55, 26–33.
23. Wang, X.;Walter, K.S. Computational analysis of marine-propeller performance using transition-sensitive turbulence modeling. *J. Fluids Eng.* **2012**, 134, 071107.
24. Morgut, M.; Nobile, E. Influence of grid type and turbulence model on the numerical prediction of the flow around marine propellers working in uniform inflow. *Ocean Eng.* **2012**, 42, 26–34.
25. Morgado, J.; Silvestre, M.Â.R.; Páscoa, J.C. Validation of new formulations for propeller Analysis. *J. Propuls. Power* **2015**, 31, 467–477.
26. Morgado, J.; Silvestre, M.A.R.; Páscoa, J.C. A comparison of post-stall models extended for propeller performance prediction. *Aircr. Eng. Aerosp. Technol.* **2016**, 88, 540–549.
27. Morgado, J.; Abdollahzadeh, M.; Silvestre, M.A.R.; Páscoa, J.C. High altitude propeller design and analysis. *Aerosp. Sci. Technol.* **2015**, 45, 398–407.

APPENDIX A: SDA 1075 Aerofoil coordinates.

x/c	y/c	x/c	y/c
1.000000	0.005557	0.000280	-0.001921
0.996593	0.005916	0.004701	-0.007905
0.986424	0.007201	0.015056	-0.014217
0.970307	0.009369	0.030301	-0.020208
0.948605	0.012241	0.050355	-0.025609
0.921585	0.015743	0.075069	-0.030290
0.889621	0.019963	0.104265	-0.034146
0.853243	0.024878	0.137711	-0.037140
0.813012	0.030409	0.175126	-0.039253
0.769531	0.036448	0.216177	-0.040503
0.723430	0.042837	0.260479	-0.040926
0.675369	0.049377	0.307602	-0.040585
0.625945	0.055764	0.357073	-0.039554
0.575694	0.061768	0.408381	-0.037928
0.525145	0.067169	0.460985	-0.035812
0.474806	0.071778	0.514304	-0.033341
0.425168	0.075411	0.567727	-0.030638
0.376692	0.077929	0.620617	-0.027832
0.329814	0.079200	0.672308	-0.025029
0.284932	0.079143	0.722150	-0.022300
0.242417	0.077694	0.769510	-0.019711
0.202594	0.074839	0.813783	-0.017302
0.165758	0.070588	0.854396	-0.015105
0.132147	0.065010	0.890816	-0.013128
0.101982	0.058221	0.922559	-0.011366
0.075425	0.050381	0.949178	-0.009777
0.052643	0.041731	0.970411	-0.008207
0.033775	0.032527	0.986204	-0.006742
0.018960	0.023081	0.996295	-0.005793
0.008287	0.013758	0.999851	-0.005553
0.001894	0.005047		

APPENDIX B: Geometry data DA4022.

r/R	c/R	$\beta(^{\circ})$
0.15	0.1269	41.63
0.2	0.1291	44.363
0.25	0.1807	40.568
0.3	0.2226	36.964
0.35	0.2341	33.869
0.4	0.2315	30.788
0.45	0.2299	28.316
0.5	0.2306	26.401
0.55	0.2313	24.686
0.6	0.2312	23.127
0.65	0.2314	21.825
0.7	0.2316	20.734
0.75	0.2317	19.766
0.8	0.2319	18.922
0.85	0.2319	18.172
0.9	0.2318	17.52
0.95	0.2228	15.544
1	0.0134	14.05

APPENDIX C: Matlab Routines for CAD generation.

1. Main.m

```
load('P')%load aerofoil coordinates N1X2 matrix (x,y) (Appendix A)
load('X')%load geometry files M1X3 matrix (r/R,c/R,beta) (Appendix B)
[N1,N2]=size(P);
N=N1+4;%4 zero rows added at the end of every aerofoil for Excel macro
[M1,M2]=size(X);
Y=zeros((N1+4)*M1,3);
for t=1:M1
    Y(N*t-(N1-1):N*t,1:2)=turn(X(t,3),P*2.5*25.4*X(t,2));%Turn+scale aerofoils
    Y(N*t-(N1-1):N*t,3)=X(t,1)*2.5*25.4; %Place aerofoil in z-axis
end
filename = 'Newturn.xls';
xlswrite(filename,Y)%Writting coordinates on excel file, these coordinates
will be written in 3 columns(x,y,z) and (N1+4)*M1 rows, Each N1+4 set of
rows represent a profile.
```

2. turn.m

```
function X=turn(beta,Y)
b=(-90+beta)/180*pi;%Turn 90° extra around z axis to align aerofoil y-axis.
Y(:,1)=-Y(:,1)+0.5*Y(1,1);%Centring Aerofoil at 50% of the chord.
X=( [cos(b) -sin(b);sin(b) cos(b)]*(Y) )';%Turning centred aerofoil angle b.
end
```

APPENDIX D: PropellerScanner raw data: APC Slow Flyer 10x7 inches.

r/R	c/R	r(mm)	C(mm)	β (°)	H(mm)
0,0134	0,2641	1,7041	28,4956	31,823	6,6447
0,0629	0,1469	7,9823	15,2164	35,3555	35,5843
0,1123	0,0978	14,2606	10,2604	34,2666	61,0459
0,1617	0,1185	20,5388	11,6699	39,1582	105,0933
0,2112	0,1413	26,8171	14,0581	38,4188	133,6387
0,2606	0,1615	33,0953	16,4772	36,5542	154,1752
0,31	0,1789	39,3736	18,8194	34,0531	167,2017
0,3595	0,1941	45,6518	20,9873	31,6154	176,571
0,4089	0,2051	51,9301	22,8272	28,7715	179,1665
0,4583	0,2142	58,2083	24,4775	25,8566	177,2488
0,5078	0,2194	64,4866	25,6306	23,0942	172,7757
0,5572	0,2216	70,7648	26,2662	21,0496	171,1184
0,6066	0,2204	77,0431	26,3891	19,4597	171,0375
0,6561	0,2156	83,3213	26,0355	18,0059	170,1623
0,7055	0,2069	89,5996	25,1642	16,689	168,7812
0,7549	0,1945	95,8778	23,842	15,1308	162,8924
0,8044	0,1786	102,1561	22,0226	13,9044	158,8981
0,8538	0,1586	108,4343	19,6445	12,7399	154,0396
0,9032	0,1348	114,7126	16,7591	11,7218	149,5477
0,9527	0,104	120,9908	12,9921	10,3796	139,2449
1	0,0099	127	1,2557	0	0

APPENDIX E: Geometry Matrix APC Slow Flyer 10x7 inches.

r/R	c/R	Beta(°)	0.5 chord line(x-axis)	0.5 chord line(y-axis)
0.05	0.109	34.4349	0	0
0.15	0.109	37.9997	3.2544	2.3498
0.2	0.132	38.5861	3.1167	2.7324
0.25	0.155	36.9543	2.6233	2.8764
0.3	0.175	34.5594	2.0821	2.9998
0.35	0.192	32.0832	1.0286	3.0872
0.4	0.206	29.2839	0.0743	3.2204
0.45	0.216	26.3464	-0.6826	3.2369
0.5	0.222	23.5295	-1.3063	3.1419
0.55	0.225	21.3476	-2.1386	2.9216
0.6	0.224	19.6721	-2.7452	2.5133
0.65	0.219	18.1851	-3.3633	2.0663
0.7	0.21	16.8356	-3.8548	1.5921
0.75	0.197	15.2854	-4.5583	1.2267
0.8	0.18	14.0134	-4.9145	0.7775
0.85	0.159	12.8295	-5.3691	0.5116
0.9	0.133	11.7877	-5.7588	0.4309
0.95	0.1077	10.4528	-6.2914	0.3256
1	0.0100	9.0000	-11.2914	-0.7198

APPENDIX F: Matlab routines for APC CAD Generation.

1. Main_APC.m

```
load('P_e62')%load aerofoil coordinates N1X2 matrix (x,y) (Appendix G)
load('P_c')%load aerofoil coordinates N11X2 matrix (x,y) (Appendix G)
load('X')%load geometry files M1X5 matrix (r/R,c/R,beta,0.5 Chord line
front view, 0.5 Chord line top view) (Appendix E)
r=0.90;%transition Aerofoil
[N1,N2]=size(P_e62);
[N11,N22]=size(P_c);
N=N1+4;%4 zero rows added at the end of every aerofoil for Excel macro
[M1,M2]=size(X);
P=P_e62;% First aerofoil
T=round(r*18,0);%Transition index
Y=zeros((N1+4)*T+(N11+4)*(M1-(T+1)),3);
for t=1:T
    Y(N*t-(N1-1):N*t,3)=X(t,1)*5*25.4; %Place aerofoil in correct z-axis
    Y(N*t-(N1-1):N*t,1:2)=turn(X(t,3),P*5*25.4*X(t,2),X(t,4),X(t,5));%Turn and
scale aerofoil
end
P=P_c;%Second aerofoil
N1=N11; %change indices
N2=N22; %change indices
N=N1+4; %change indices
for t=T+1:M1
    z=60;%Difference in number of aerofoil points
    Y(N*t-(N1-1)-(z*(T)):N*t-(z*(T)),3)=X(t,1)*5*25.4;
%Place aerofoil in correct z-axis
    Y(N*t-(N1-1)-(z*(T)):N*t-
(z*(T)),1:2)=turn(X(t,3),P*5*25.4*X(t,2),X(t,4),X(t,5));%Turn and scale
aerofoil
end
filename = 'New_108_correctin.xls';
xlswrite(filename,Y) %Writting coordinates on excel file, these coordinates
will be written in 3 columns(x,y,z) and (N1+4)*M1 rows, Each N1+4 set of
rows represent a profile.
```

2. Turn_APC.m

```
function X=turn(beta,Y,j,i)
%T is the leading edge function
b=(90+beta)/180*pi;%Turning 90° the Pitch angle around z axis to align
aerofoil with negative y-axis.
Y(:,1)=-(Y(:,1))+0.5*Y(1,1);%Centring Aerofoil at 50% of the chord.
X=[cos(b) -sin(b);sin(b) cos(b)]*(Y)';%Turning centred aerofoil
coordinates angle b.
X(:,2)=X(:,2)+j;%Centring Aerofoil on axis.
X(:,1)=X(:,1)-i;%Centring Aerofoil on axis.
end
```

APPENDIX G: APC 10x7 slow flyer aerofoil coordinates.

1. E-63 (4.25%)

x/c	y/c	x/c	y/c
1	0	0.00536	0.00766
0.99719	0.00121	0.00076	0.00218
0.98938	0.00473	0.00055	-0.00141
0.97751	0.00986	0.00557	-0.00306
0.96173	0.01553	0.01651	-0.0033
0.94164	0.02126	0.03316	-0.00227
0.91717	0.02709	0.0555	-0.00004
0.88861	0.03301	0.08342	0.00315
0.85624	0.03885	0.11671	0.00708
0.82039	0.04451	0.15504	0.01151
0.78141	0.04985	0.198	0.0162
0.73968	0.0548	0.24509	0.02093
0.69562	0.05921	0.29574	0.02546
0.64967	0.06304	0.34931	0.02962
0.60229	0.06617	0.40513	0.03319
0.55394	0.06857	0.46247	0.03605
0.50509	0.07016	0.52056	0.03803
0.45624	0.07094	0.57859	0.03907
0.40786	0.07084	0.63576	0.03907
0.36043	0.0699	0.69125	0.03806
0.31441	0.06809	0.7443	0.03604
0.27026	0.06545	0.79414	0.0331
0.2284	0.06198	0.84004	0.0293
0.1892	0.05775	0.88132	0.02482
0.15304	0.0528	0.91735	0.01979
0.12023	0.04723	0.94756	0.01439
0.09103	0.04111	0.97115	0.00887
0.06568	0.03457	0.98754	0.0041
0.04435	0.02775	0.99695	0.00102
0.02714	0.02083	1	0
0.01416	0.01404		

2. Clark Y

x/c	y/c	x/c	y/c
1.0000	0.0000	0.4200	0.0906
0.9900	0.0030	0.4000	0.0912
0.9800	0.0053	0.3800	0.0915
0.9700	0.0077	0.3600	0.0916
0.9600	0.0100	0.3400	0.0915
0.9400	0.0146	0.3200	0.0912
0.9200	0.0191	0.3000	0.0907
0.9000	0.0235	0.2800	0.0900
0.8800	0.0278	0.2600	0.0891
0.8600	0.0320	0.2400	0.0878
0.8400	0.0361	0.2200	0.0861
0.8200	0.0400	0.2000	0.0839
0.8000	0.0439	0.1800	0.0811
0.7800	0.0476	0.1600	0.0776
0.7600	0.0513	0.1400	0.0734
0.7400	0.0548	0.1200	0.0686
0.7200	0.0582	0.1000	0.0630
0.7000	0.0614	0.0800	0.0564
0.6800	0.0646	0.0600	0.0488
0.6600	0.0676	0.0500	0.0443
0.6400	0.0705	0.0400	0.0391
0.6200	0.0732	0.0300	0.0330
0.6000	0.0758	0.0200	0.0254
0.5800	0.0781	0.0120	0.0179
0.5600	0.0803	0.0080	0.0137
0.5400	0.0824	0.0040	0.0089
0.5200	0.0842	0.0020	0.0058
0.5000	0.0859	0.0010	0.0037
0.4800	0.0874	0.0005	0.0023
0.4600	0.0886	0.0000000	0.0000000
0.4400	0.0897	0.0005000	-.0046700

x/c	y/c	x/c	y/c
0.0010000	-.0059418	0.5000000	-.0189619
0.0020000	-.0078113	0.5200000	-.0182262
0.0040000	-.0105126	0.5400000	-.0174914
0.0080000	-.0142862	0.5600000	-.0167572
0.0120000	-.0169733	0.5800000	-.0160232
0.0200000	-.0202723	0.6000000	-.0152893
0.0300000	-.0226056	0.6200000	-.0145551
0.0400000	-.0245211	0.6400000	-.0138207
0.0500000	-.0260452	0.6600000	-.0130862
0.0600000	-.0271277	0.6800000	-.0123515
0.0800000	-.0284595	0.7000000	-.0116169
0.1000000	-.0293786	0.7200000	-.0108823
0.1200000	-.0299633	0.7400000	-.0101478
0.1400000	-.0302404	0.7600000	-.0094133
0.1600000	-.0302546	0.7800000	-.0086788
0.1800000	-.0300490	0.8000000	-.0079443
0.2000000	-.0296656	0.8200000	-.0072098
0.2200000	-.0291445	0.8400000	-.0064753
0.2400000	-.0285181	0.8600000	-.0057408
0.2600000	-.0278164	0.8800000	-.0050063
0.2800000	-.0270696	0.9000000	-.0042718
0.3000000	-.0263079	0.9200000	-.0035373
0.3200000	-.0255565	0.9400000	-.0028028
0.3400000	-.0248176	0.9600000	-.0020683
0.3600000	-.0240870	0.9700000	-.0017011
0.3800000	-.0233606	0.9800000	-.0013339
0.4000000	-.0226341	0.9900000	-.0009666
0.4200000	-.0219042	1	0
0.4400000	-.0211708		
0.4600000	-.0204353		
0.4800000	-.0196986		